2001

Deformation Studies of Tungsten-Gold Contacts at the Nanometer Scale.

Steven A. Smallwood

DEFORMATION STUDIES OF TUNGSTEN-GOLD CONTACTS AT THE NANOMETER SCALE

By

Steven A. Smallwood

B.S. University of North Carolina at Charlotte, 1992

A THESIS

Submitted in Partial Fulfillment of the

Requirements for the Degree of

Doctor of Philosophy

(in Physics)

The Graduate School

The University of Maine

May, 2001

Advisory Committee:

Robert J. Lad, Professor of Physics, Advisor

William N. Unertl, Professor of Physics

Richard A. Morrow, Professor of Physics

Charles W. Smith, Professor of Physics

Brian G. Frederick, Assistant Professor of Chemistry

External Reader

Peter Grütter, Associate Professor of Physics, McGill University

DEFORMATION STUDIES OF TUNGSTEN-GOLD CONTACTS AT THE NANOMETER SCALE

By Steven A. Smallwood

Thesis Advisor: Dr. Robert J. Lad

An Abstract of the Thesis Presented
in Partial Fulfillment of the Requirements for the
Degree of Doctor of Philosophy
(in Physics)
May, 2001

The deformation behavior of atomically clean, nanometer sized tungsten / gold contacts was studied at room temperature in ultra-high vacuum. An instrument that combines atomic force microscopy (AFM), scanning tunneling microscopy (STM), and field ion microscopy (FIM) into a single experimental apparatus was designed, constructed, and calibrated. A cross-hair force sensor having a spring constant of ~ 442 N/m was developed and its motion was monitored during indentation experiments with a differential interferometer. Tungsten tips of controlled size (12.8 nm < tip radius < 21.6 nm) were first shaped and characterized using FIM and then indented into a Au (110) single crystal to depths ranging from 1.5 nm to 18 nm using the force sensor. Continuum mechanics models were found to be valid in predicting elastic deformation during initial contact and plastic zone depths despite our small size regime. Multiple discrete yielding events lasting < 1.5 ms were observed during the plastic deformation regime; at the yield points a maximum value for the principal shear stress was measured to be 5 ± 1 GPa.

During tip withdrawal, "pop-out" events relating to material relaxation within the contact were observed. Adhesion between the tip and sample led to experimental signatures that suggest neck formation prior to the break of contact. STM images of indentation holes revealed various shapes that can be attributed to the $\{111\}\langle 110\rangle$ crystallographic slip system in gold. FIM images of the tip after indentation showed no evidence of tip damage.

Acknowledgements

I would first and foremost like to extend my deepest gratitude to God for all the wisdom, knowledge and skills that he has so freely given me. Also for the desire, patience and endurance to seek my education to this extent. I am extremely grateful to my thesis advisor, Professor Robert J. Lad. Under his guidance I have found a true source of encouragement and ideas through the years. Professor Lad's patience and friendly manner have been a pleasure to work with during my time here. I would also like to thank the rest of my committee members, Professors William Unertl, Brian Frederick, Richard Morrow and Charles Smith for their support and guidance. I'd like to thank Dr. Marius Enachescu who spent much time in development of this instrument and Dr. Anna Cichos for her assistance and encouragement (also for her creation of Figure 1.1). I'd also like to extend my appreciation to those who were working on the project in its early stages: Dr. William Unertl, Chris Richardson, Aaron Washburn, Tom McIntire and Marcus Neitzert. I would like to thank Dr. Alan Melmed of Johns Hopkins University for allowing me to work with him for one month and for all his useful suggestions and expertise in the area of field ion microscopy. I'd like to extend my gratitude to my external thesis reviewer, Professor Peter Grütter of McGill University.

Financial support for this work was provided by the EPSCoR program from the Department of Energy, the Maine Science and Technology Foundation, and the Laboratory for Surface Science and Technology at the University of Maine.

The one person who may very well have influenced this project the most is Nick LeCursi. His talents and friendship were absolutely invaluable in this project and in my

life during these years. LASST has provided me with the opportunity to work with a diversified group of individuals, many of whose assistance I've required through the years. I would like to thank the following individuals for their help, and I apologize for any whom I have accidentally left out: Dr. David Frankel, Paul Caroll, Bronson Crothers, Scott Moulzolf, Pasti Popescu, Dann Woodland, Jody DiLorenzo, David Grenier, Mike Davis, Eric Martin, Molly Kovaka, Dale Goodwine, Patty Paul and Barbara Deshane.

Finally, I must acknowledge those most important to me, my family. The most significant person in my life during these years, my wife Shannon, I can not even begin to describe my deepest appreciation for all her support, understanding and patience through this time. I thank my mother for all the encouragement and freedom that she gave me as I grew, and my father; I wish you could have been here to see this dad.

Proverbs 3:5 Trust in the Lord with all your heart and lean not on your own understanding; in all your ways acknowledge him, and he will make your paths straight.

Table of Contents

List of Tables

List of Figures

Chapter 1

INTRODUCTION

Manipulation of matter at the nanometer scale can lead to unique electrical, mechanical, and chemical properties and behavior in so-called 'nanomaterials' that differ considerably from the behavior of bulk materials. This new exciting field of nanotechnology has prompted intense research that spans a variety of disciplines in science and engineering. The U.S. federal government anticipates that nanotechnology will have a profound impact on our economy and society and is making a major investment in this area as recently summarized in a report on the National Nanotechnology Initiative (NNI) by the National Science and Technology Council [1]. This initiative is expected to lead to significant advances in technologies associated with materials and manufacturing, electronics, medicine, environment, energy, chemicals, agriculture, information technology, and national security.

Mechanical properties of materials at the nanometer scale are extremely important in the fabrication and operation of microelectromechanical systems (MEMS), nanodevices, and nanomachines. The mechanisms of friction, lubrication, wear, deformation and fracture all take on a new meaning at nanometer size scales [2,3]. For example, adhesion effects in nanosized relay contacts and microgears can cause 'stiction' phenomena in which large adhesive surface forces cause nanosized regions to stick together and limit reliable motion. Fundamental as well as applied research will be required to fully elucidate the mechanics of these nanosystems.

The invention and application of scanned probe microscopies have made a major impact on our understanding of the mechanics of sharp tips interacting with surfaces. Several pioneering AFM experiments done by Colton *et al.* [4] and others revealed information about elasticity, adhesive forces and material yielding at nanometer sized contacts which began to bridge the knowledge gap between the nanometer scale and orders of magnitude larger contacts probed by "nanoindentor" instruments [5,6,7]. However, these early AFM experiments were carried out in an air ambient with undefined tips and surfaces. Contaminants at the contact including condensed water had a large effect on the adhesive forces measured in these experiments. Figure 1 shows a model comparison of the tip-surface interactions expected in a "dirty" contact in air versus a "clean" contact in ultra-high vacuum.

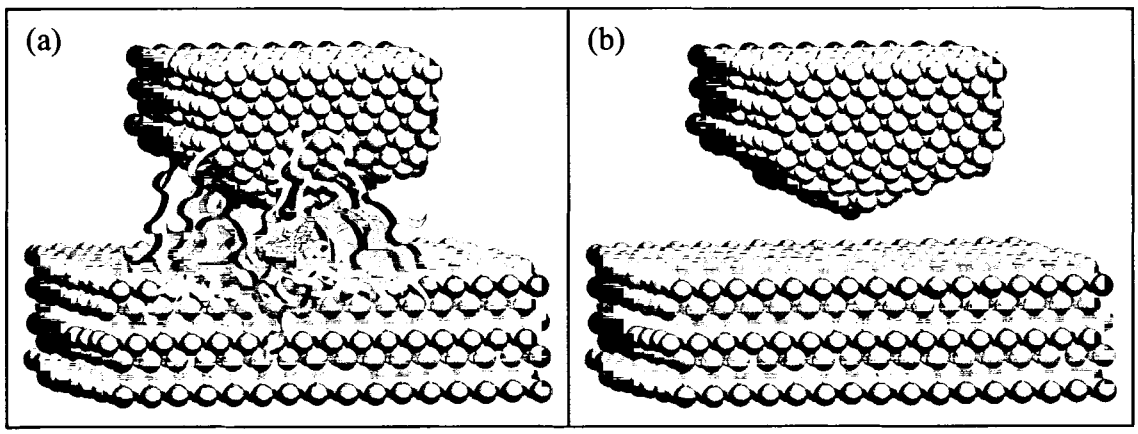

Figure 1.1: Dirty versus clean tip-surface contact. (a) Dirty contact in air. (b) Clean contact in ultra-high vacuum.

The main focus of the work described in this thesis is to explore nanometer scale mechanical properties of "clean" contacts. A significant question to ask is: *How well do continuum mechanics theories predict deformation behavior in the nanometer size regime?* To address this question, we built an instrument that combined the capabilities

of atomic force microscopy (AFM), scanning tunneling microscopy (STM), and field ion microscopy (FIM). This ultra-high vacuum instrument allows atomically clean tungsten tips to be shaped and characterized by FIM and be immediately used for indentation experiments on atomically clean single crystal gold surfaces. Experimental signatures of the deformation behavior acquired with this instrument provides information that can be compared to predictions from continuum mechanics theories [8,9] as well as molecular dynamics simulations [10,11,12].

Several other groups [4,13,14,15,16] have used similar experimental approaches to gain a better understanding of nanometer sized contacts involving gold surfaces. These experiments cover a wide range of contact sizes (2 nm < contact radius < 300 nm) and involve tungsten or diamond tips indented into a gold surface. The diamond/gold and tungsten/gold systems have been used primarily because atomically clean gold is relatively easy to prepare, and these tips are much harder than gold meaning that most of the deformation occurs only within the gold lattice. In all of these experiments, it is important to accurately know the geometry and size of the contact region, but often this is difficult to quantify. By using FIM in our experiments, we were able to accurately control the tip radius (12.8 nm < tip radius < 21.6 nm) and our AFM instrument allowed us to measure indentation and adhesive forces to a resolution of 75 nN. This size regime falls in between that used by other researchers.

This thesis discusses several aspects of our instrumentation as well as results of several elastic/plastic deformation experiments. In Chapter 2, we summarize some recent theoretical and experimental nanoindentation experiments performed on gold surfaces reported in the literature. The experimental chamber and the components that are

essential to performing the nanoindentation experiments are detailed in Chapter 3. Chapter 4 describes the basic principles involved with Field Ion Microscopy (FIM) and how we fabricated and characterized our tungsten tips. Calibrations that were performed on a regular basis, along with detailed experimental procedures for our nanoindentation experiments are given in Chapter 5. Chapter 6 analyzes the experimental results and relates them to both continuum and atomistic theories of deformation. Finally, Chapter 7 lists the major conclusions of our work and suggests future research directions.

1.1 References for Chapter 1

1. National Science and Technology Council, Committee on Technology, Subcommittee on Nanoscale Science, Engineering and Technology, National Nanotechnology Initiative: The Initiative and its Implementation Plan, July 2000. Can be located at <http://nano.gov/nni2.htm#DocumentBody>.
2. Belak, J.F., MRS Bulletin 18 (5), 15 (1993).
3. Kaneko, R., Proceedings IEEE Micro Electro Mechanical Systems, 1 (1991).
4. Burnham, N.A. and Colton, R.J., Journal of Vacuum Science and Technology A 7, 2906 (1989).
5. Pethica, J.B. and Oliver, W.C., Physica Scripta T19, 61 (1987).
6. Pharr, G.M and Oliver, W.C., Journal of Materials Research 4, 94 (1989).
7. Page, T.F., Oliver, W.C., and McHargue, C.J., Journal of Materials Research 7, 450 (1992).
8. Johnson, K.L., Contact Mechanics, (Cambridge University Press, New York, 1985).

9 . Timoshenko, S., Theory of Elasticity, (McGraw-Hill Book Company, Inc., New York, 1934).

10 . Landman, U., Luedtke, W.D., Burnham, N.A., and Colton, R.J., Science 248, 454 (1990).

11 . Harrison, J.A., White, C.T., Colton, R.J. and Brenner, D.W., MRS Bulletin 18 (5), 50 (1993)

12 . Kelchner, C.L., Plimpton, S.J., and Hamilton, J.C., Physical Review B 58, 11085 (1998).

13 . Corcoran, S.G., Colton, R.J., Lilleodden, E.T., and Gerberich, W.W., Physical Review B 55, R16057 (1997).

14 . Cross, G., Schirmeisen, A., Stalder, A., Grütter, P., Tschudy, M., and Durig, U., Physical Review Letters 80, 4685 (1998).

15 . Michalske, T.A. and Houston, J.E., Acta Materialia 46, 391 (1998).

16 . Kiely, J.D., Jarausch, K.F., Houston, J.E., and Russell, P.E., Journal of Materials Research 14, 2219 (1999).

Chapter 2

BACKGROUND INFORMATION ON NANOMETER-SCALE DEFORMATION OF GOLD SURFACES

This chapter discusses the results of several nanoindentation studies reported in the literature for gold surfaces. These include theoretical simulations as well as nanoindentation experiments and neck formation experiments performed over a range of contact size regimes.

2.1 Theoretical Simulations of Nanocontacts

In 1990 Landman *et al.* [1] published results of a molecular dynamics simulation using a Ni (001) tip with a radius of curvature of ~30 Å indented into a Au (001) surface. Their calculations are modeled after the embedded-atom method [2], but their calculations do not include such forces as van der Waals forces which can be viewed as long-range interactions in the context of the embedded-atom method. The computations assumed an infinitely stiff cantilever with a nickel tip indented into gold at room temperature. The normal force of the tip on sample versus tip to sample displacement results are shown in Figure 2.1, this is a typical way to analyze indentation data. While the tip is approaching the surface, jump to contact is the first event to occur at point D. As the tip continues to approach the force starts to go to zero until point L where there is wetting of the tip as pile-up along the sides of the tip occurs to relieve stress under the tip. Upon further indentation, slip starts to occur along the (111) planes of the sample and interstitial defects are generated. At this point M, the edges of the surface zone of the tip are found to be in tension while the deformed region under the tip is in compression. The

maximum pressure occurs directly under the tip and a few nickel atoms diffuse into the surrounding gold substitutional sites.

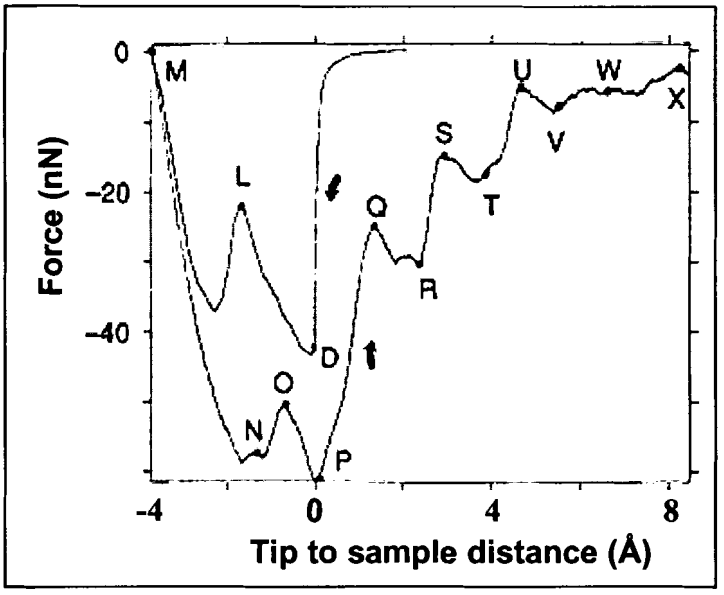

Figure 2.1: Nanoindentation simulation results from Landman *et al.* [1]. Force vs. tip to sample distance from a molecular dynamics simulation of a Ni (001) tip with a radius of curvature of ~ 30 Å indented into a Au (001) surface.

Upon withdrawal of the tip there is a mostly elastic response from points M to N. After point N, begins the process of a neck formation that consists mostly of gold atoms being pulled out of the contact. As the neck forms, atoms in adjacent layers of the neck disorder and then rearrange to form an added layer. Each time the neck maintains a layered crystalline structure until the disorder occurs, then a new layer is added. The reordering starts at points O, Q, S, and U. The cross sectional area of the neck decreases as it elongates. It is noticed that beyond the initial forming stages the number of atoms in the connective neck region remains roughly constant throughout the elongation process. The neck eventually breaks at a tip-to-sample distance of 18 Å leaving the nickel tip covered with gold. The normal pressure in the narrowest region of the neck remains roughly constant at ~10 GPa, throughout the necking process, and is found to increase by

~ 20% right before the structural rearrangements. These important results by Landman *et al.* were some of the first involving the behavior of nanometer sized contacts. Many of the features predicted in their force displacement curve have been qualitatively verified by experimental studies over the last decade.

More recently Kelchner *et al.* [3] did a simulation experiment using an 80 Å radius of curvature spherical tip indenting into a Au (111) surface. This model differs from Landman *et al.* in that it doesn't allow for adhesion between tip and sample and there is no friction. This situation is very similar to experiments conducted by Houston *et al.* [4,5] using thiol passivating layers on gold. The model is also very analogous to the continuum Hertzian contact model [6] which is explained in more detail in Section 6.3.2. Results of two different simulations are shown from Kelchner *et al.* in Figure 2.2. One result shows retraction after the first yield event and the second result shows retraction after the second yield event. The simulation shows that yield events happen on a very short time scale. Their molecular dynamics simulation was run long enough to see the dislocation loops equilibrate, which was on the order of picoseconds.

Deformations in the substrate were tracked by using the centrosymmetric property of gold. A centrosymmetric material is one where each atom has pairs of equal and opposite bonds to its nearest neighbors. For a homogeneous elastic deformation these bonds will lengthen and/or change direction in such a way that they remain equal and opposite. When a defect occurs there is no longer an equal and opposite relation for the nearest neighbor pairs and the symmetry is broken.

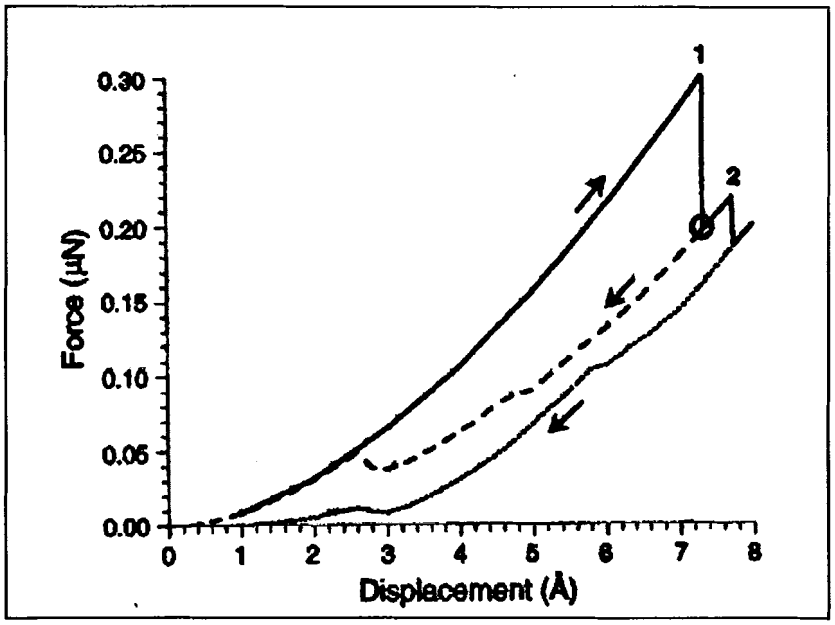

Figure 2.2: Nanoindentation simulation results from Kelchner *et al.* [3]. Computer simulation that uses an 80 Å radius of curvature spherical tip indenting into a Au (111) surface. The model allowed for no adhesion or friction between tip and sample. The solid line shows the insertion region while the dotted lines show the retraction region. One retraction occurs after the first yield event while the second retraction occurs after the second yield event.

The centrosymmetric quantity P is defined as

$$P = \sum_{i=1,6} \left| \mathbf{R}_i + \mathbf{R}_{i+6} \right|^2, \tag{2.1}$$

where $\mathbf{R}_i$ and $\mathbf{R}_{i+6}$ are the vectors or bonds corresponding to the six pairs or opposite nearest neighbors in the fcc lattice of the gold substrate. When $P = 0$ the crystal is a perfect lattice, but when the lattice incorporates defects, P becomes nonzero. After an indent, based on ranges for P values, Kelchner *et al.* [3] were able to characterize the atoms in the bulk gold according to whether they were surface atoms, partial dislocations or stacking faults. The stacking faults were found to be bounded by partial dislocation loops, and it was found that all the defects lie on {111} planes. For a tip displacement of about 7 Å the partial dislocation loops that initiated at the surface, went as deep as 85 Å.

It was found that partial dislocation loops first appear with mirror symmetry on either side of the tip apex, at a distance approximately half of the contact radius below the surface. The loops occur on planes that are 71° from the surface plane. This is in disagreement with what is predicted in Hertzian mechanics. For nucleation dislocation to occur, a commonly used criterion is that the maximum resolved shear stress (MRSS) exceeds the critical shear stress (CSS) [7]. In continuum Hertzian contact theory [6] the MRSS occurs on the indenter axis and on a plane that is 45° from the axis. In their simulation, Kelchner *et al.* found that the MRSS was 7 GPa immediately before the first yield event. The CSS was calculated to be 2 GPa by deriving it from the potential used in the simulation. Since the MRSS greatly exceeded the CSS, they proposed a new criterion for dislocation nucleation to occur on this atomistic scale which states: the work done over the displaced surface must be greater than the line energy of the new dislocation loop.

2.2 Elastic and Plastic Deformation Studies of Nanocontacts

Perhaps the earliest paper that presented experimental results of small-scale nanoindentations on gold surfaces was presented by Burnham and Colton in 1989 [8]. The experiment was performed using an AFM that contained an STM used to measure the deflection of the cantilever beam. The experiments were performed in air under ambient conditions with a cantilever spring constant of 50 N/m. For their initial experiment the tip radius of curvature was about 100 - 200 nm as determined from scanning electron microscopy (SEM) and was indented into a thick gold foil. This was a deep indentation with a penetration depth about 103 nm and a corresponding force of 20.3 μN. The indentation was found to be totally plastic and a hardness value of 0.65

GPa was calculated. Burnham and Colton also reported a few other experiments, involving smaller indentations (~ nanometers to tens of nanometers), on a 100 nm thick gold film deposited on a glass substrate. The tip radius was unknown and sample cleanliness was not controlled. No jump to contact was noticed for these smaller contacts, but there was adhesion and hysteresis in the force vs. displacement curves.

In 1997, Colton's laboratory performed a more controlled experiment [9] with a commercial Hysitron, Inc. Picoindenter® used in conjunction with a Digital Instruments, Nanoscope™ III AFM/STM. The indentations were performed in a dry N_2–purged glove bag. A Berkovich diamond, with a spherical radius of curvature ~ 205 nm determined by imaging the tip with an asperity on the gold surface, was used as the tip. The indentation samples were carefully cleaned gold single crystals oriented in the [111], [110] and the [100] directions. The penetration depths of the indents ranged from 7 to 50 nm. During the insertion portion of the indents, displacement excursions were noticed following the initial elastic regime as shown in Figure 2.3. The first displacement excursion corresponds to the initiation of plastic behavior (the yield point) of the gold sample. Yield point values varied between 3 GPa for Au (111) and 8.5 GPa for Au (100), but the yield point was found to depend on the surface roughness of the sample. As the surface roughness increased, these values were found to decrease. The area of contact between the tip and sample was calculated assuming Hertzian contact. Hardness values calculated immediately before and after the tip excursions ranged from 0.6 to 2.4 GPa. Corcoran *et al.* [9] analyze the data assuming that a single displacement excursion is started by a single dislocation event. This first dislocation event acts as a Frank-Read source, which eventually creates a dislocation pileup under the indenter. There is some discrepancy

between this interpretation and their experimental results due to the fact that the model does not take into account the interaction of dislocations on parallel slip bands. Reports from this study did not discuss or show any regions of negative force on the force vs. indentation depth curves.

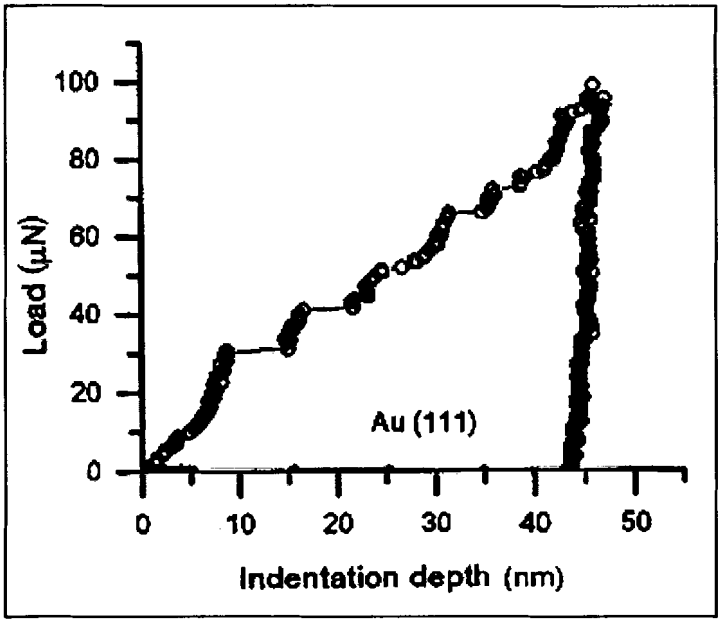

Figure 2.3: Experimental nanoindention results from Corcoran *et al.* [9]. Berkovich diamond tip with tip radius = 205 nm on a Au (111) surface.

Houston *et al.* have performed many nanoindentation experiments on gold [4,5,10,11,12,13,14,15] with the surface coated with a self-assembled monolayer (SAM) so as to avoid adhesion between tip and sample. No attractive force at all is observed on these surfaces at the beginning of the indent [4], due to the fact that the SAM has low surface energy. Their experiments were all performed with the interfacial-force microscope (IFM) [16,17]. The main advantage of the IFM is that it avoids any jump to contact by using a force feed back system that uses capacitance to detect displacement and then applies a voltage to rebalance the displacement. The passivating layer allows the data to be analyzed using continuum Hertzian theory, which inherently assumes no

adhesion. Despite the fact that their earlier experiments were done in air [16], in liquid hexadecane [10,11,12], or in a pumped out region that was backfilled with nitrogen [4], the Hertzian theory matches their data well. They also observed features in the force versus displacement curves due to multiple plastic events [15] similar to Corcoran *et al.* results [9]. For this work, the range of tip radii varies from 25 to 500 nm and the indentation depths range between 2.5 and 70 nm. In earlier experiments the tip radii were determined from SEM, and in later experiments the radii were determined by field emission scanning electron microscopy (FESEM).

Several interesting physical phenomena were extracted from data on gold by Houston *et al.* Their experiments probed slip along grain boundaries [10,11], lower yield stresses near surface steps [11,13], shear stress dependence as a function of tip radius [12], differences in nanomechanical properties between (111), (001), and (110) gold orientations [14], and the initial stages of indentation which included comparing the depth of the plastically deformed holes with their respective widths [15]. It was found that the maximum shear stress (MSS) increases as the tip radius decreases for a (111) gold crystal [12]; the MSS was measured to be 3 GPa for a 250 nm tip and 5 GPa for a 50 nm tip. A dislocation nucleation mechanism was proposed to explain the initial deviation of the force vs. displacement curve from ideal Hertzian behavior. Houston *et al.* also found that when different orientations of gold surfaces were examined, the elastic modulus of the (111) orientation was similar to (110) but greater than the (001) orientation [14]. In fcc materials such as gold, slip occurs on close-packed {111} planes in ⟨110⟩ directions. Using this fact, they resolved the MSS in the direction of primary

slip for indents done in the three different crystals and found a value of about 1.8 GPa for all orientations.

Grütter *et al.* have recently used FIM to characterize a tungsten tip in atomistic detail before and after nanoindentation into gold [18,19,20,21,22] at 150 K in UHV. In their experiments, sharp W (111) tips with radii ≤ 3.0 nm were indented into 100 nm thick Au (111) film surfaces that were evaporated onto a cleaved mica substrate. Penetration depths were limited to < 2.5 nm and the corresponding forces were < 300 nN. This approach is very similar to ours but covers a smaller size regime; discussion of the similarities and differences in results are discussed in Chapter 6. FIM results by Grütter *et al.* show no significant damage to the tungsten tip caused by indentation. Indentation results for force vs. rigid body separation were found to be fairly consistent with both the Maugis-Dugdale theory [23] and the Rose-Ferrante-Smith theory [24,25] except for a long range adhesion force upon insertion and during withdrawal. No adequate model was found to fully explain this long range force.

2.3 Neck Formation at Nanocontacts

Groups have performed experiments to analyze neck formation and degradation during indentation of a gold tip into a gold surface [26,27,28,29,30,31,32]. Up to this point we have been discussing indentation experiments in which the tip is much harder than the sample to avoid any plastic deformation of the tip. The necking experiments, however, focus on the dynamics of the neck formation and adhesion effects, and thus the same material is used for the tip and the sample. Tip radii are not reported in these experiments since the tip becomes drastically modified during contact formation and breakage.

During the neck formation experiments at gold/gold contacts, electrical current through the neck was measured. As the neck expands or contracts, quantized steps are measured in conductance vs. displacement graphs with units of integer values of $2e^2/h$. There is uncertainty as to whether the steps are due to conductance quantization or due to atomic rearrangements themselves [33,34]. These conductance steps having dimensions on the order of 2 Å (~ atomic spacing of gold), were found to correlate with quantized steps in force vs. displacement graphs [26,27,31,32], suggesting that the quantization is due to atomic rearrangements. Additionally, conductance steps were found to be independent of temperature.

Agrait *et al.* performed experiments where the neck was repeatedly lengthened and shortened. They estimated the yield strength of gold to be 3 to 6 GPa [26,27].by measuring the pressure at the beginning of the conductance steps. Pressure was measured from the force and contact area (determined from the conductance value). Stalder and Durig measured a yield strength of 5 to 8 GPa at the point of neck breakage [31,32]. These yield strengths are similar to the values found in the nanoindentation experiments in Section 2.2.

It is instructive to consider specific results of a necking experiment performed by Stalder and Durig [31,32] as shown in Figure 2.4. These results reveal four different phases of the nanoindentation process. As the tip and sample first approach one another, an attractive force exists between the tip and sample. This leads to electrical contact with the connective neck being in a strong tensile stress state. As plastic flow is initiated during insertion, the neck diameter increases rapidly with indentation depth. During the next phase, the neck experiences compressive stress and its diameter grows at a slower

rate. This can qualitatively be explained by the fact that for compressive loading the maximum shear stress is within the substrate at a depth comparable to the contact radius, yet for tensile loading the maximum shear stress is located close to the perimeter of the contact. Tensile loading at the perimeter makes it easier for the neck to grow.

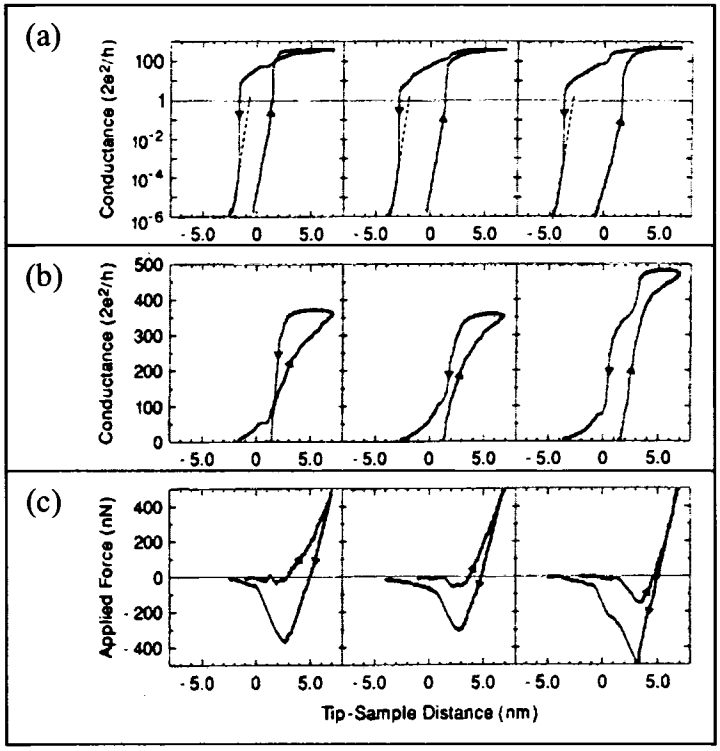

Figure 2.4: Necking experiment at a gold/gold contact from Stalder and Durig [31]. Electrical conductance (a) on a logarithmic scale, (b) on a linear scale, and (c) applied force vs. tip-sample displacement. Data of three representative examples are shown. Approach and retraction are indicated by arrows.

During retraction of the tip, the neck diameter remains relatively constant (unlike during insertion) as the tensile stress increases. When the tensile stress reaches a critical value, the neck diameter starts to decrease more dramatically as the tensile force decreases. The tensile force is reduced at a slower rate than the rate of neck diameter shrinkage. Eventually the stress can no longer be sustained and the neck breaks.

Both these necking experiments as well as the nanoindentation experiments discussed in Section 2.2 show many of the same features that we observe in our experiments (see Chapter 6). Continued work by several research groups over a large range of contact size and material characteristics will improve the overall understanding of the systems.

2.4 References for Chapter 2

1. Landman, U., Luedtke, W.D., Burnham, N.A. and Colton, R.J., Science 248, 454 (1990).
2. Foiles, S.M., Baskes, M.I., and Daw, M.S., Physical Review B 33, 7983 (1986).
3. Kelchner, C.L., Plimpton, S.J., and Hamilton, J.C, Physical Review B 58, 11085 (1998).
4. Thomas, R.C., Houston, J.E., Michalske, T.A., and Crooks, R.M., Science 259, 1883 (1993).
5. Joyce, S.A., Thomas, R.C., Houston, J.E., Michalske, T.A., and Crooks, R.M., Physical Review Letters 68, 2790 (1992).
6. Johnson, K.L., Contact Mechanics, (Cambridge University Press, Cambridge, 1985).
7. Hirth, J.P. and Lothe, J., Theory of Dislocations, (Krieger, Malabar, FL, 1982).
8. Burnham, N.A. and Colton, R.J., Journal of Vacuum Science and Technology A 7, 2906 (1989).
9. Corcoran, S.G., Colton, R.J., Lilleodden, E.T., and Gerberich, W.W., Physical Review B 55, 16057 (1997).

10. Tangyunyong, P., Thomas, R.C., Houston, J.E., Michalske, T.A., Crooks, R.M., and Howard, A.J., Physical Review Letters 71, 3319 (1993).

11. Tangyunyong, P., Thomas, R.C., Houston, J.E., Michalske, T.A., Crooks, R.M., and Howard, A.J., Journal of Adhesion Science and Technology 8, 897 (1994).

12. Michalske, T.A. and Houston, J.E., Acta Metallurgica 46, 391 (1998).

13. Keily, J.D., Hwang, R.Q., and Houston, J.E., Physical Review Letters 81, 4424 (1998).

14. Keily, J.D. and Houston, J.E., Physical Review B 57, 12588 (1998).

15. Keily, J.D., Jarausch, K.F., Houston, J.E., and Russell, P.E. Journal of Materials Research 14, 2219 (1999).

16. Joyce, S.A. and Houston, J.E., Review of Scientific Instruments 62, 710 (1991).

17. Houston, J.E. and Michalske, T.A., Nature 356, 266 (1992).

18. Cross, G., Schirmeisen, A., Stalder, A., and Grütter, P., Physical Review Letters 80, 4685 (1998).

19. Schirmeisen, A., Cross, G., Stalder, A., Grütter, P., and Durig, U., Applied Surface Science 157, 274 (2000).

20. Schirmeisen, A., Cross, G., Stalder, A., Grütter, P., and Durig, U., New Journal of Physics 2, 29.1 (2000).

21. Cross, G., Mechanics of Nanometer Scale Indentation of a Metal Surface, Ph.D. thesis, McGill University, Montreal, Quebec, Canada, 1999.

22. Schirmeisen, A., Metallic Adhesion and Tunneling at the Atomic Scale, Ph.D. thesis, McGill University, Montreal, Quebec, Canada, 1999.

23 . Derjaguin, B.V., Muller, V.M., and Toporov, Y.P., Journal of Colloid Interface Science 53, 314 (1975).

24 . Rose, J.H., Smith, J.R., and Ferrante, J., Physical Review Letters 47, 675 (1981).

25 . Ferrante, J. and Smith, J.R., Physical Review B 31, 3427 (1985).

26 . Agrait, N., Rubio, G., and Viera, S., Physical Review Letters 74, 3995 (1995).

27 . Rubio, G., Agrait, N., and Viera, S., Physical Review Letters 76, 2302 (1996).

28 . Sanchez-Portal, D., Untiedt, C., Solar, J.M., Saenz, J.J., and Agrait, N., Physical Review Letters 79, 4198 (1997).

29 . Scheer, E., Agrait, N., Cuevas, J.C., Yeyati, A.L., Ludolph, B., Martin-Rodero, A., Bollinger, G.R., van Ruitebeek, J.M., and Urbina, C., Nature 394, 154 (1998).

30 . Yanson, A.I., Bollinger, G. Rubio, van den Brom, H.E., Agrait, N., and van Ruitenbeek, J.M., Nature 395, 783 (1998).

31 . Stalder, A. and Durig, U., Journal of Vacuum Science and Technology B 14, 1259 (1996).

32 . Stalder, A. and Durig, U., Applied Physics Letters 68, 637 (1996).

33 . Brandbyge, M. *et al.*, Physical Review B 52, 8499 (1995).

34 . Sirvent, C., Rodrigo, J.G., Agrait, N., and Viera, S., Physica B 218, 238 (1996).

Chapter 3

ULTRA-HIGH VACUUM INSTRUMENT THAT COMBINES ATOMIC FORCE MICROSCOPY (AFM), SCANNING TUNNELING MICROSCOPY (STM) AND FIELD ION MICROSCOPY (FIM)

A large effort went into the design and construction of an ultra-high vacuum (UHV) system that combines atomic force microscopy (AFM), scanning tunneling microscopy (STM), and field ion microscopy (FIM). This chapter discusses the main hardware components and their specifications.

3.1 Ultra-High Vacuum Chamber

The ultra-high vacuum chamber (UHVC) which houses the three microscopes routinely achieved base pressure $< 2 \times 10^{-11}$ torr after being baked out. The pumping consists of one Leybold-Heraus model D4AC mechanical pump, one Leybold-Heraus model TURBOVAC 150 turbo pump, and one Perkin-Elmer Ultek Inc. ion pump. The system has three main sections (Figure 3.1), the sample introduction chamber, the sample characterization chamber, and the AFM/STM/FIM experimental chamber. All three chambers can be valved off from one another. The UHVC is mounted on a TMC Micro-g model 65-22801-01 compressed air vibration isolation system.

The sample introduction chamber is used to introduce the sample and force sensor into the system. A transfer arm moves them between the sample characterization and experimental chamber. Details of a novel transfer and docking mechanism are discussed in Appendix A.

The sample characterization chamber includes a Balzers model QMG 112 mass spectrometer (for leak testing), an electron beam heater (for annealing the sample), a Physical Electronics model 15-110 single pass Auger electron spectrometer (AES) and a Physical Electronics model 20-115 ion gun. The sample is docked onto the end of a Huntington model PM-600-XYZ-RC rotateable x,y,z manipulator. While on the manipulator, the sample can be checked for cleanliness by AES, cleaned with the ion gun or annealed with the electron beam heater. After cleaning and characterizing the sample, it is transferred to the experimental chamber where the AFM/STM/FIM head is located.

3.2 AFM/STM/FIM Head

The AFM/STM/FIM head (Figure 3.2) contains the major parts of the three microscopes. These components are the Inchworm® [1] and the piezoelectric scanner tube (PST), the force sensor, the interferometer, and the microchannel plate (MCP) which is discussed in the next chapter. The Inchworm® and the MCP are mounted on a slide so that alternating between AFM/STM mode and FIM mode can quickly be achieved by merely pushing or pulling the slide.

3.2.1 Inchworm® and Piezoelectric Scanner Tube (PST)

The sample is mounted onto the end of the PST. A course approach, performed by an Inchworm® translator, brings the sample close to the tip. Then, a computer controlled algorithm is used to control the final approach of the sample to the tip via expansion of the PST, along the z direction.

The final approach uses both the Inchworm® and the PST (Figure 3.3). The PST has four silver electrodes on the exterior that extend the length of the tube and the inside is coated with silver to make another electrode. The tube can be bent in the x direction

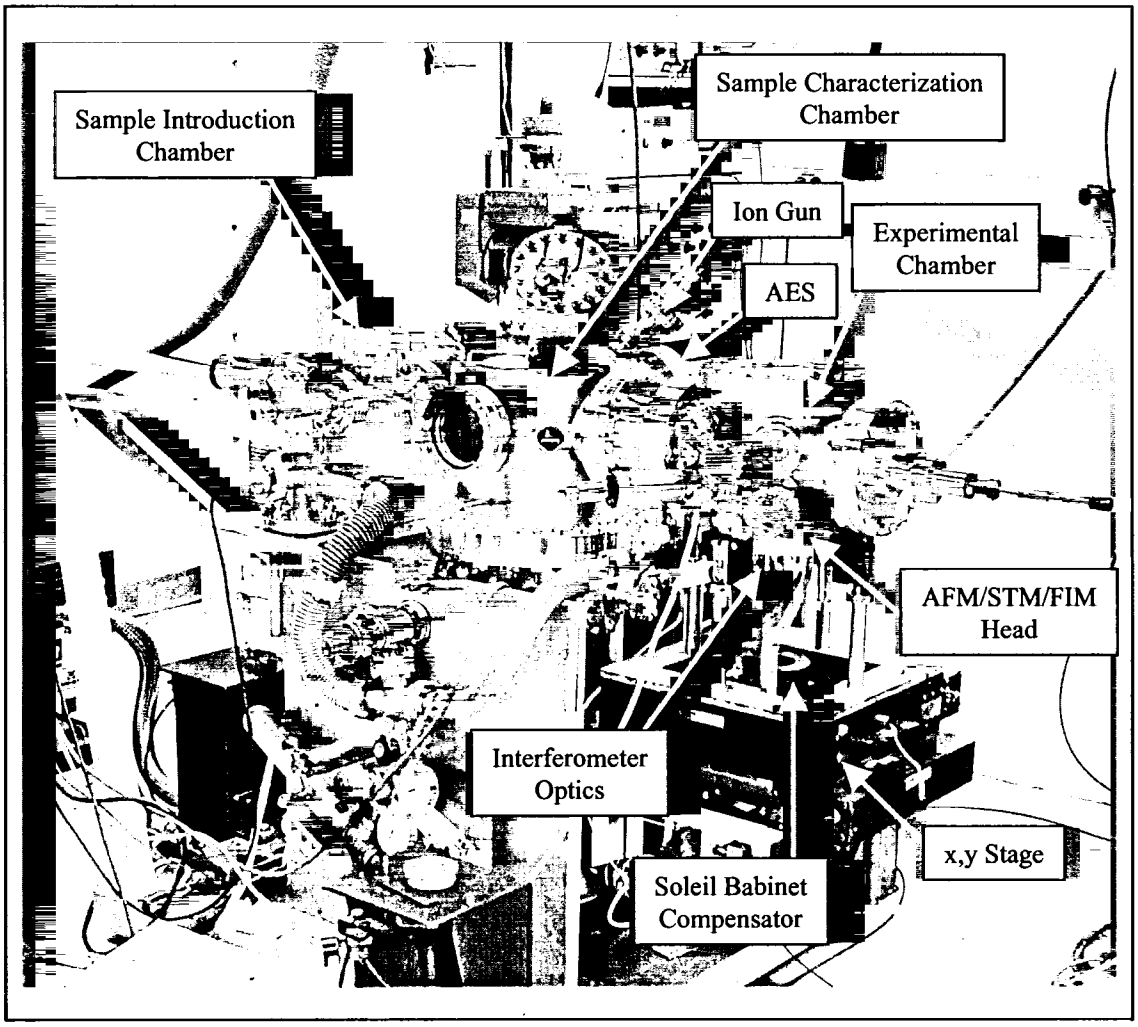

Figure 3.1: Photograph of the ultra-high vacuum chamber (UHVC).

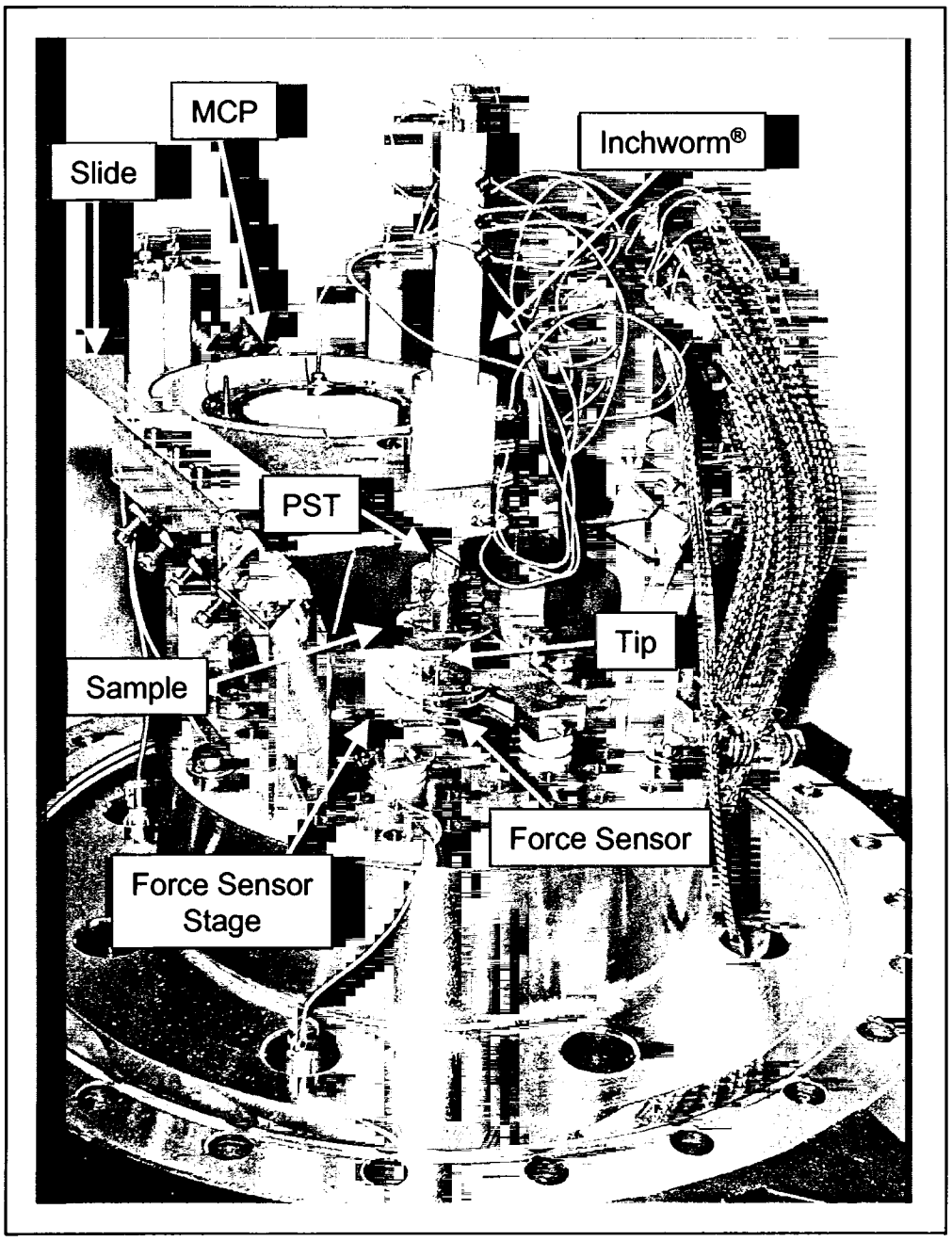

Figure 3.2: Photograph of the AFM/STM/FIM head.

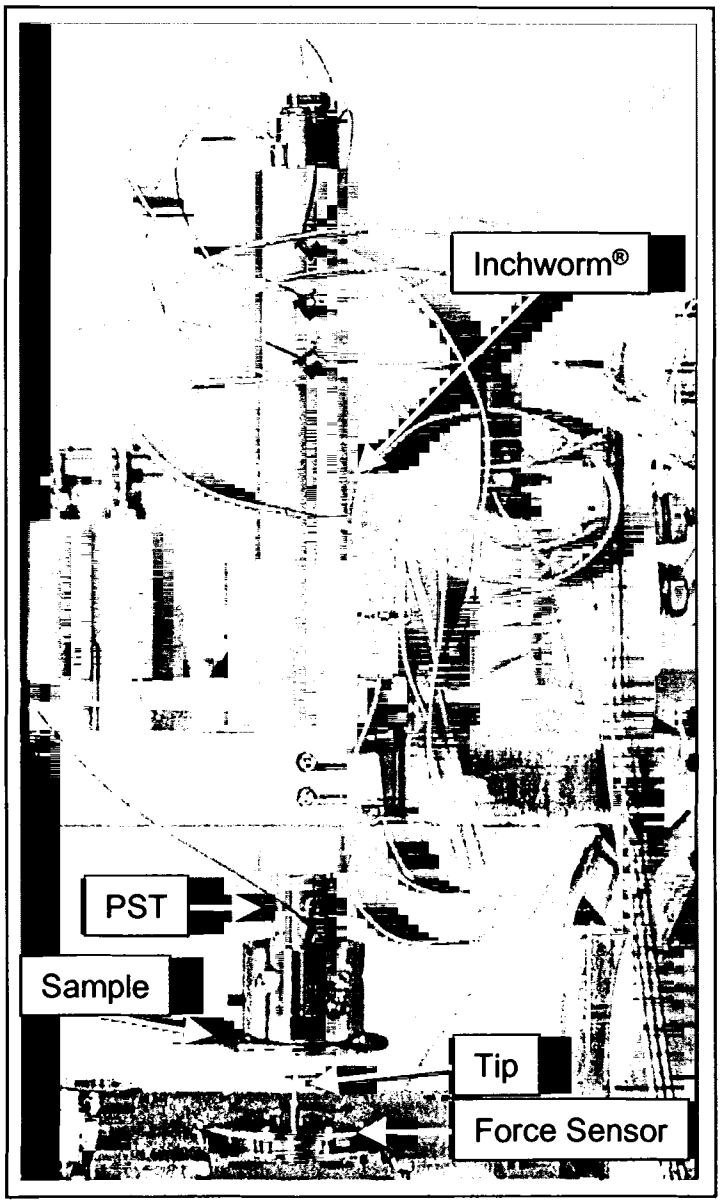

Figure 3.3: Photograph of the Inchworm® and the piezoelectric scanner tube (PST).

by applying voltage to two opposing quadrants of the PST or can be bent in the y direction by applying voltage to the other two opposing quadrants. The tube can be lengthened or shortened by applying voltage on the inner electrode relative to the quadrants' voltages. Typically, between + 60 V and – 60 V was applied to x and y direction quadrants, which yielded a displacement of about 4.5 μm in the x and y directions. For the z direction, + 60 V and – 60 V provided a range of about 1 μm. Several times the PST was broken and needed replacing. Buying a new Inchworm® with a PST inside is expensive, so we developed an interchangeable piezo design that allows easy interchange of the PST inside the Inchworm®. Details of this design are in Appendix B.

In our instrument the sample is mounted on a holder made out of Carpenter HYMU "80"® Alloy [2]. This holder is held in place on the end of the PST. During the final approach, the Inchworm® advances toward the tip then stops. Next the PST advances forward in much smaller increments to see if the tip and sample are close enough to trigger the current setpoint. If the setpoint has not been reached then the PST retracts and the Inchworm® advances again. The Inchworm® never advances more than the PST advances. After the final approach has been completed and the tip is in tunneling contact, only the PST is used for the feedback. The tunneling current goes through a current-to-voltage converter consisting of a AD549L monolithic electrometer operational amplifier and an AD524 precision monolithic instrumentation amplifier, which are both made by Analog Devices, Inc. [3]. The voltage output of the converter goes to the STM module (see Section 3.3).

3.2.2 Force Sensor

The tip is mounted in a crosshair force sensor (Figure 3.4). The crosshair geometry eliminates lateral force components and allows only a normal force. The first generation sensor was designed and built by Richardson and Unertl [4]. Several improvements were subsequently made.

In our crosshair force sensor, a tip is held in place by an IC socket that is press fitted into a tip holder. The tip holder has machined grooves which guide four wires that hold the tip holder in place. The force sensor that we used for the indentation experiments was made from tantalum wire using a special jig. The wires were epoxied to the force sensor body and then spot welded. The whole force sensor was cast into an epoxy resin for polishing. The back of the tip holder and four pads on the back of the force sensor body were simultaneously polished (see Figure 3.4b) to insure that all reflective surfaces were parallel. Acetone was used to dissolve the epoxy and then the force sensor was calibrated as described in Section 5.1.2. During an indentation experiment a reference laser beam is reflected off the back of the force sensor body and another laser beam is reflected off the back of the tip holder. As the tip moves, a differential polarized interferometer determines how far the tip has moved. By knowing the force constant of the force sensor, the force exerted by the tip can be calculated from its displacement.

There were some problems with the force sensor that we used for our experiments. Wiring the force sensor and polishing were very lengthy procedures. Also there was no quantitative way to control the tension in the wires, hence the tensions on the tip holder may not have been uniform. This lead to a large uncertainty in the force

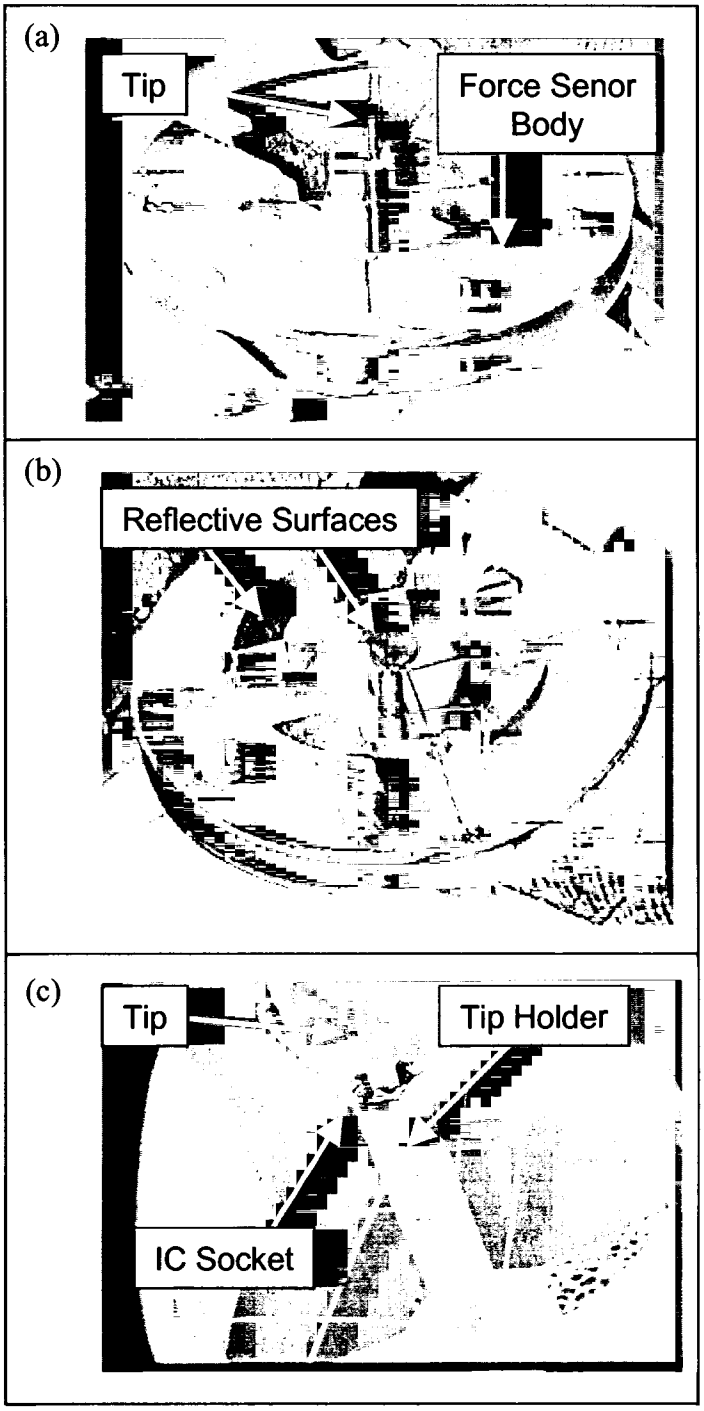

Figure 3.4: Crosshair force sensor. (a) Top view. (b) Bottom view. (c) SEM image.

constant value. We recently developed a method to control the wire tension with a new "tensioner" jig that yielded a predictable spring constant. This new tensioner force sensor design was tested but never used in an actual experiment. A theoretical model that was developed for our force sensor and results of our new tensioner design are discussed in Section 5.1.2.

In the new force sensor design, the reflective pads consist of parallel mirrors attached to the back of the tip holder and force sensor body using UHV compatible epoxy. A special tensioner jig was designed so that adjustable tensions could be applied to all the individual wires (Figure 3.5) which were made of 0.102 mm diameter aluminum. Aluminum was chosen due to its ease of wire bonding to the stainless steel force sensor body. To obtain a desired force constant, we used the model in Section 5.1.2 to determine the tension in the wires. A thin metal rod was calibrated to touch a flat beam and make electrical contact at the predetermined tension when the rod was flexed. These thin metal rods were used to pull the wires and create the tension. The aluminum wires were held in place using UHV compatible epoxy and then wire bonded to the force sensor body. This new method of making force sensors is very reliable and yields a better defined spring constant.

Once the tip is positioned in the force sensor, it is inserted into vacuum via the load lock. The transfer arm can be used to dock or undock the force sensor thereby allowing tip change or resharpening. The force sensor is held in place by spring clips on the force sensor stage.

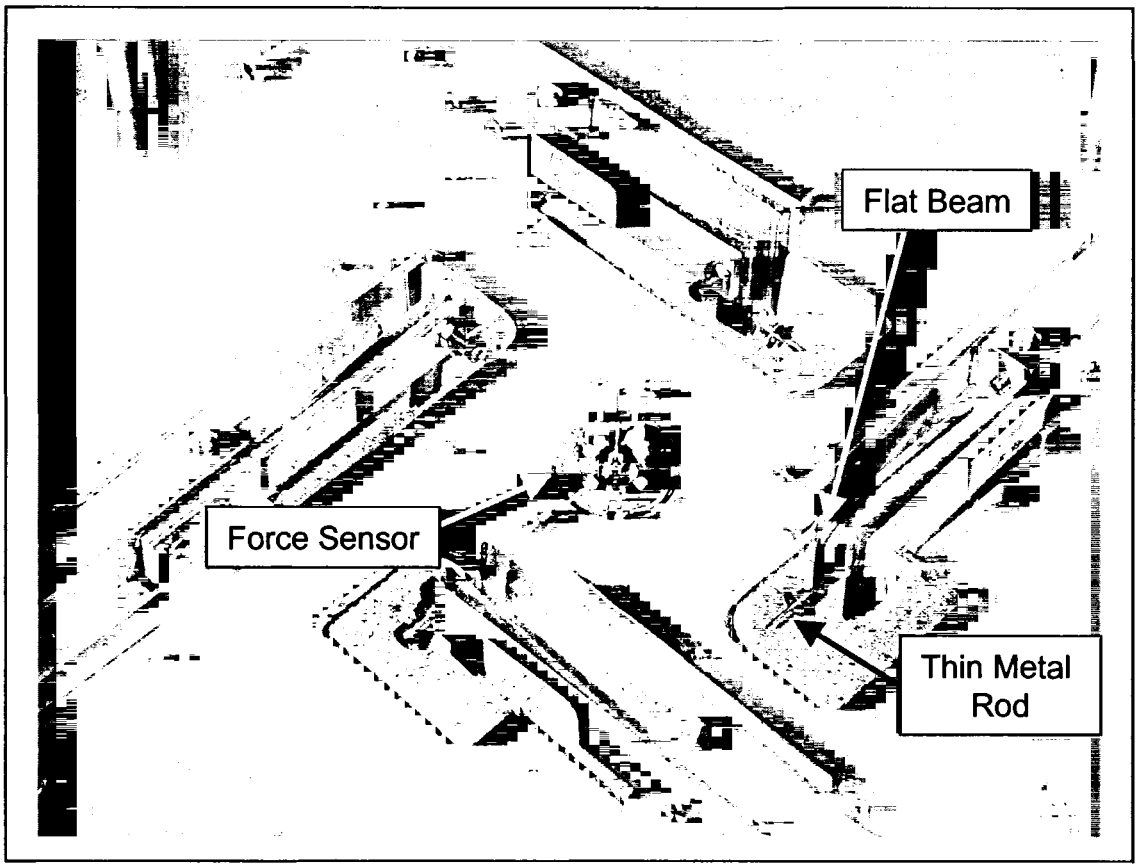

Figure 3.5: Tensioner jig used to construct new force sensors.

3.2.3 Interferometer

The interferometer that measures tip displacement is a differential polarized interferometer based on the design by Schonenberger and Alvarado [5]. This type of interferometer minimizes the concern for variations in refractive index and light intensity, due to the fact that path differences between differential beams are small and the signal gets normalized. The interferometer mount is located outside the vacuum. A window on the vacuum flange allows the laser beams to enter into the UHVC and reflect off the force sensor. A Melles Griot HeNe laser (model 05LHP111) and interferometer optics are mounted on a x,y stage that also has rotational motion. This allows the beams to be properly aligned on the back of the force sensor. Each time a force sensor is moved on the force sensor stage, a realignment was required. The starting position of the interference fringes prior to the indentation experiments was adjusted using a Soleil Babinet compensator in between the laser and the interferometer optics.

The output of the interferometer optics yields two different concentric ring patterns that are independently measured by two photodetectors. These two signals, A and B, are sent into a current-to-voltage converter circuit. The signals are subtracted from one another and then divided by their sum; i.e. (A - B)/(A + B). An AD734 four-quad analog multiplier from Analog Devices, Inc. [3] performs this normalizing function. The normalized signal is sent to the AFM module, which is discussed in Section 3.3.

3.3 Electronics for AFM/STM/FIM Head

The electronics that control the AFM/STM/FIM head (Figure 3.6) were mostly built in house by Marius Enachescu [6]. This instrument control and data acquisition electronics were based on a design by Steven M. Clark [7]. The Inchworm® was

controlled by the ARIS®-950 [8] Inchworm® controller. The software that controlled the electronics was based on software written by David Baselt [9].

The heart of the electronics control is the digital signal processing board (DSP) from Spectrum Signal Processing Inc. (model TMS320C30) [10]. The DSP was housed inside a 486-D0 processor based computer. The DSP communicated with an interface enclosure via a ribbon cable. Inside the interface enclosure there are six different modules plugged into the ribbon bus. They are the Inchworm®, AFM, STM, x, y and z/tip modules.

The first module is the Inchworm® module which takes information from the DSP about the clock frequency. This in turn is fed to the ARIS®-950 controller which controls the approach rate of the Inchworm®.

The AFM module uses an AD7884, 16-bit monolithic analog-to-digital converter (ADC) from Analog Devices, Inc. [3]. This module takes the normalized analog signal from the interferometer current-to-voltage converter and sends it to the computer.

The STM module is the same as the AFM module except that it has a logarithmic amplifier section so that the electronics can better react to the exponential dependence of tip to sample tunneling current.

The x module contains a PCM53, 16-bit monolithic digital-to-analog converter (DAC) by Burr-Brown Corp. [11]. The PCM53 takes the digital signal sent from the DSP and turns it into an analog voltage. This voltage is then split into itself and an inverted signal. These signals are amplified using PA83 high voltage operational amplifiers from Apex Microtechnology Corp. [12]. The outputs of the PA83's are used to apply voltage to two opposing quadrants on the PST.

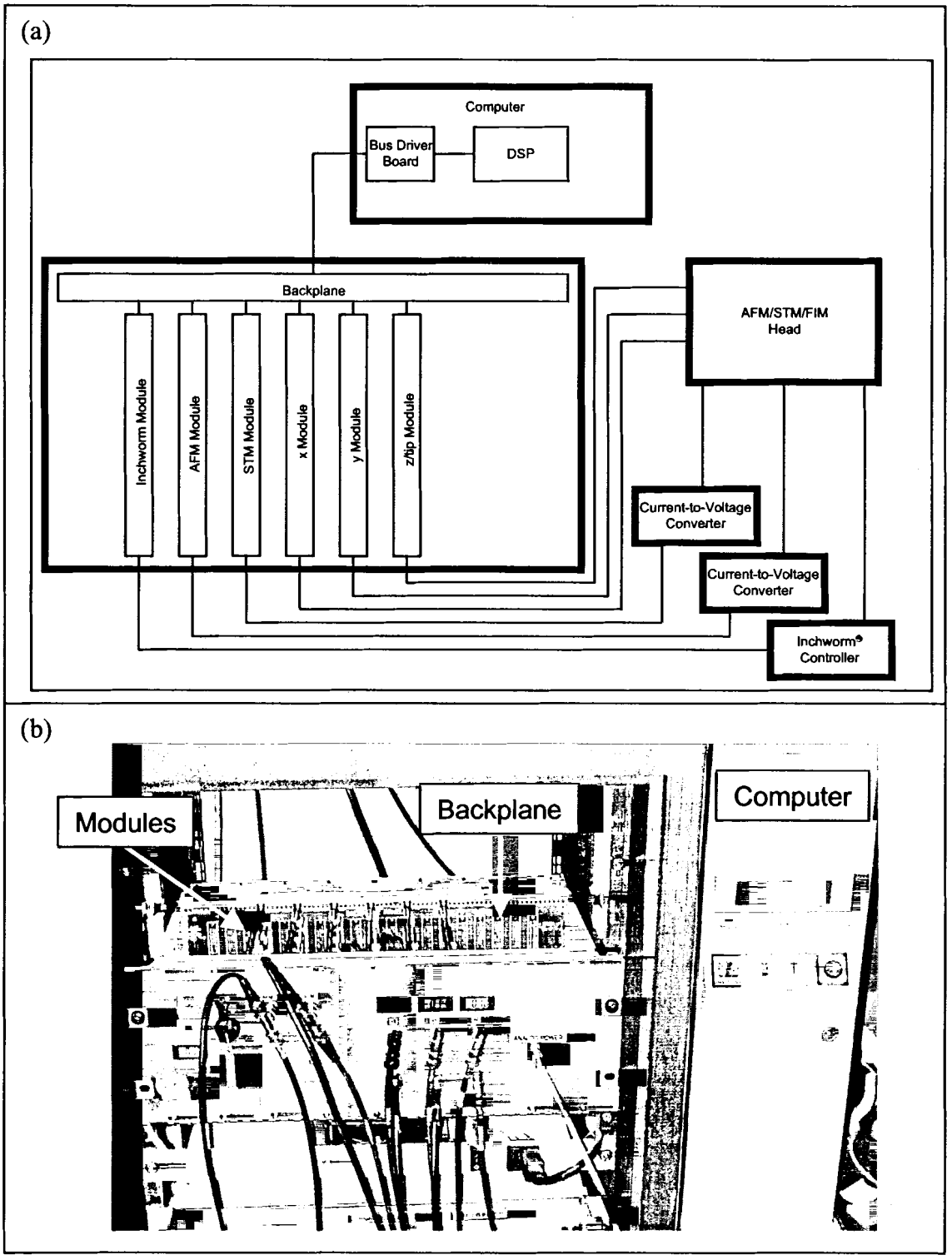

Figure 3.6: Electronics that control the AFM/STM modes. (a) Block diagram. (b) Photograph.

The y module is built the same as the x module. The output of this module is used to apply voltage to the two other opposing quadrants on the PST. The z/tip module is very similar to the x module except that there are two PCM53 chips. The output of one PCM53 is amplified using a PA83. This output is used to apply voltage to the center electrode of the PST. The output of the other PCM53 is used to apply voltage to the tip for STM.

3.4 References for Chapter 3

1. Inchworm® is a registered trademark of Burleigh Instruments, Inc., Burleigh Park, Fishers, NY 14453.
2. Carpenter HYMU "80"® is a registered trademark of Carpenter Technology Corporation,101 W. Bern St., Reading, PA 19612-4662.
3. Analog Devices, Inc., One Technology Way, P.O. Box 9106, Norwood, MA 02062.
4. Richardson, C., senior project report with advisor Unertl, W., Department of Physics and Astronomy, The University of Maine, Orono, ME 04469.
5. Schonenberger, C. and Alvarado, S.F., Review of Scientific Instruments 60, 3131 (1989).
6. Enachescu, M., currently employed at Lawrence Berkeley Laboratory at the University of California, Berkeley, CA 94270.
7. Clark, S.M., Advances in Scanning Force Microscopy, Ph.D. thesis, California Institute of Technology, Pasadena, CA, 91125, 1992.
8. ARIS® is a registered trademark of Burleigh Instruments, Inc., Burleigh Park, Fishers, NY 14453.

9 . Baselt, D., Ph.D. thesis, California Institute of Technology, Pasadena, CA 91125, 1993.

10 . Spectrum Signal Processing Inc., One Spectrum Court, #200, 2700 Production Way Burnaby, BC, Canada V5A 4X1.

11 . Burr-Brown Corporation, P.O. Box 11400, Tucson, AZ 85734.

12 . Apex Microtechnology Corporation, 5980 N. Shannon Road, Tucson, AZ 85741-5230.

Chapter 4

SHAPING AND CHARACTERIZATION OF TUNGSTEN PROBES USING FIELD ION MICROSCOPY (FIM)

4.1 Field Ion Microscopy (FIM)

FIM was the first microscopy to achieve atomic resolution as demonstrated by Erwin Muller in 1951 [1]. The technique takes advantage of an extremely high electric field located at the apex of a sharp tip. This large electric field is used to locally ionize helium atoms whose trajectories map out the surface of the tip apex.

A typical FIM setup (Figure 4.1) located inside a vacuum chamber includes a sharp tip that can range in sharpness from a single atom terminated tip to one having a ~ 200 nm radius of curvature. A voltage is applied such that there is a high positive tip potential relative to a phosphorescent target, thereby producing an electric field strength ~ 4 V/Å. As the chamber is filled with an inert gas such as helium to a pressure ~ 10^{-6} to 10^{-3} torr, the electric field causes the gas atoms to be polarized. The polarized atoms are attracted toward the apex of the tip where the electric field is largest. In a region just outside the apex of the tip, the magnitude of the electric field is strong enough to cause the electrons in the polarized molecules to tunnel into the tip, leaving an ion that is strongly repelled radially from its point of origin. The ions collide with the phosphorescent target to produce a visible image. Due to the radial ion trajectories the apex surface image is magnified on the phosphorescent screen. The magnification is approximately equal to the tip to screen distance divided by the tip radius of curvature,

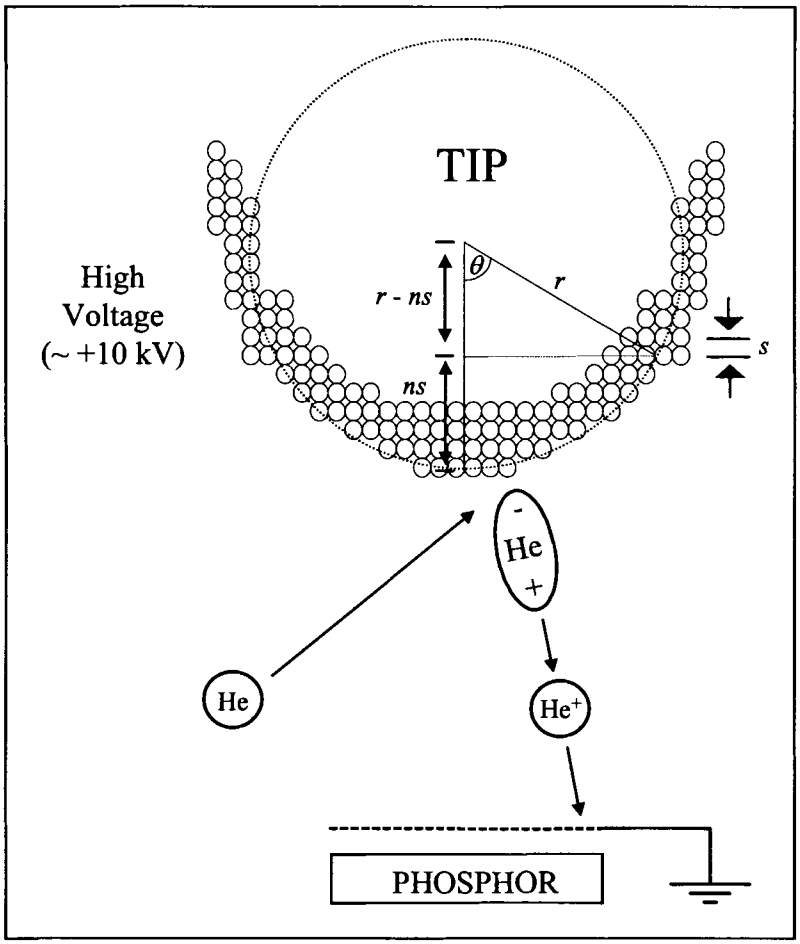

Figure 4.1: Field ionization process.

which is about one million times. This magnification is sufficient to resolve atomic structure.

At the atomic scale, the contour of a tip apex consists of terraces and steps. Since the electric field is largest at step edges, atoms at steps appear as brighter regions in an FIM image (Figure 4.2b). Each atomic step forms a ring pattern in the FIM image corresponding to a crystallographic pole for a plane in the crystal. The concentric ring patterns can be used to map out the crystallographic structure of the tip surface. An FIM image is most closely represented by a crystal stereographic projection [1].

4.2 Determining Tip Radius of Curvature

Determining the tip local radius of curvature, r, from a pole in a FIM image is a straightforward procedure if the crystal structure of the material is known (Figure 4.1). To calculate r, first the pole, (hkl), closest to the tip apex is identified; typically this pole is in the center of the FIM image. Next, the number of concentric rings, n, from that pole to the next major pole, $(h'k'l')$, on the FIM image is counted. The angle, θ, is simply

$$\theta = \cos^{-1} \frac{hh'+kk'+ll'}{\sqrt{h^2 + k^2 + l^2}\sqrt{h'^2+k'^2+l'^2}}. \tag{4.1}$$

From simple geometry, r is given by

$$r = \frac{ns}{1 - \cos\theta}, \tag{4.2}$$

where s is the crystal lattice plane spacing. As an example, Figure 4.2c shows $n = 10$ concentric rings from the (011) pole to the (112) pole. The angle between the (011) and (112) poles is $\theta = 30°$ and the lattice spacing for the (011) planes of tungsten is $s = 0.223$ nm. Thus $r = 16.6$ nm for the local radius of curvature with respect to the (011) pole.

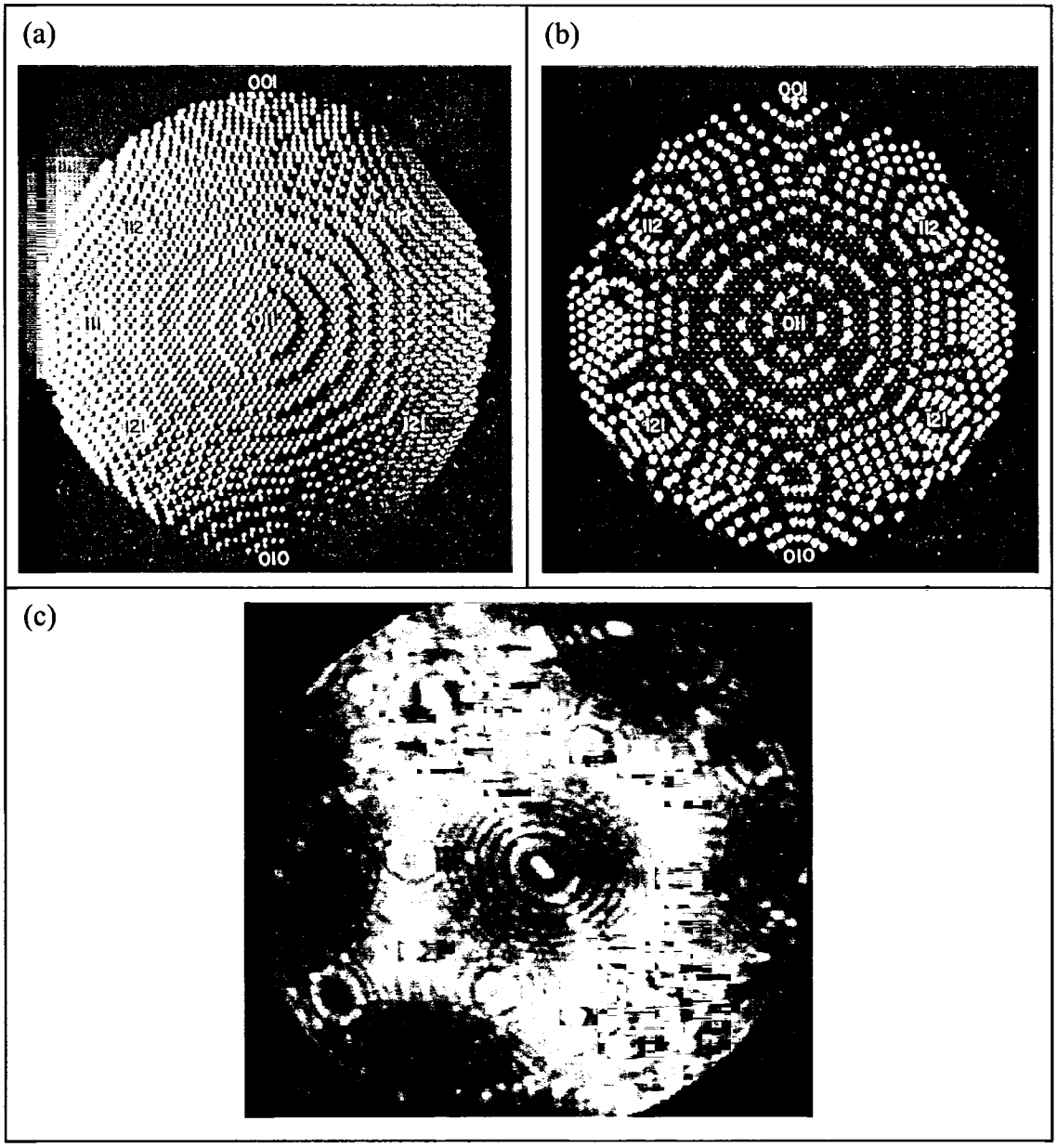

Figure 4.2: FIM image representation. (a) Ball model of a (011) oriented tungsten tip. (b) Ball model with most protruding and second next protruding atoms marked with fluorescent paint, illuminated with UV light (from reference [2]). (c) (011) centered FIM image of tungsten at room temperature acquired in our laboratory.

4.3 Field Evaporation

As the voltage on the tip is increased beyond the imaging voltage range, one reaches an electric field value at the tip large enough that atoms on the tip become ionized and are repelled. This process is known as field evaporation if the repelled atoms are tip atoms, or field desorption if the repelled atoms are atoms adsorbed on the tip. Since field evaporation occurs first at locations of highest electric fields (hence the sharpest regions of the tip) it naturally shapes the tip into a smooth surface. In our experiment, we routinely used field desorption to clean our tips of contaminants and field evaporation to shape our tips to the desired radius of curvature.

4.4 Field Corrosion

A nice property in using helium as an imaging gas in FIM is its high ionization potential of 24.6 eV; this is the highest ionization potential of any element. If while imaging a tip with helium, any foreign atom that gets close to the tip apex will be ionized and repelled. This protects the cleanliness of the tip surface. If the FIM chamber is contaminated or has an unusually high pressure, contaminants can start to react with the tip shank just outside the apex region. This can cause the tip shape to slowly change and allow the contaminated region to slowly creep toward the apex. This effect is known as field corrosion [3]. We observed that this type of tip deterioration did not occur as long as the pressure remained below $1x10^{-9}$ torr.

4.5 FIM Instrumentation

The FIM used for this work is composed of mainly three components: the tip, the microchannel plate (MCP), and the FIM ring, which are housed in a UHV chamber (Figure 4.3). The imaging gas used in our work was helium.

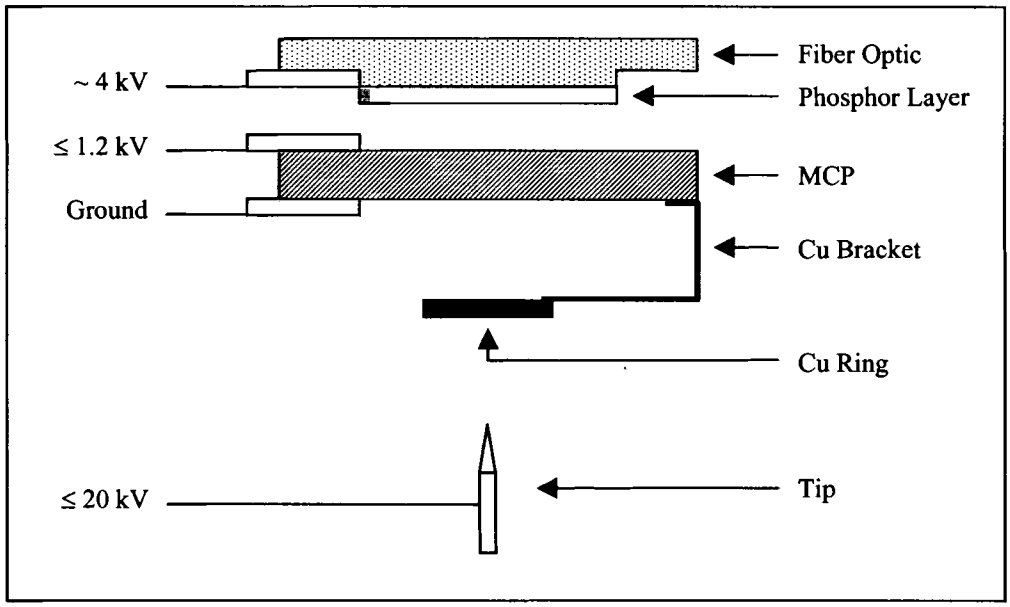

Figure 4.3: FIM instrument schematic.

4.5.1 Tip

Tips for FIM were prepared using a two step electropolishing procedure [4], which includes a rough electropolishing step followed by a zone electropolishing step. The tips are held in a force sensor as described in Section 3.2.2. Voltage is applied to the tip by use of a FUG model HCN35M-20000 high voltage power supply. The power supply is capable of 0 – 20 kV and 1.5 mA using either positive or negative polarity.

4.5.1.1 Rough Electropolishing

The first step of electropolishing the tip is the rough electropolishing using the setup shown in Figure 4.4a. The tips were made from 0.0197″ diameter tungsten wire. The wire was cut using a pair of dull side cutters, which has been found to minimize the dislocation density near the location of the cut. Next, the cut tungsten wire was partially suspended in a beaker of 2 N NaOH solution. One electrode of the 10 V AC power

supply was connected to the end of the tip, and the other electrode was connected to a 0.25″ diameter graphite rod placed in the solution. The tip was visually oriented vertically with about 0.30″ of the end of the tip submerged in the solution, and then the 10 V AC voltage was applied. At the tip-liquid interface, a small meniscus was present that slowly changed the shape of the wire at the interface to a tapered end, while the remaining wire in the solution was completely etched into the solution. The rough electropolishing procedure took about 5.5 minutes to complete and yielded a tip with a few hundred nanometer radius of curvature.

4.5.1.2 Zone Electropolishing

The subsequent zone electropolishing procedure (Figure 4.4b) was used to obtain a sharper tip. A small loop of gold wire was submerged in a solution of ~ 1 N NaOH and then pulled out to leave a small amount of fluid suspended in the loop of wire. Gold wire was chosen so that it would not react with NaOH during the electropolishing process. The loop of wire was then controlled by a micromanipulator that moved in one dimension in order to control tip shape. The tip was mounted in a 600x microscope with a long focal length. An AC voltage of 3 - 10 V was applied between the tip and the loop. The tip was inserted into the loop while being observed through the eyepiece of the microscope. A micro-switch was used to control when the voltage would actually be applied. When looking through the eyepiece, a voltage was applied to the loop via a microswitch and the micromanipulator was moved to create a controlled tip shape. This procedure routinely yielded a tip radius of curvature of ~ 3 nm. The radius of curvature was determined using FIM as described in Section 4.2.

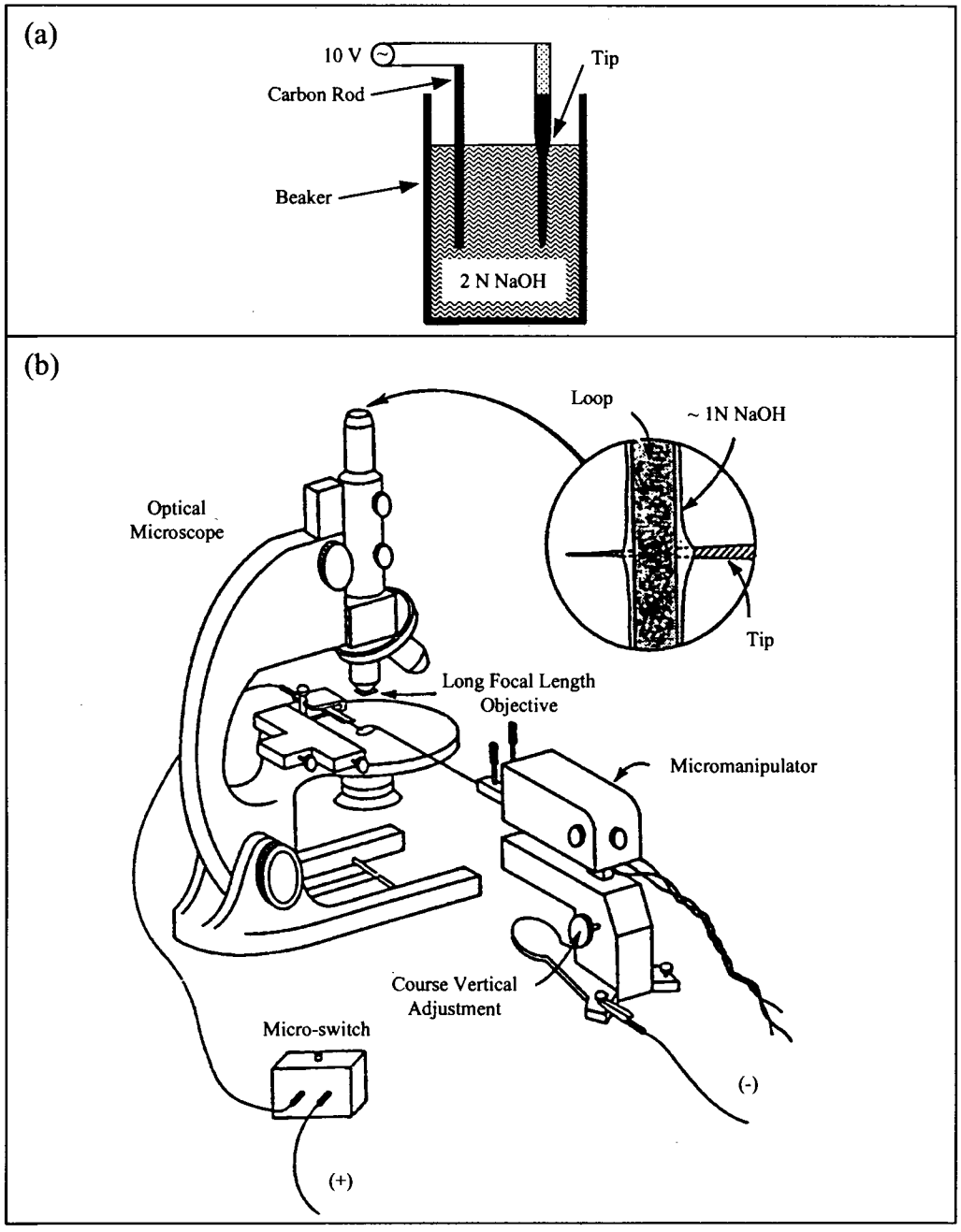

Figure 4.4: Tip fabrication. (a) Rough electropolishing. (b) Zone electropolishing (from reference [4]).

4.5.2 Microchannel Plate (MCP)

A MCP was used in front of the phosphorescent target to amplify the FIM image intensity. Our specific MCP is an Advanced Performance Long-Life™ Microchannel Plate [5] assembly model CEMA 6040PS manufactured by Burle Industries, Inc. The MCP assembly includes both the MCP and a fiber optic section.

The MCP is a leaded glass plate perforated with 10 μm diameter cylindrical channels (Figure 4.5). The insides of the channels are coated with a silicon dioxide secondary electron emissive layer on top of a semi-conductive layer. The front and back of the MCP are coated with a thin metal electrode. The front electrode was grounded and the back electrode was biased to + 1.2 kV with respect to ground using a Bertan model 602B-50P high voltage power supply.

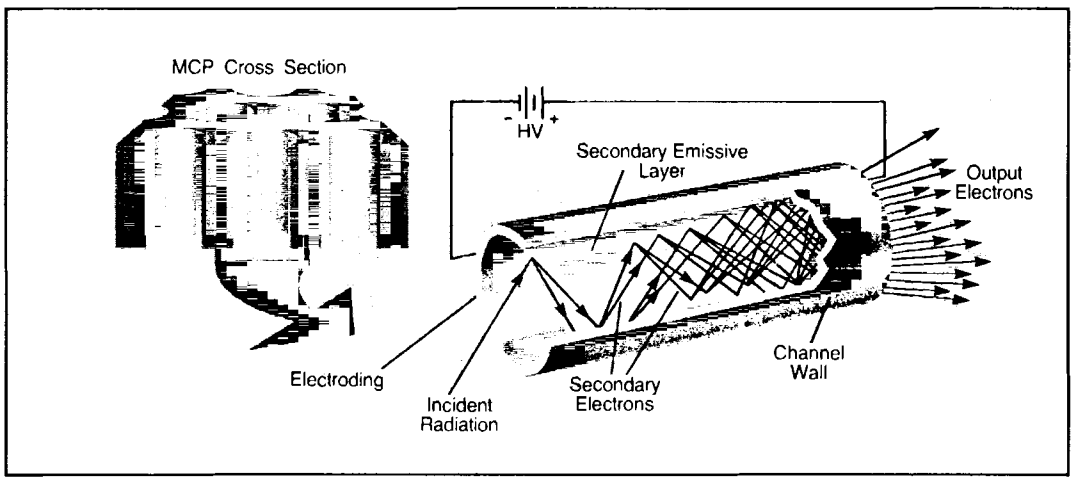

Figure 4.5: Multichannel plate (MCP) (from reference [6]).

The fiber optic section has a layer of phosphor deposited on top of it. Between the phosphor layer and the fiber optic is an optically transparent conductive layer. This conductive layer was biased to + 4 kV with respect to ground using another Bertan model 602B-50P high voltage power supply. All three of the high voltage power supplies for

the FIM are connected to the UHV system via super high voltage (SHV) connectors mounted on a flange.

A FIM image is formed by ions first entering into the channel openings on the front of the MCP. These ions collide with the walls of the channels and cause the release of more electrons. All these electrons travel toward the back of the channel due to the bias on the channel. As they travel down the tube the electrons have more collisions with the walls and in turn release even more electrons. The multiplication factor at the output end of the channel is about 10^4. The exiting electrons at the back of the MCP are accelerated toward the phosphor where they collide to produce light. The light is then channeled through the fiber optic assembly to minimize the amount of light scatter.

4.5.3 FIM Ring

As a tip is positioned further away from the MCP, the magnification of the FIM image is increased. However, the tradeoff is that more voltage is needed to reach the same field for field ionization. In order to keep the voltage at a reasonable magnitude and get proper magnification at the same time, a metal ring was constructed and placed in front of the tip (see Figure 4.3). The ring has the same potential as the front of the MCP and allows the ions to travel a longer radial path before colliding with the MCP, thus leading to higher magnification. The distance between the tip and the ring remains small enough so that a lower voltage can be used for field ionization.

4.6 References for Chapter 4

1. Müller, E.W. and Tsong, T.T., Field Ion Microscopy Principles and Applications, (American Elsevier Publishing Co., Inc., New York, 1969).

2 . Müller, E.W., Advances in Electronics and Electron Physics Vol. XIII, (Academic Press, New York, 1960), p. 144.

3 . Miller, M.K. and Smith, G.D.W., Atom Probe Microanalysis: Principles and Applications to Materials Problems, (Materials Research Society, Pennsylvania, 1989), p. 20.

4 . Melmed, A.J., Journal of Vacuum Science Technology B 9, 601 (1991).

5 . Long-Life™ Microchannel Plate is a trademark of Burle Industries, Inc.

6 . From a data sheet HOT Microchannel® Plates from BURLE ELECTRO-OPTICS, INC. Used with permission of BURLE TECHNOLOGIES, INC.

Chapter 5

INSTRUMENT CALIBRATIONS AND EXPERIMENTAL PROCEDURES

Experimental results presented in Chapter 6 involve measurements of force in the nano-Newton to micro-Newton range and sample/tip displacements in the 10 - 50 nm range. Accurate measurements of these small quantities required careful consideration of sources of error for all the experimental parameters. This chapter discusses in detail the calibration procedures and experimental protocols that were used to obtain meaningful and reproducible data.

5.1 Calibration Procedures

Three different calibration procedures were performed on a regular basis in order to assure precision in our experiments. The most frequent calibration, one that needed to be done for every experiment, involved the interferometer. Since the interferometer signal is sinusoidal and the tip displacements in our indentation experiments were small, the interferometer signal needed to be normalized as discussed in Section 5.4. The next most frequent calibration was for the force sensor in order to determine the force constant and response characteristics. The least frequent calibration was to determine the extent of hysteresis and motion displacement for the piezoelectric scanning tube (PST).

5.1.1 PST Calibration

There were two different types of calibration performed for the PST, one for the z direction and one for the x and y directions. To calibrate the PST for the z direction, the tip holder was taken out of a force sensor. This left just the force sensor body (FSB) which has the polished pads on the bottom. The FSB was slid into the force sensor

mount on the AFM head as usual. Instead of attaching a sample to the end of the PST, a stainless steel cylinder with a mirror-polished end was stuck on the end of the PST. As the PST was moved downward, the cylinder was lowered through the inside of the FSB until its polished surface was at the same z-height as the polished pads of the FSB. One of the interferometer laser beams reflected off the mirror-polished surface of the cylinder while the other laser beam reflected off a polished pad on the FSB. The six computer macros that were written to perform indentation experiments had different PST extensions and indentation rates. The three different PST extensions were approximately 6 nm, 9 nm, and 19 nm. These are only nominal values since the calibrations changed over time. For each PST extension there were two different macros, one which corresponded to an indentation time of about 380 ms ("fast" indent) and one where the indentation time was about 2 s ("slow" indent). The fast indentations for the 6 nm, 9 nm, and 19 nm PST extensions had an indentation rate of 16 nm/s, 24 nm/s, and 50 nm/s respectively. The calibration procedure consisted of executing the six different macros using the cylinder with the mirror-polished end and saving the interferometer data. This yielded the PST voltage signal calibrated against the interferometer voltage signal, with the PST voltage signal in units of DAC voltage.

The interferometer signal output is sinusoidal, so to determine the z position of the PST requires taking the arcsine of the interferometer voltage signal. The interferometer voltage signal received by the computer was corrected for any offset voltage; this offset was determined by measuring the interferometer signal with an oscilloscope. Then, the maximum and minimum interferometer voltages were measured by moving the cylinder so that the interferometer signal traversed at least one full fringe.

These values served to normalize the interferometer signal output. In the actual indentation experiments, the extensions are so small that they never cause the interferometer to go through a maximum and a minimum signal. Therefore we needed to determine these maximum and minimum signals as a reference prior to an indentation. Once the signal is normalized, the interferometer output, I, becomes:

$$I = \sin\left[\frac{2\pi}{(\lambda/2)} z\right], \tag{5.1}$$

where, $\lambda = 632.8$ nm, is the wavelength of the laser and, z, is the position of the mirror-polished surface of the cylinder. We determined the z position of the PST by solving Eq. 5.1 for z:

$$z = \frac{\lambda}{4\pi} \sin^{-1} I. \tag{5.2}$$

During the approach, the Soleil-Babinet compensator was adjusted so that the interferometer signal was close to zero such that when the tip holder moves, the interferometer signal is at the most sensitive location on the sinusoidal interferometer curve.

The absolute position of the PST was determined by subtracting a reference baseline established from a best fit line through the interferometer signal during static tunneling prior to the start of an indentation experiment. The PST displacement plotted against the DAC voltage applied to the PST was fitted with a third degree polynomial as shown in Figure 5.1. This polynomial fit was used in calculating the penetration depth from the nanoindentation data.

Figure 5.1a shows hysteresis with a maximum difference in displacement of ~ 2 nm. Only the fast and slow 19 nm PST displacements showed any measurable hysteresis.

So for these curves we separately fitted the insertion portion and the withdrawal portion. No consideration was taken to match the two different curve fits at the turnaround point. The discrepancy between the two different curves at the turnaround point was never more than 0.5 nm. Since there was no measurable hysteresis in the 6 nm and the 9 nm PST displacements (see Figure 5.1b), these curves were only fitted with one curve that represented both the insertion portion and the withdrawal portion of the indentation. This calibration was carried out on a monthly basis and the calibration that was used for a given experiment was that which had the closest date.

The calibration for x and y directions of the PST was much easier. We performed this calibration by scanning, in STM mode, a gold coated grid with a 1 μm periodicity in both directions. A typical calibration value was 37.5 nm/V. Lateral scanning hysteresis was ignored in all of our experiments since the maximum scan size used was 400 nm x 400 nm.

5.1.2 Force Sensor Calibration

All the nanoindentation experiments reported in this thesis were performed with one force sensor. This force sensor was calibrated by determining the slope of a force vs. displacement curve using a Vitrodyne® [1] V1000 Universal micromechanical tester. A lead screw with 1 μm displacement precision was pushed against the force sensor and the force was measured with a strain gauge load cell. Using this method the spring constant, k, for the force sensor was determined to be 442 N/m. One problem with this method of determining k is that the micromechanical tester's smallest displacement is only 1 μm

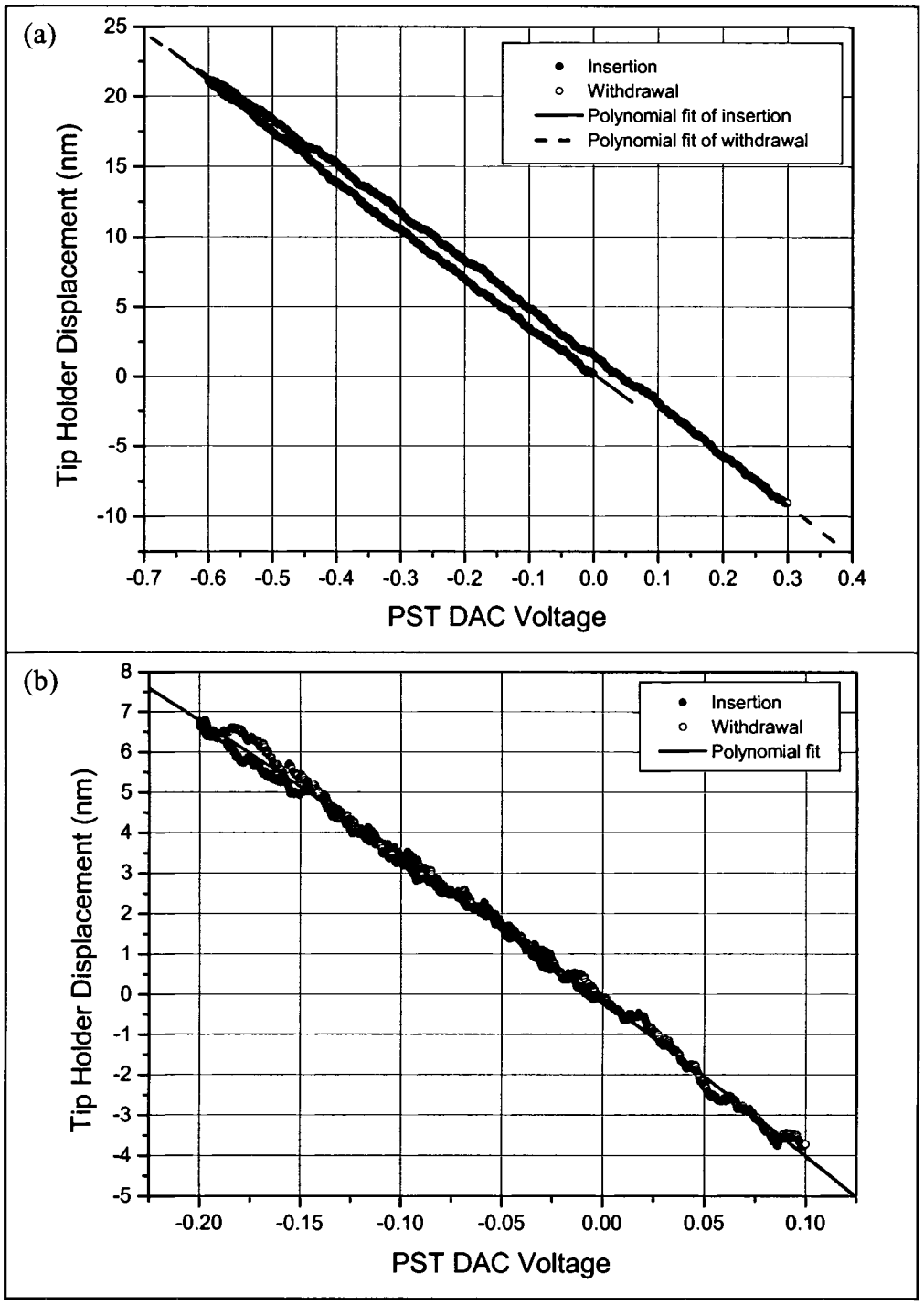

Figure 5.1: PST calibration curves. (a) Calibration curve for a 19 nm PST displacement. (b) Calibration curve for a 6 nm PST displacement.

and the load cell precision is ~ 1 mN. However, the largest force sensor displacement that we experience during our indentation experiments is < 14 nm. In using k = 442 N/m, we assume that k is constant down to the nanometer region with the same value. If the force vs. displacement curve is not truly linear, then k determined in this way could be incorrect. We therefore modeled the mechanical response of our force sensor to determine the appropriateness of the linear force versus displacement relationship.

A theoretical expression was found that related the total force exerted by the force sensor, F, as a function of tip holder displacement, z, for our force sensor geometry. In this model we will assume the tip holder and tip have no mass. We are interested in determining the spring constant which is the slope of the force curve versus displacement, and the mass would not affect this spring constant value. Referring to Figure 5.2b, the force, f, that one of the four wires applies to the tip holder is analyzed. The tip holder is displaced a distance z and causes the wire to make an angle θ with the plane of the FSB. The force, f, is related to the tension, T, in the wire by:

$$f = 2T \sin \theta, \tag{5.3}$$

the factor of 2 is due to the wire being displaced at its midpoint. T is determined from the stress-strain relationship, $T/A = E\varepsilon$, where A is the cross sectional area of the wire, E is the elastic modulus of the wire, and ε is the strain on the wire which is given by:

$$\varepsilon = \frac{2L + 2r_3 + \frac{\pi}{2} r_1 - R_0}{R_0}, \tag{5.4}$$

where R_0 is the length of the wire between points A and B (which is the location of epoxy that holds the wire) when the force sensor is unloaded. T is therefore:

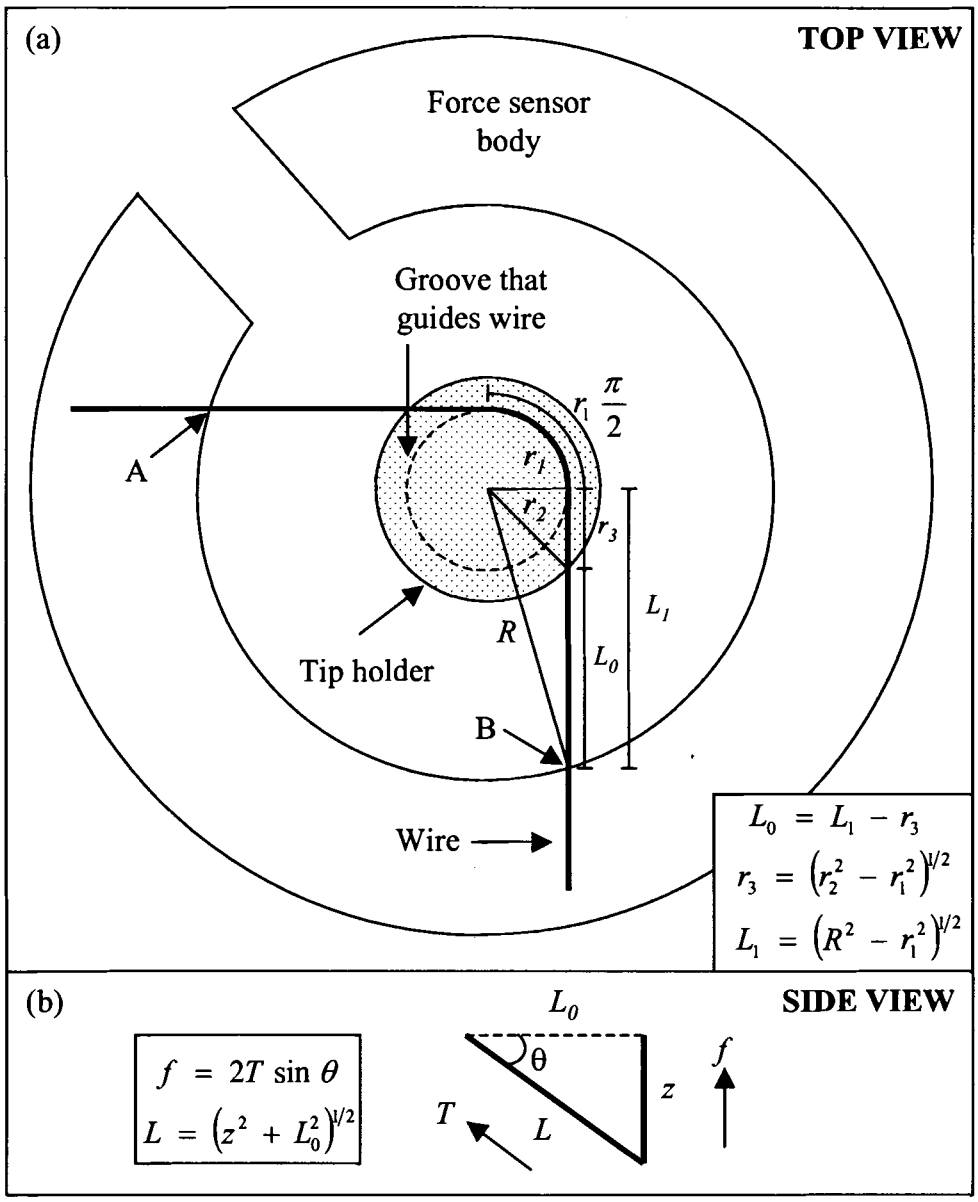

Figure 5.2: Force sensor geometry. (a) Top view of the force sensor. Only one out of the four wires is shown for clarity. (b) Side view schematic of the force sensor showing its displacement in the vertical direction.

$$T = AE\left(\frac{2L + 2r_3 + \frac{\pi}{2}r_1 - R_0}{R_0}\right). \tag{5.5}$$

Substituting Eq. 5.5 into Eq. 5.3, and using the geometrical argument that $\sin\theta = z/L$, we get:

$$f = 2AE\,\frac{z}{L}\left(\frac{2L + 2r_3 + \frac{\pi}{2}r_1 - R_0}{R_0}\right). \tag{5.6}$$

Given the geometrical relation $L = \left(z^2 + L_0^2\right)^{1/2}$, and that there are four wires that make up the force sensor, the total force, $F(z)$, that the force sensor pushes on the tip holder with is given by:

$$F(z) = 4f = \frac{8AEz}{R_0\left(z^2 + L_0^2\right)^{1/2}}\left[2\left(z^2 + L_0^2\right)^{1/2} + 2r_3 + \frac{\pi}{2}r_1 - R_0\right]. \tag{5.7}$$

The known quantities are R = 5.08 mm, r_1 = 1.02 mm, r_2 = 1.27 mm, $A = 8.11\text{x}10^{-9}$ m^2, E = 160 GPa and T_0 = 0.178 N so we must find expressions for L_0, r_3 and R_0.

R_0 can be determined by the tension, T_0, that is originally in the wire when the force sensor is unloaded. They are related through the stress strain relationship:

$$\frac{T_0}{A} = E\left(\frac{2L_1 + \frac{\pi}{2}r_1 - R_0}{R_0}\right). \tag{5.8}$$

Solving Eq. 5.8 for R_0 yields:

$$R_0 = AE\left(\frac{2L_1 + \frac{\pi}{2}r_1}{AE + T_0}\right). \tag{5.9}$$

The unknown quantities L_1, L_0, and r_3 can be determined in terms of the known quantities through geometrical considerations shown in Figure 5.2.

We recently developed a new technique for making force sensors (as discussed in Section 3.2.2) where we can accurately build a force sensor with a specific k value. The smaller k is, the better the signal to noise ratio is in our interferometer. The easiest way to make k smaller is to use a smaller tension in the wire when building the force sensor, but if the tension becomes too small the tip holder will not be held very rigidly and it becomes susceptible to rotation when taking tips in and out. This rotation destroys the interferometer alignment on the back of the tip holder. A spring constant of 338 N/m was estimated to be the optimum value when considering the sensitivity versus robustness trade-off. The value of 442 N/m for the force sensor used in experiments discussed in Chapter 6 is close to this optimum value.

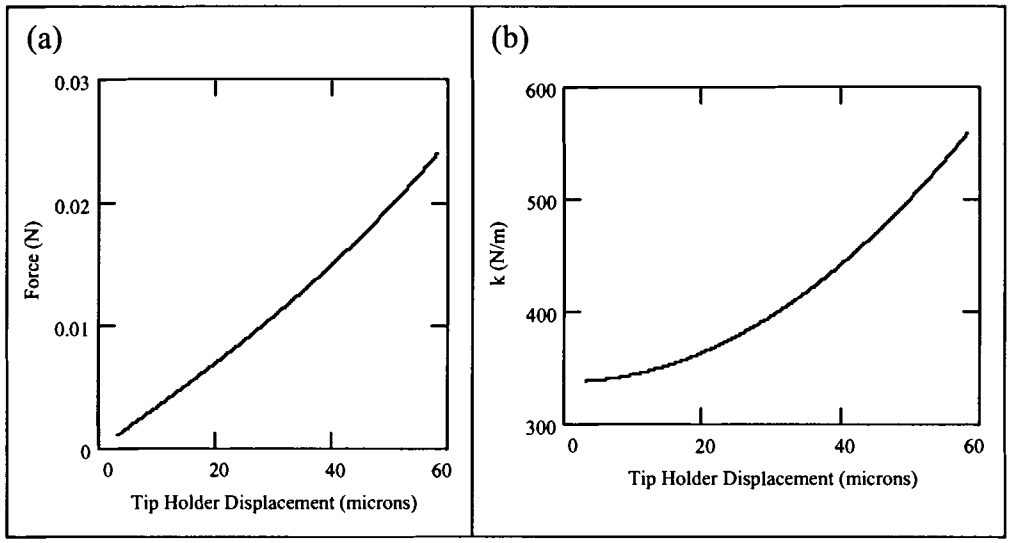

Figure 5.3: Theoretical predictions for force sensor. (a) Force vs. tip holder displacement for k = 338 N/m in the nanometer region. (b) Corresponding k vs. tip holder displacement curve.

Using Eq. 5.7, the force vs. displacement curve for a force sensor with k = 338 N/m is plotted in Figure 5.3a. Note that the curve is non-linear. $k(z)$ can be determined by taking the derivative of Eq. 5.7 with respect to z; k vs. z for a force sensor that has a value k = 338 N/m in the nanometer region is plotted in Figure 5.3b. The displacement range accessible in the micromechanical tester calibration method is 0 – 60 μm. In the $k(z)$ plot covering this range (Figure 5.3a) we find that k varies between 338 N/m and 560 N/m, with a midway value of 399 N/m. This midway value is approximately what is determined by a simple linear fit. An experimentally measured $F(z)$ curve obtained using the micromechanical tester method is shown in Figure 5.4. The slope is 412 ± 2 N/m which is only 3 % error from the expected 399 N/m.

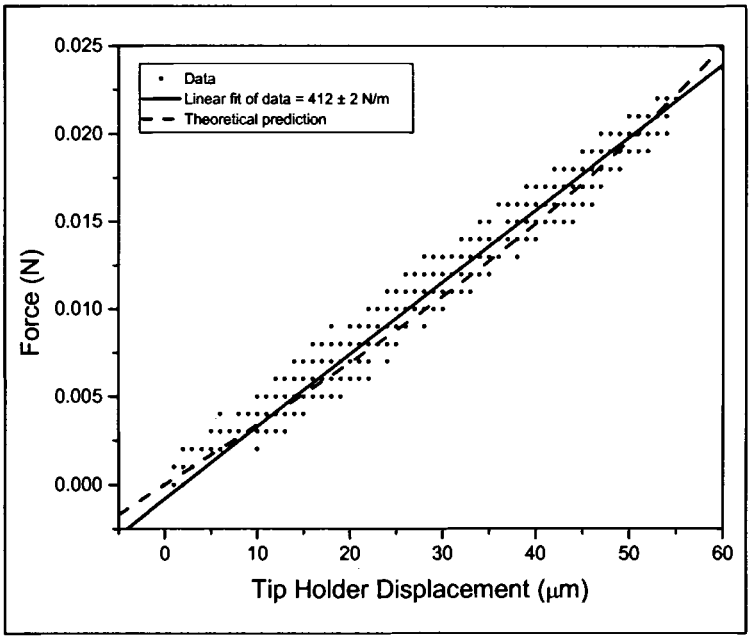

Figure 5.4: Force vs. tip holder displacement curve for a force sensor. The theoretical k = 338 N/m for the nanometer region. Linear fit k = 412 N/m, measured using a Vitrodyne® V1000 Universal micromechanical tester.

Based on the model for our force sensor, we believe that the value of 442 N/m for the force sensor used in our indentation experiments is actually smaller. However, the actual value is difficult to determine since the tensions were not the same on all four wires in this sensor. Also the tip was changed multiple times within that force sensor. We found with the new force sensors that the force constant can be perturbed by as much as a factor of two or three when tips are changed. Based on numerous measurements on all of our force sensors, we estimate that the true spring constant of the force sensor used in our indentation experiments is between 338 N/m $< k <$ 442 N/m leading to an error in actual force of less than 30%.

5.2 Preparation of the Au (110) Surface

Immediately before the Au (110) sample was placed in the chamber it was flame annealed using a propane torch to approximately 600° C. This treatment has been reported to eliminate hydrocarbon contamination and produce a clean surface [2,3]. The sample was inserted into vacuum via the load lock and transferred to the manipulator in the sample characterization chamber. The base pressure in our UHV system was ~ 2.0×10^{-10} torr. The surface cleanliness of the sample was checked using Auger electron spectroscopy (AES); only a small carbon signal was detected in addition to the gold peaks. To remove the carbon the sample was sputtered for about 10 minutes using a 2 kV ion gun in an argon atmosphere of 5.0×10^{-5} torr. The argon was pumped out and then the sample was heated for ~ 5 minutes at 700° C using an electron beam heater to anneal out the ion beam damage. A sample prepared in this way remained free of contamination in UHV for about 2 days, after which carbon build-up was noticed and the cleaning

treatment repeated. Using the transfer arm, the clean Au (110) sample was docked onto the end of the PST in the experimental chamber.

5.3 Preparation of the Tungsten Tip

Prior to each indentation experiment, an FIM image was taken of the tip. To accomplish this, the slide was adjusted so that the MCP was above the tip. Next, the ion pump was turned off, the chamber was valved off from the turbo pump and filled with helium to a pressure of $\sim 9 \times 10^{-5}$ torr. The appropriate voltages were turned up on the MCP until an image was noticed on the phosphor screen (PS). The tip was field evaporated until a clean tungsten FIM image was apparent. A CCD camera was aligned above the PS and not moved for the rest of the experiment. The location of the slide that held the MCP was also noted so that the MCP could be returned back to the same position after the indentation experiment was complete. An FIM image was captured using the CCD camera to retain an accurate measure of the tip radius. The radius of curvature of the tungsten tip was determined by counting the number of rings from the (110) pole to the (121) pole as discussed in Section 4.2. Tip radii ranged from 13.6 nm to 21.6 nm.

5.4 Tip-Sample Approach

After preparing and imaging the tip, the helium was pumped away and the mechanical and turbo pumps were disconnected from the chamber to eliminate mechanical vibrations; the chamber was still pumped using an ion pump. Using the slide mechanism, the gold sample was positioned above the tungsten tip. Then the sample was positioned close to the tip, as sighted by eye, by manually controlling the Inchworm® [4]. Next the interferometer was mechanically perturbed by hand to cause the interferometer

signal to vary through an entire fringe. The maximum and minimum values of this fringe were noted so as to normalize the interferometer signal, much the same way as for the PST calibration (Section 5.1.1). The stability of the interferometer was found to be quite vulnerable to noise and air currents in the room. A styrofoam box was used to completely enclose the chamber to minimize these effects. During the approach, the Soleil-Babinet compensator was adjusted so that the interferometer signal was close to zero as mentioned in Section 5.1.1.

The approach mode was started under computer control. Eventually the tip went into tunneling contact and the computer system went into tunneling feedback mode. Prior to the start of an indentation, the tip was translated laterally by ~ 645 nm to a different location on the gold surface. This procedure was used in case there was accidental surface contact and deformation during the initial approach.

5.5 Contact and Indentation

The tunneling current and the interferometer signal often exhibited noise fluctuations while the tip was in tunneling contact. When the noise was judged to be minimal the indentation was performed using the selected macro. The nanoindentation experiments consisted of sending a programmed voltage sequence to the PST in order to cause an indentation and withdrawal of the tip with respect to the gold surface. The three sets of data that were simultaneously collected are: i) the voltage signal output from the current to voltage (I-V) converter that measures the current between tip and sample, ii) the voltage signal from the photodiode output of the interferometer signal which tracks the motion of the tip in the tip holder and iii) the voltage being applied to the PST. Figure 5.5 shows a representative set of raw data from one of the indentation

experiments. The voltage signal from the I-V converter, through a calibration procedure, is plotted in units of current (amps), and the voltage signal from the interferometer has been converted to show tip displacement (see section 5.1.1 and Eq. 5.2 for conversion procedure). We assume that there is no elastic or plastic deformation of the tip, which means that the tip displacement and the tip holder displacement are the same.

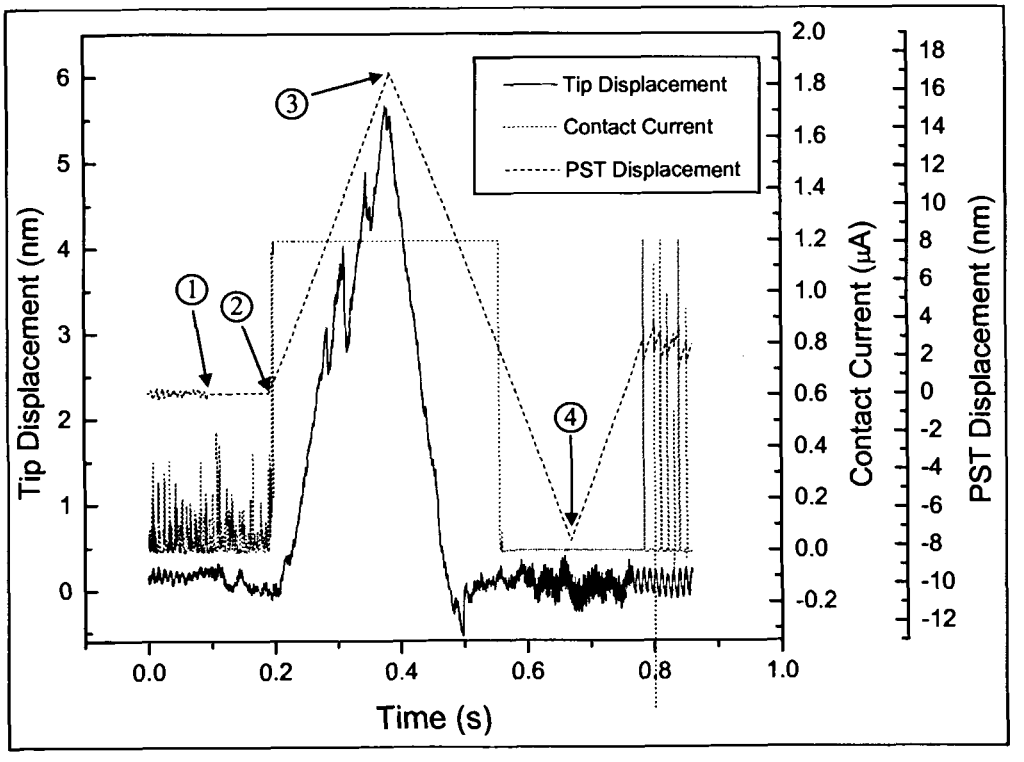

Figure 5.5: A representative set of raw data. Measurement acquired during a W/Au (110) indentation experiment.

The controlled parameter during indentation was the PST motion. Up to position 1 (see Figure 5.5), the system feedback was on and the tip was in tunneling mode with the surface. Between positions 1 and 2 the feedback was shut off for a period of 95 μs for the fast experiments (99 ms for the slow experiments) while the programmed PST sequence was established. Immediately after position 2, the tip comes into contact with

the sample and the contact current saturates to a value of 1.2 μA (limited by the I-V converter). Between positions 2 and 3, the PST was advanced at a constant rate to the maximum indentation depth before being retracted (between positions 3 and 4) at the same constant rate beyond its original starting location. After position 4, the PST was advanced to its original starting position in tunneling current.

There was often random drift in the interferometer signal that occurred over a time interval on the order of seconds. We carefully waited and tried to do a quick indent in between these fluctuations. However, sometimes these fluctuations occurred during an experiment and caused a baseline drift in the interferometer data. This problem would render that data set useless as shown by the tip displacement graph in Figure 5.6a. The drift is seen quite dramatically in the corresponding force vs. penetration depth graph in Figure 5.6b. We were unable to locate the exact source of this drift, but it did appear to be related to the rigidity of the interferometer and how it was attached to the chamber. Because of these noise fluctuations, most experiments were performed at the fast rate (380 μs between points 1 and 4 in Figure 5.5). The high frequency noise in the interferometer signal (~ 300 Hz) yielded a typical uncertainty of ~ ± 1.7 Å in tip displacement, and hence an uncertainty of ± 75 nN in the force.

5.6 Post-Indentation Analysis

Immediately after the indentation, an STM scan was performed to image the size and shape of the deformation volume where the indentation had occurred. The scan size was 400 nm x 400 nm at a scan rate of 0.5 Hz. Next, the Inchworm® was retracted, the styrofoam box was removed, and the pumps were reconnected and started. The slide was

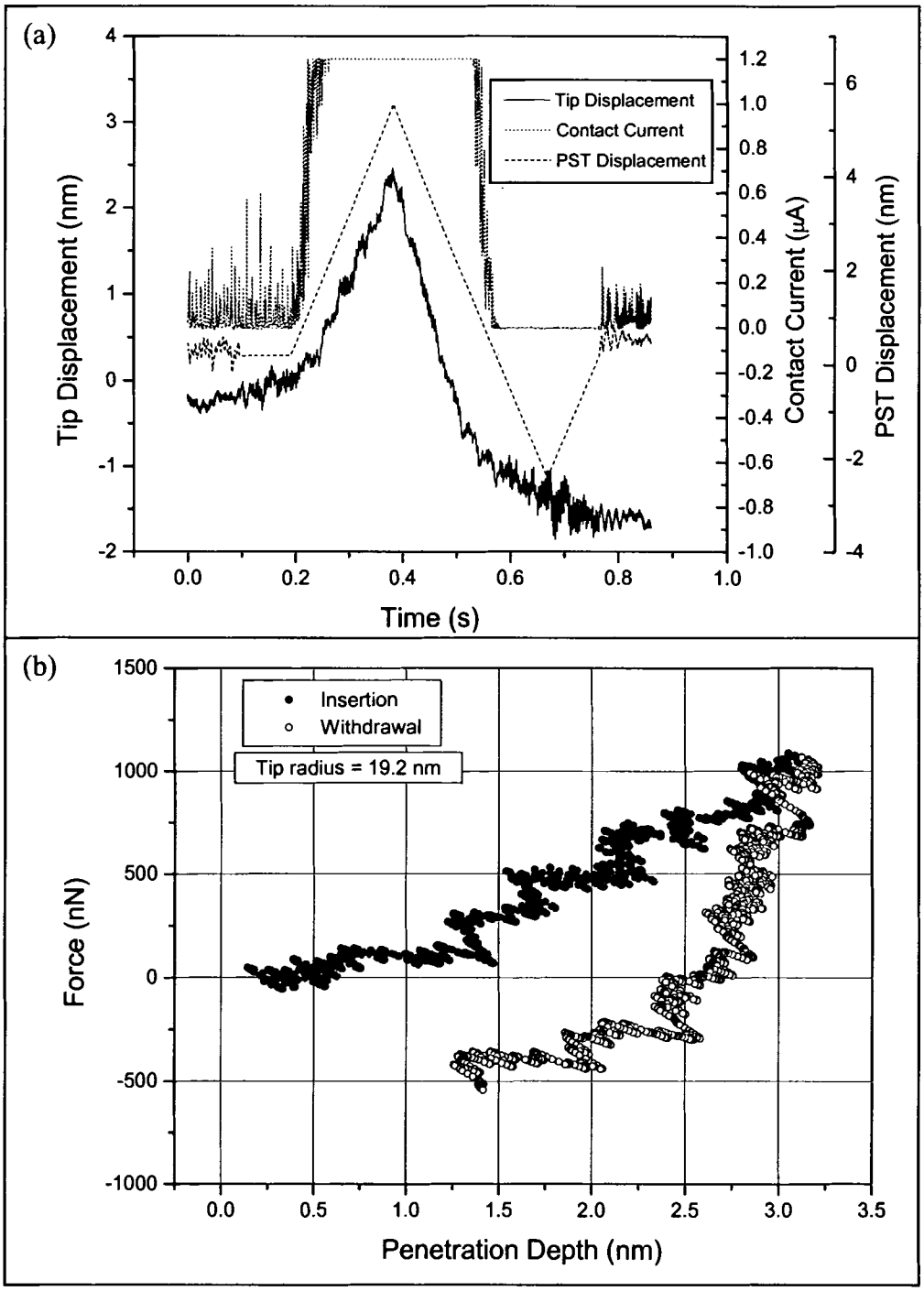

Figure 5.6: Interferometer noise. (a) Example of baseline drift in interferometer data. (b) Corresponding force vs. penetration depth data showing unphysical characteristics.

moved such that the MCP returned to the FIM position. Helium was introduced into the chamber to a pressure of ~ $9x10^{-5}$ T and the voltages on the MCP were raised. Several different FIM images were captured as the voltage was increased. This allowed us to see how the tip was being altered by field evaporation as the voltage was increased.

The tip was now ready to be field evaporated to prepare it for another experiment. We typically field evaporated a few hundred volts past the prior imaging voltage causing three atomic layers of the (110) plane to evaporate. This procedure yielded a clean tip with essentially the same radius of curvature. Several indentation experiments could be performed before a measurable change in tip radius was observed.

5.7 Data Processing

Once the data were obtained they were plotted in several different forms (see Figure 5.7). The most physically intuitive is force vs. penetration depth. The force was determined by multiplying the tip holder displacement by the spring constant of our force sensor (k = 442 N/m). The tip holder displacement was determined using Eq. 5.2 (see Section 5.1.1) using normalization of the maximum and minimum interferometer signals (see Section 5.4).

The penetration depth is determined by subtracting the tip holder displacement from the PST displacement (see Figure 5.7b). This represents the true deformation depth of the tip inside the sample during an indentation. The PST displacement is determined by applying the most recent calibration curve that corresponds to the macro used for the indentation. The force and penetration depth (see Figure 5.7d) were then both shifted according to the Hertzian model as discussed in Section 6.3.2. The contact current is

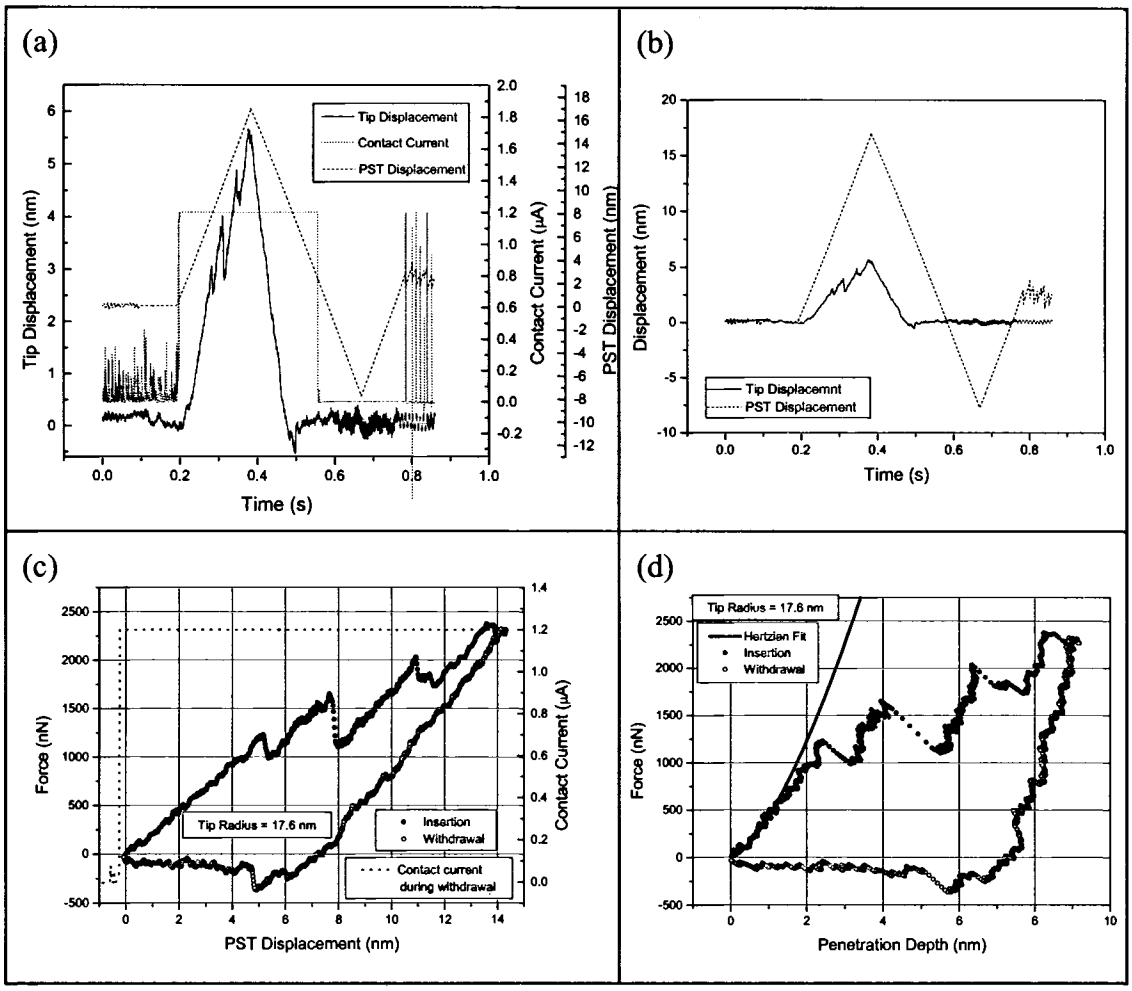

Figure 5.7: Various ways to display data for the same 19 nm PST displacement experiment. (a) Raw data. (b) Tip displacement and PST displacement vs. time. The penetration depth is determined by subtracting the tip displacement from the PST displacement. (c) Force vs. PST displacement. (d) Force vs. penetration depth.

displayed on a force vs. PST displacement graph (Figure 5.7c) rather than in a force vs. penetration depth graph so that it is easier to visualize the point of electrical contact.

5.8 References for Chapter 5

1. Vitrodyne® is a registered trademark of John Chatillon & Sons, Inc., Greensboro, N.C. 27409-9301.

2. Clavilier, J., Faure, R., Guinet, G., and Durand, R., Journal of Electroanalytical Chemistry 107, 205 (1980).

3. Corcoran, S.G., Colton, R.J., Lilleodden, E.T., and Gerberich, W.W., Physical Review B 55, R16057 (1997).

4. Inchworm® is a registered trademark of Burleigh Instruments, Inc., Burleigh Park, Fishers, NY 14453.

Chapter 6

NANODEFORMATION STUDIES AT TUNGSTEN/GOLD CONTACTS

6.1 Overview

This chapter presents the results and analysis of experiments performed by indenting a well-defined tungsten tip into a clean Au (110) single crystal sample at room temperature using the combined ultra high vacuum (UHV)/atomic force microscope (AFM)/scanning tunneling microscope (STM)/field ion microscope (FIM) system. Several other studies have focused on the W/Au system as discussed in Chapter 2, but they have covered a larger size regime compared to our experiment. A recent set of experiments by Grütter *et al.* [1,2,3,4] in the size regime comparable to ours is worth noting. They used FIM to shape and characterize a tungsten tip and used it to perform well-controlled indentation experiments. Their approach is similar to ours except that we perform our experiments at room temperature and use a larger contact size regime (~ 17 nm tip radii on average) compared to their experiments at 150 K using ≤ 3 nm tip radii.

In our work, several nanoindentation experiments were performed using a variety of tip radii and indentation depths. Table 6.1 lists the parameters for the 24 experiments that we carried out. The reliability and accuracy of some of the measurements were compromised due to problems of instability and drift in the interferometer as discussed in Section 5.5. However, reproducible results were acquired and they are analyzed in depth in the remaining part of this chapter.

The analysis of the experimental behavior can be broken down into several stages of the overall nanoindentation process: (a) tunneling contact (b) elastic contact (c)

yielding and plastic deformation (d) adhesion and break of contact. Each of these processes and supporting data will be discussed in turn.

6 nm PST Displacements	
Experiment #	Tip Radius (nm)
1	12.8
2	13.6
3	13.6
4	17.6
5	17.6
6	18.4
7	19.2
8	21.6
9	21.6
10	21.6

9 nm PST Displacements	
Experiment #	Tip Radius (nm)
11	12.8
12	12.8
13	14.4
14	16.8
15	21.6
16	21.6
17	21.6

19 nm PST Displacements	
Experiment #	Tip Radius (nm)
18	13.6
19	14.4*
20	15.2
21	17.6
22	17.6
23	17.6
24	17.6*

* These data sets were acquired at the ~ 2 s rate instead of the ~ 380 ms rate used for the other experiments.

Table 6.1: List of nanoindentation experiments covering a range of tip radii and piezoelectric scanner tube (PST) extensions.

6.2 Approach and Tunneling Contact

The first step in all of our experiments was to bring the well-defined tungsten tip into tunneling contact with the clean Au (110) surface. The tip voltage used for tunneling was +156 mV with the current set point at 2.2 nA corresponding to a resistance of 70.9 MΩ when in tunneling contact. These values are consistent with values used by other groups during STM on gold surfaces [1,5,6,7,8]. The usual tip to sample distance in an STM experiment is between 1 to 4 Å [9]. Due to exponential tunneling dependence, every 1 Å change in tip to sample displacement corresponds to one order of magnitude

change in the tunneling current [10]. An average noise level in the tunneling current from our apparatus caused the current to range between 0 - 600 nA, corresponding to < 2 Å of noise. The tunneling was often erratic and may be due to vibrations within the apparatus or instability of contaminants on the tip (see Section 6.6.1). The noise may have also been caused by tip instability resulting from adhered gold on the tungsten tip gathered during motion of the tip across the surface before the indent was performed. However, we have no conclusive proof for this effect. As the tip moved closer to the sample, the current saturated at 1.2 μA, due to limitations in our electronics. This saturation point is defined to be electrical contact (in contrast to tunneling contact) between the tip and sample. During an indentation experiment, the current remained saturated at this 1.2 μA level while there was physical contact. Occasionally there were short fluctuations during tunneling, before the indentation experiment, that exceeded the 1.2 μA limit. This meant that there was intermittent electrical contact between the tip and sample. This contact was short lived so it was assumed to be negligible in our analysis.

6.3 Physical Contact and Elastic Deformation

When considering the tip coming into physical contact, the location of the origin (i.e. zero force, zero displacement) must be defined so that all other measurements of the system can be quantified relative to this origin. This origin represents the point of "initial contact".

6.3.1 Problems Defining the Point of Initial Contact

In an idealized view of tip to surface contact, one would expect to observe a noise free transition in the interferometer and tunneling current signal as soon as the PST

begins to move from the tunneling position. By correlating these electrical and force signals, an origin could be defined with some precision.

Unfortunately, these criteria were never met simultaneously in our experiment for a variety of different reasons. Sometimes the contact current would exhibit a very noisy transition as shown in Figure 6.1a; in this particular case the "noisy transition" occurs over about a 0.1 s period. The same behavior occurs during the withdrawal portion of the indent. This example is from a 6 nm PST displacement experiment. For the 19 nm PST displacement experiments this "noisy transition" was not as pronounced due to a faster rate of PST motion and a deeper indentation into the sample. In addition to this "noisy transition" during initial contact, the ~ 2 Å of tunneling noise (see Section 6.2) adds to the uncertainty in defining the origin.

Noise and drift in the interferometer signal also contributes to the uncertainty for the origin. Figure 6.1b illustrates an example of an experiment that contains a high frequency noise of ± 4 Å in the tip displacement, and a drift in the interferometer baseline over the course of the experiment.

In our experiments, the feedback was shut off for a short amount of time as shown in Figure 5.5 between positions 1 and 2 (see Section 5.5). While the feedback was off, there is the possibility that the tip may have drifted closer to or further away from the sample. Unfortunately, this was a limitation of our instrumentation. Two different types of experiments that would have provided useful information are: (1) be in tunneling, pull away from the surface, and then begin the indent as shown in Figure 6.1c or (2) indent

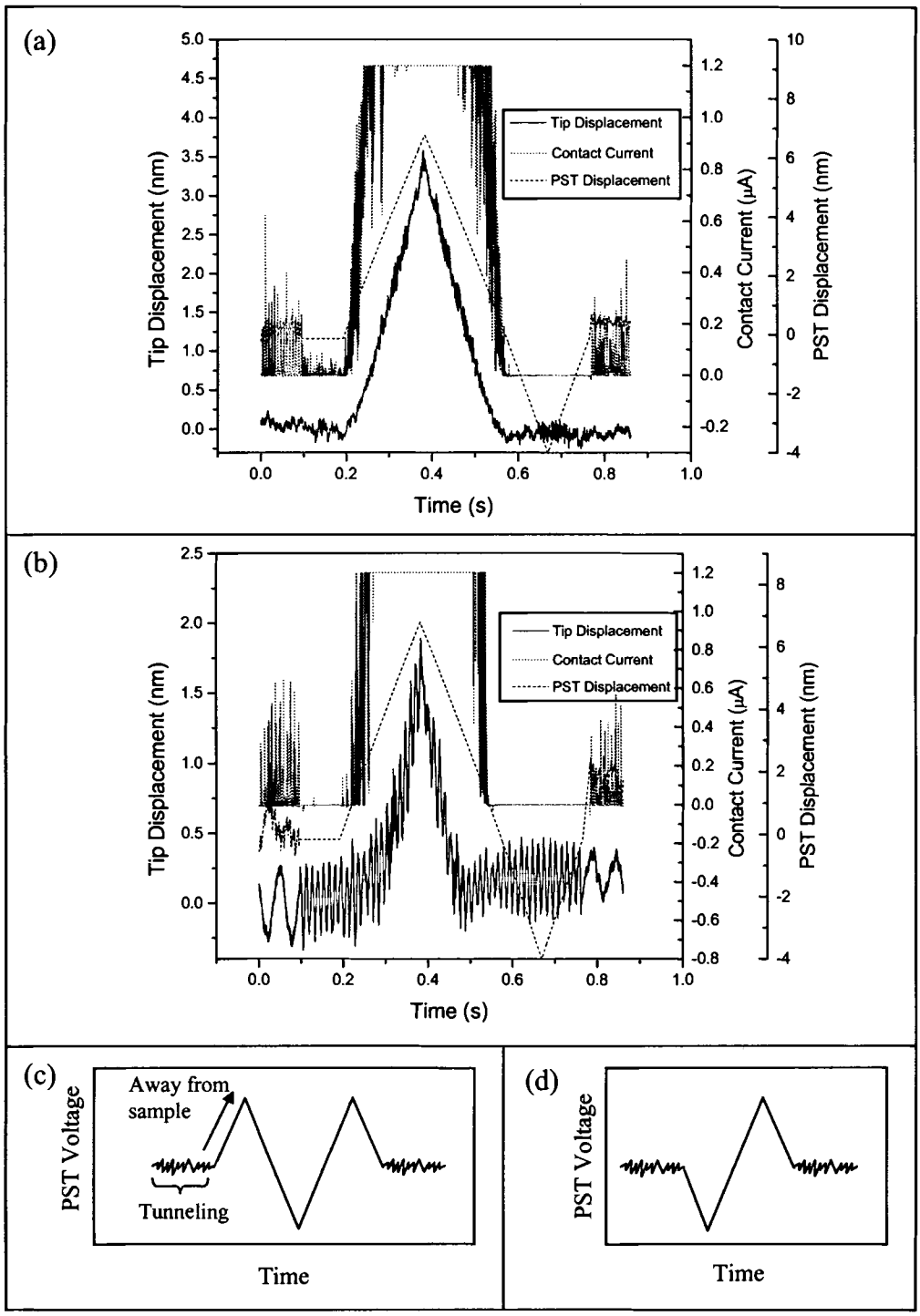

Figure 6.1: Problems in defining the origin. (a) Raw data showing noisy contact current during indentation. (b) Raw data showing noisy interferometer behavior. (c) PST displacement vs. time showing pullout from surface before indentation. (d) PST displacement vs. time showing indentation immediately from the tunneling position.

immediately after being in tunneling as shown in Figure 6.1d. During a procedure of type (1), Cross *et al.* [1] are able to see an attractive force as the tip approaches the surface before the repulsive force starts to dominate, as shown in Figure 6.2. This behavior is also seen during indentation experiments on gold using a tungsten tip [2,11] and on gold using a gold tip [8,12,13,14]. Since these forces are quite small (2 to 125 nN), it would be difficult to measure this attractive region using our apparatus since our typical force uncertainty is approximately ± 75 nN due to noise in the interferometer as discussed previously in Section 5.5. Recent studies have found this attractive force to be longer range than the van der Waals forces [14,15]. This longer-range force has been attributed to patch charges on the surface of the interacting bodies [15]. Also Cross has suggested three other possibilities for the long range force [3]: (1) there is gold on the tip and this influences the range of the force through an electronic effect (2) there is gold on the tip that diffuses under influence of force gradients, changing the length of the tip (3) the exchange correlation force between a tungsten tip and gold surface has a large scaling length.

6.3.2 Point of Initial Contact Defined by the Hertzian Contact Model

The consistent method that we used to define the origin of our force, F, versus penetration depth, d, curves was to use the Hertzian contact model (see Figure 6.3) and fit the theoretical Hertzian curve with our experimental data during the initial elastic region. Within the well-known Hertzian continuum model, the contact force between a spherical tip on a flat is given by [16]:

$$F = \frac{4}{3}\sqrt{R}E^{*}d^{\frac{3}{2}}, \tag{6.1}$$

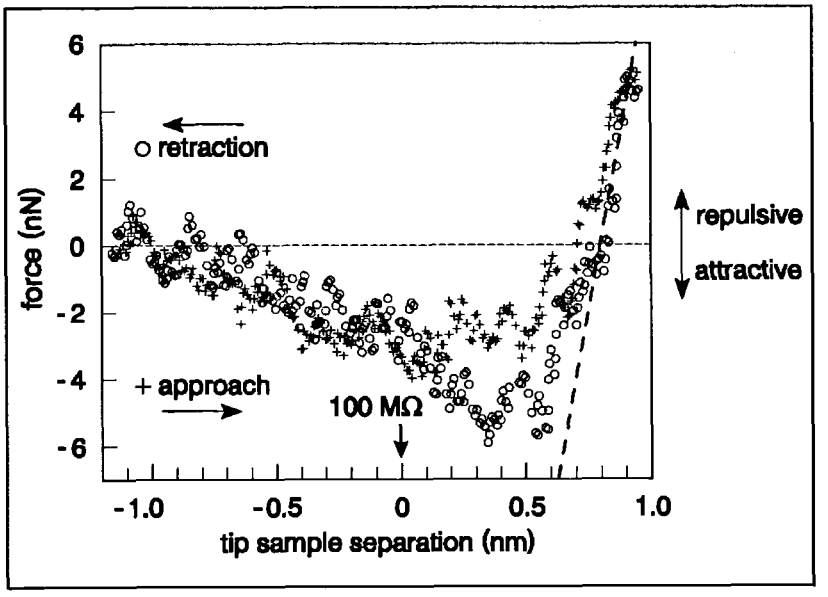

Figure 6.2: Indentation data measured from a W/Au (111) contact. Results show attractive and repulsive forces. From reference [1].

where R is the tip radius of curvature (in our case determined from FIM). E^* is the composite modulus given by the expression

$$\frac{1}{E^*} = \frac{1-\nu_{Au}^2}{E_{Au}} + \frac{1-\nu_W^2}{E_W}, \tag{6.2}$$

where E_{Au}, E_W, ν_{Au} and ν_W refer to the elastic modulus and Poisson ratios of gold and tungsten. We used E_{Au} = 82 GPa [17], E_W = 411 GPa [18], ν_{Au} = 0.45 [17] and ν_W = 0.28 [18]. This yielded a value of E^* = 81.5 GPa. Since $E_W >> E_{Au}$ which causes $E^* \approx E_{Au}$, we can safely assume that most of the elastic behavior takes place in the gold sample rather than the tungsten tip. Once the theoretical curve was drawn, the data was then shifted to match the theoretical curve in order to define the origin.

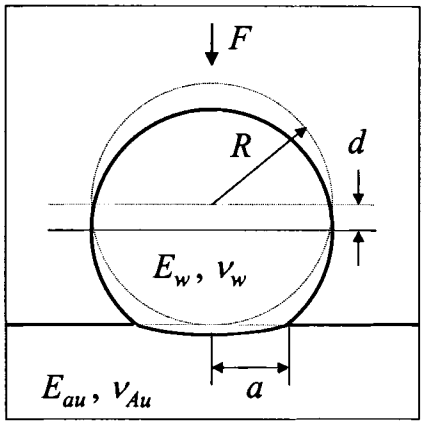

Figure 6.3: Schematic of the Hertzian continuum mechanics contact model. Elastic contact formed by a spherical tip contacting a flat surface. The parameters are defined in the text.

The Hertzian model is strictly valid under the following assumptions [16,19]:

1) The sphere radius R is much larger than the circular contact radius, a.

2) The materials are homogeneous, at least for a significant volume around the contact.

3) There is only elastic deformation.

4) The only force is an applied normal force, and there is no sliding or adhesion.

5) The surfaces are perfectly smooth.

Considering the elastic portion of our nanoindentation experiments, most of these conditions are met. The possible exceptions are that the force may not be a purely normal force due to a non-ideal tip and sample mounting, some adhesion forces may be present, and the surfaces may not be perfectly smooth. In the experiments where purely elastic indentations were performed, no adhesion was measured during the withdrawal procedure within the resolution of our interferometer. Furthermore, STM scans of the surface after the indentation showed that the surface was not perfectly flat, however, the

surface roughness was typically < 2.5 nm within a scan area of 400 nm x 400 nm. It is interesting to note that the Hertzian continuum model appears to remain a good approximation despite the fact the contact area in our experiment approaches dimensions containing only ~ 950 atoms.

6.3.3 Purely Elastic Indentations

Six indents were performed that showed purely elastic behavior (Figure 6.4). All of these curves were acquired using a 6 nm PST displacement. The agreement between the experimental data (points) and Hertzian model (solid line) is quite good for 5 of the 6 experiments. The one case that did not fit the model fell slightly below the theoretical fit (Figure 6.4f). This may have been due to one of the random noise events in the interferometer. Nanonindentation studies on gold by Houston *et al.* [17,20,21] also show agreement with a Hertzian model during the initial elastic regime. Their samples were treated with a self-assembled monolayer to passivate the tip-sample interaction, and eliminate adhesion effects. It is noteworthy that even though our surfaces were not treated to prevent adhesion, we also obtain good agreement with the simple Hertzian theory.

6.4 Initial Yielding and Plastic Deformation Under the Contact

Many of our experiments involved indentation forces that were large enough to exceed the elastic limit and cause material yielding and plasticity. In the experimental series with 9 nm PST displacement, yielding effects were always evident. For 19 nm PST displacements, the deepest indentation experiments that we performed, multiple yielding events were found to occur. For these deepest indentations the average

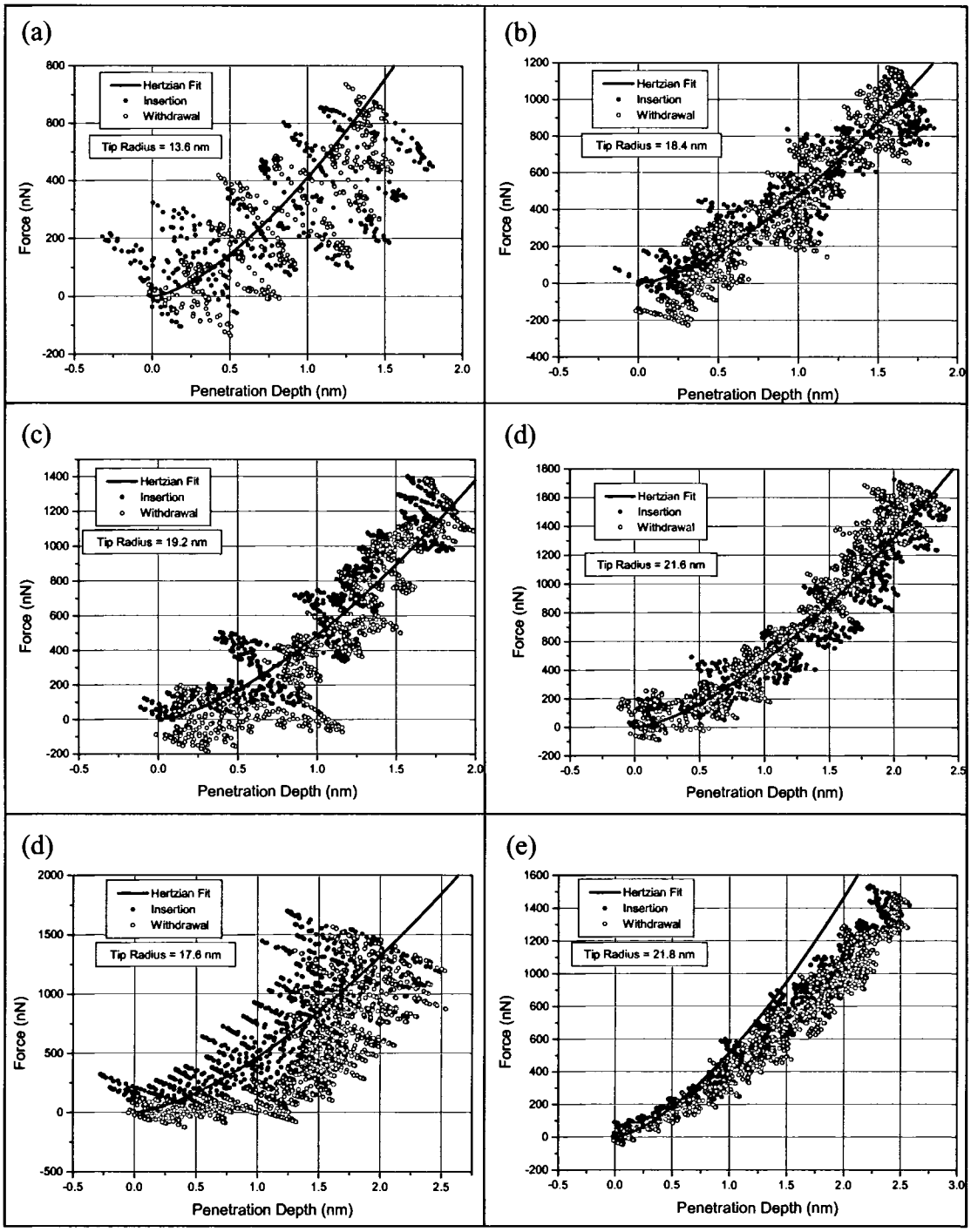

Figure 6.4: Elastic indentation results. Experimental elastic nanoindentation curve (points) fitted against the Hertzian contact model (solid lines).

penetration depth was 12.0 nm and the average tip radius was 16.2 nm. The larger tip displacement also meant that the signal to noise ratio was better than for the smaller indents. Some of the 19 nm PST displacement indentations were done over a time period of ~ 2 s rather than the ~ 380 μs time period. No noticeable difference was found between data acquired at these two different rates.

6.4.1 Hertzian Behavior During the Initial Elastic Regime

All of the 19 nm PST displacement indentation data were fitted against the Hertzian model prediction as discussed in Section 6.3.2. Good agreement was again found as shown in Figure 6.5 up to the point where the first measurable plastic yield event occurred. After the initial yield event there were usually several more yield events (see Figure 6.5a). Regions of elastic behavior, as demonstrated by similar slopes, separate the yield events consistent with other work [20,22]. Evidence for elastic behavior can also be seen in the last elastic event of Figure 6.5b. As the PST starts to retract the sample from the tip, there is no hysteresis observed with respect to the last elastic event.

The Hertzian model was not quantitatively compared to other elastic portions of the curve after the first yield event due to the uncertainty of where to define the new origin. Most of the 19 nm PST displacement indentations that were performed followed the theoretical Hertzian curve at the initial portion of the indentation curve. When the experimental data first deviated from the Hertzian curve, the first measurable plastic (or yield) event was observed. In Figure 6.5a the first yielding occurs at a penetration depth of 2.7 nm. The point of first yielding ranged from 1.2 nm to 2.7 nm for the series of experiments suggesting that the yield point depends on the exact dislocation density

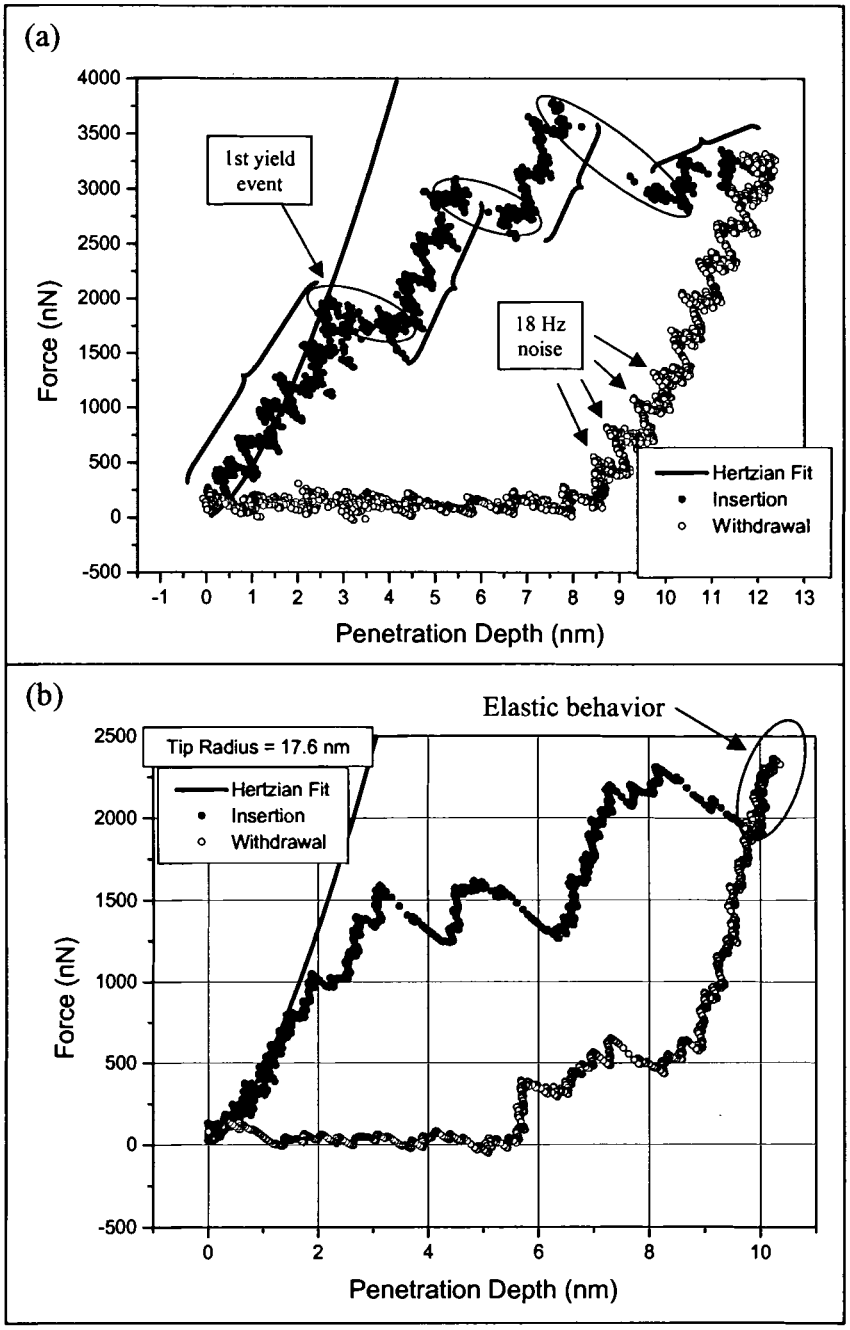

Figure 6.5: Force vs. penetration depth measured during 19 nm PST displacement indentation experiments. (a) Plastic and elastic events. The braces show the elastic portions of the curve and the ovals show where yielding events occur. (b) Evidence of elastic behavior following plastic yielding.

under the contact, which can vary from experiment to experiment, or the yield point may also depend on the tip radius. The data in Figure 6.5a also shows 18 Hz noise in the interferometer signal. Thus, we define yield events as events that are noticeably larger than the noise level. The interpretation of the slope observed during a yield event is discussed in Section 6.4.3.

6.4.2 Analysis of Initial Yield Stress

From the Hertzian continuum theory [16] the mean normal stress, $\bar{\sigma}$, at the threshold for plastic deformation is predicted to be

$$\bar{\sigma} = \frac{F_t}{\pi R d}, \tag{6.3}$$

where F_t is the force at the plastic threshold, R is the tip radius and d is the penetration depth.

A common way to estimate the shear stress beneath the tip while in contact with the surface is to take the maximum value of the principal shear stress using continuum elastic theory. The principal shear acts on planes that are inclined 45° to the surface at about a depth of $a/2$ below the axis of symmetry, where a is the radius of the contact area [19]. The maximum shear stress, σ_m, from continuum theory for gold is related to the mean normal stress by

$$\sigma_m = 0.465\bar{\sigma}. \tag{6.4}$$

Although most analyses take this approach, a recent simulation that models the indentation of a hard sphere indenter of radius 8 nm into Au (111) revealed that the nucleation of dislocations occurs on planes off the indenter axis [23]. Thus, most real systems may be more complex than continuum theory predicts.

The average value of the mean normal stress at the first yield event from our experiments was found to be $\bar{\sigma} = 12 \pm 2$ GPa with a range between 8 GPa and 14 GPa. The corresponding average maximum value of the principal shear stress was $\sigma_m = 5 \pm 1$ GPa. The uncertainty was determined from the standard deviation of seven different measurements.

Our results closely match other results in the literature. Using Eq. 6.4 to estimate the shear stress, Kiely and Houston [17] found $\sigma_m \approx 4$ GPa for Au (110) and Michalske and Houston [24] found $\sigma_m \approx 3$ GPa for Au (111). Moreover, it was found that the shear stress increased by about a factor of two as the tip radius decreased over the range 250 nm to 50 nm. Cross [3] did Au (111) indentation experiments using a very small tungsten tip radius of only 2.5 ± 0.05 nm. As the yielding point was approached, they found $\bar{\sigma} = 23 \pm 12$ GPa (corresponding to $\sigma_m \approx 11$ GPa) . Our tip radius size falls in between that of Cross and Houston *et al.* and our value of $\sigma_m = 5 \pm 1$ GPa is slightly larger than Houston's, which is consistent with the shear stress increasing as the tip radius decreased. This trend may be caused by decreased interactions with any intrinsic dislocations in the surrounding material as the contact gets smaller.

In experiments by Corcoran *et al.* [22] using a Berkovich diamond tip with a radius of curvature of about 205 nm, it was found that $\sigma_m \approx 3$ to 5 GPa for both Au (110) and Au (100). They also found that as the surface roughness increased, the shear stress decreased. Kiely *et al.* [25] had found similar results when investigating how surface steps affect the initiation of plastic yield events. It is believed that atomic steps act as nucleation sites for dislocations thereby lowering the yielding threshold. This effect may

be responsible for the variability in our measured yield points for the several different experimental runs.

Stalder and Durig [8,13] observed neck formations after a gold tip was pushed into a Au (111) sample and then pulled back out. As the tip was retracted from the sample, the contact went into tension as indicated by a negative force. Upon further withdrawal, it was found that the neck diameter stayed approximately constant until the point of maximum tensile force was reached. At this point the neck diameter started to decrease appreciably. Stalder and Durig defined the yield stress as the pressure at the point of maximum tensile force. The stress was calculated by dividing the contact area at that point by the maximum tensile force; contact area was determined from conductance measurements. This stress value is essentially the mean normal stress $\overline{\sigma}$ and it was found to range from $\approx$ 5 to 8 GPa, independent of the neck diameter. In computing this value, they subtracted out the energy needed to create new surface area along the neck. As a neck is being elongated, energy is needed to plastically deform the contact as well as to create new surface area along the neck. A simple model can be used to estimate the relative magnitudes of these two energies [26]. Modeling the neck as a cylinder with radius, r (Figure 6.6), the plastic energy, E_p, needed to plastically deform a length, Δx, of the cylinder is:

$$E_p = (\pi r^2)\Delta x \sigma_y \tag{6.5}$$

where, σ_y = 4 GPa, is the yield strength of gold. The surface energy, E_s, needed to create a new surface area, $(2\pi r)\Delta x$, as the cylinder extends, Δx, is:

$$E_s = (2\pi r)\Delta x \gamma \tag{6.6}$$

where, $\gamma = 1.12$ J/m^2 [26], is the surface energy of gold. These two different energies are equivalent to one another when $r = 2\gamma/\sigma_y = 5.6$ Å. Since $E_p \propto r^2$ and $E_s \propto r$, the plastic energy is dominant at values larger than 5.6 Å. However, for neck diameters on the order of atomic sizes, the surface forces become very important and need to be accounted for in yield stress determinations.

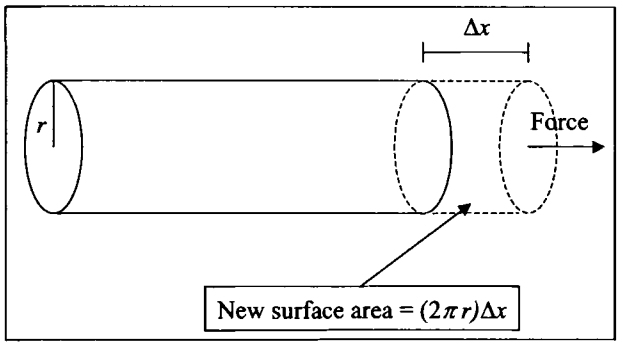

Figure 6.6: Connective neck modeled as a cylinder that is being stretched by a length Δx.

Experiments by Agrait *et al.* [14,26,27] have emphasized neck formation at gold–gold contacts. The experiments involved repetitive cycling of the tip-sample distance without breaking the contact. The conductance and force at the tip-sample contact were carefully measured. Discrete yielding events were noticed in the force and conductance, from which the maximum pressure that the neck could sustain before relaxation was calculated by taking the force at that point and dividing by the cross sectional area. Measured values were in the range of $\approx$ 2 to 6 GPa, and were also found to be independent of neck diameter. This pressure was measured to be as high as 13 GPa when the necks got very close to being one atom in diameter. However, this increase may be due to the increased surface forces for small contacts as discussed above, which they did not subtract out.

6.4.3 Time Response of Yielding Events

The slope of the force vs. penetration depth curve immediately after each yielding event contains information regarding the dynamics of the yielding event as well as the response time of the measurement apparatus. Figure 6.7a illustrates how the tip would respond versus time for the case where the tip holder could immediately respond to an instantaneous displacement during a yield event. The force of the tip on the sample is obtained by simply multiplying the tip holder displacement by its spring constant. The penetration depth is obtained by subtracting the tip holder displacement from the PST displacement. The corresponding force vs. penetration depth curve to Figure 6.7a is shown in Figure 6.7b. Since the penetration depth is plotted on the x-axis, even if the tip holder could immediately respond there is a non-vertical slope.

If the tip holder could immediately respond then a vertical line is expected on the tip displacement vs. time graph, but experimentally this is not observed. In Figure 6.8 an example is shown of a typical yield event measured with our apparatus. In this plot of the tip holder displacement vs. time, the yield event occurs over a $\approx$ 1.5 ms interval. Yield events in the W (110) and Fe–3% Si systems have been reported to occur over periods ~ 0.010 ms [21,28]. If our tip holder is modeled as a simple harmonic oscillator, then we can determine the relaxation time, τ, it would take for the tip holder to move from a position where it was instantaneously let go to its rest position. This time is simply equal to one-fourth its period, T. The relaxation time and period can be calculated from the angular frequency, ω, which is ultimately related to the spring constant, k, of the force sensor and the mass, m, of the tip holder as follows:

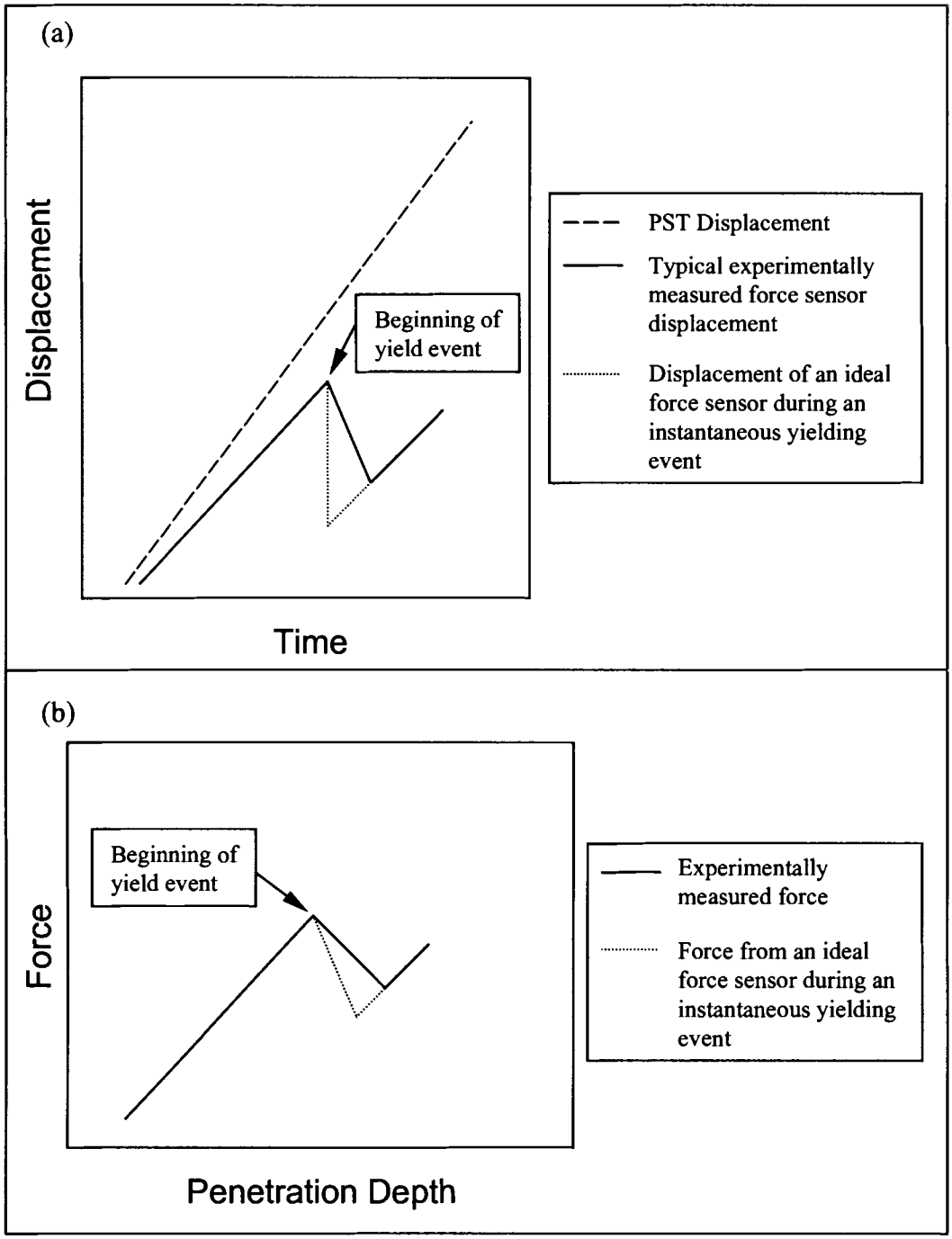

Figure 6.7: Ideal force sensor behavior versus measured results. (a) Displacement vs. time graph illustrating the differences expected between an ideal and real tip holder response. (b) The same comparison plotted on a force vs. penetration depth graph.

$$\tau = \frac{1}{4}T = \frac{1}{4}\frac{2\pi}{\omega} = \frac{1}{4}2\pi\sqrt{\frac{m}{k}}. \tag{6.7}$$

Taking the measured value for k = 442 N/m and m = 0.123 g, we get τ = 0.83 ms. Thus, it is evident that our tip holder itself will not follow the true yield event because its response time is too slow.

Since the tip holder only accounts for about half of the 1.5 ms that is experimentally measured, there is probably also some time delay in the electronics due to filtering of the interferometer signal or perhaps due to adhesion effects between the tip and sample. In Figure 6.8, a straight line has been drawn along the slope of the yield event. The data do not follow the straight line but show evidence for time delays at the beginning and end of the yield event. This non-linearity is further evidence for time delays in the force sensor, electronics and possibly due to adhesion effects between tip and sample. Figure 6.7b illustrates that the true force along the slope may be smaller than the measured value due to these time delays.

6.4.4 Hardness Values at Yielding Points

Hardness values were calculated at the beginning of each of the yield events for the indentation experiments. The hardness was determined by taking the force at the yield event and dividing it by the cross sectional area, A, of the tip in contact with the surface. This cross sectional area was estimated by assuming a rigid spherical tip in contact with the surface to a depth equal to the penetration depth, d, of the tip at the yield event (Figure 6.9a). The surface of the sample is assumed to perfectly conform to the shape of the rigid tip, although in reality this does not occur. Thus our contact area is an overestimate and will yield lower hardness values than what we would obtain if we could

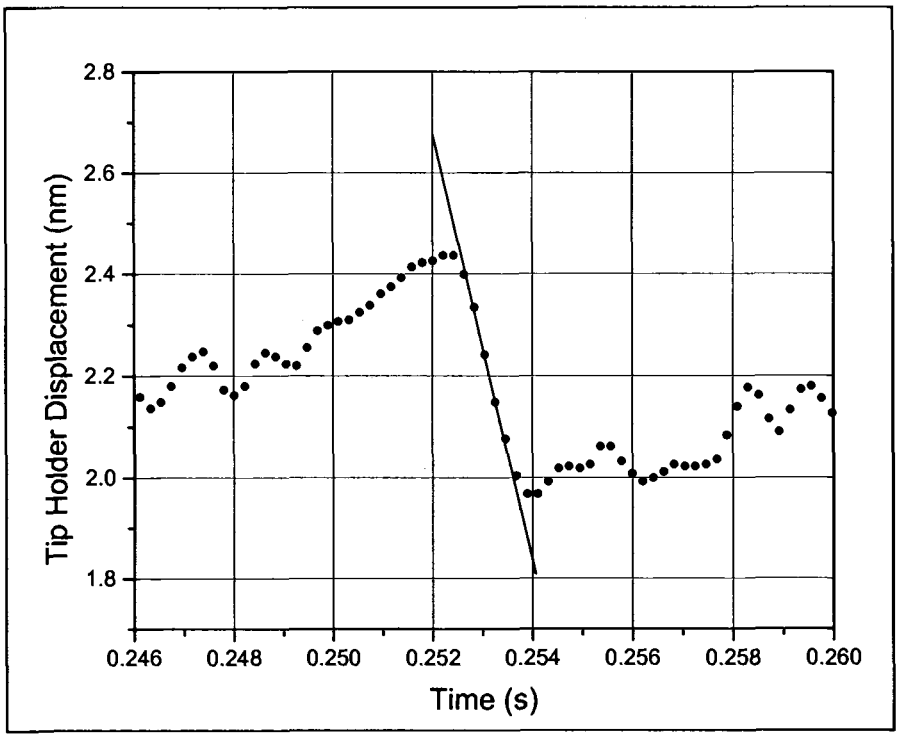

Figure 6.8: Portion of nanoindentation data showing a single yield event. The straight line shows that the data are non-linear, which is a result of the finite response times of the force sensor and measurement electronics.

measure the true contact area. Values of hardness versus penetration depth are plotted in Figure 6.9b and compared to data measured for larger indentation depths by Corcoran *et al.* [22] in Figure 6.9c. The data agree within the same order of magnitude, yet our values are about a factor of three larger probably due to the fact that Corcoran *et al.* used a tip radius about ten times larger than ours. The larger contact areas allow for a greater likelihood that the area below the contact has dislocation networks prior to the indentation that would lead to lower hardness values. This is consistent with even larger contact areas that are used in conventional microhardness testers, which yield a hardness value of 0.3 GPa on polycrystalline gold [29]. Note this value is more than an order of magnitude lower than our values. Our results show a considerable spread in our values

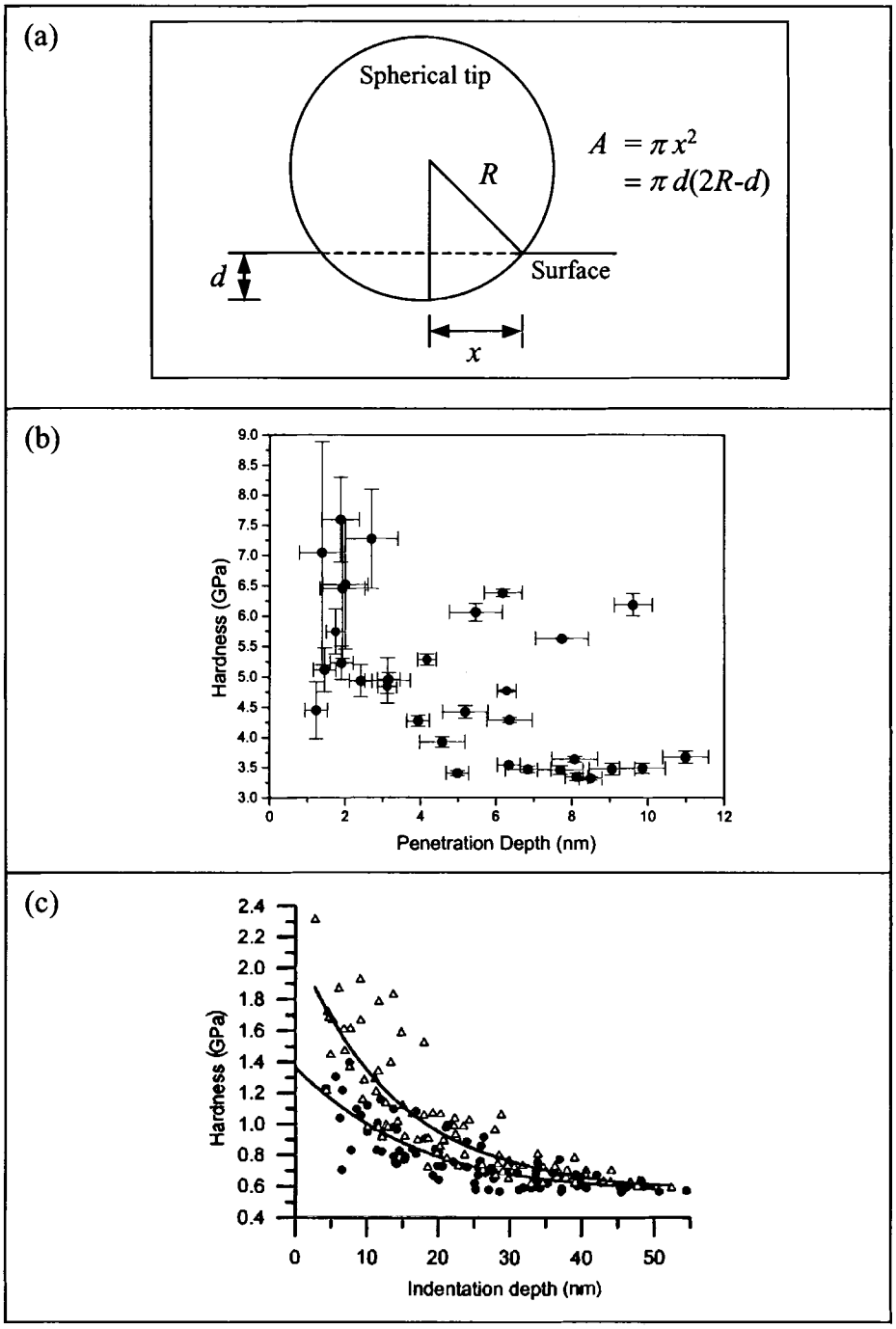

Figure 6.9: Hardness results. (a) Model used for determining the contact area in the hardness calculation. (b) Our experimental hardness values vs. penetration depth. (c) Hardness values vs. indentation depth measured by Corcoran *et al.* [22]. Note that their contacts were an order of magnitude larger in size.

just as in the data by Corcoran *et al.*, for indentation depths smaller than 12 nm. Most of the scatter in our data is likely due to the noise in our interferometer signal, particularly at the smallest indentation depths.

6.4.5 Possible Evidence for "Major" and "Minor" Yielding Events

Keily *et al.* [21] report two different types of yielding events during the initial indentation of gold. Their indentation curves follow the Hertzian model but eventually deviate from elastic behavior in one of two different ways, referred to as "major" and "minor" events. "Major" events exhibit a 20% or more drop in the force while "minor" events show a 5% or less drop in the force or an abrupt change in slope. Our data exhibited features that are supportive of these "major" and "minor" events as shown in Figure 6.10. In Figure 6.10a there is ≈18% drop in the load while in Figure 6.10b there is a change in the slope.

After each "major" yielding event, the tip is displaced by an average distance of 14 ± 7 Å before the next elastic event occurs. This distance may be an underestimate of the tip motion due to the time response of the force sensor as discussed in Section 6.4.3. The values ranged between 3 Å and 30 Å, and the uncertainty was determined from the standard deviation of nineteen different measurements. Keily *et al.* [21] found that the first "major" event was followed by smaller ones. This trend was not seen in our data.

6.5 Adhesion Effects and Break of Contacts

This section examines the portion of the force vs. penetration depth curve that occurs after the PST starts to reverse its direction and pull the sample away from the tip. The features in this regime result primarily from material relaxation and adhesion effects.

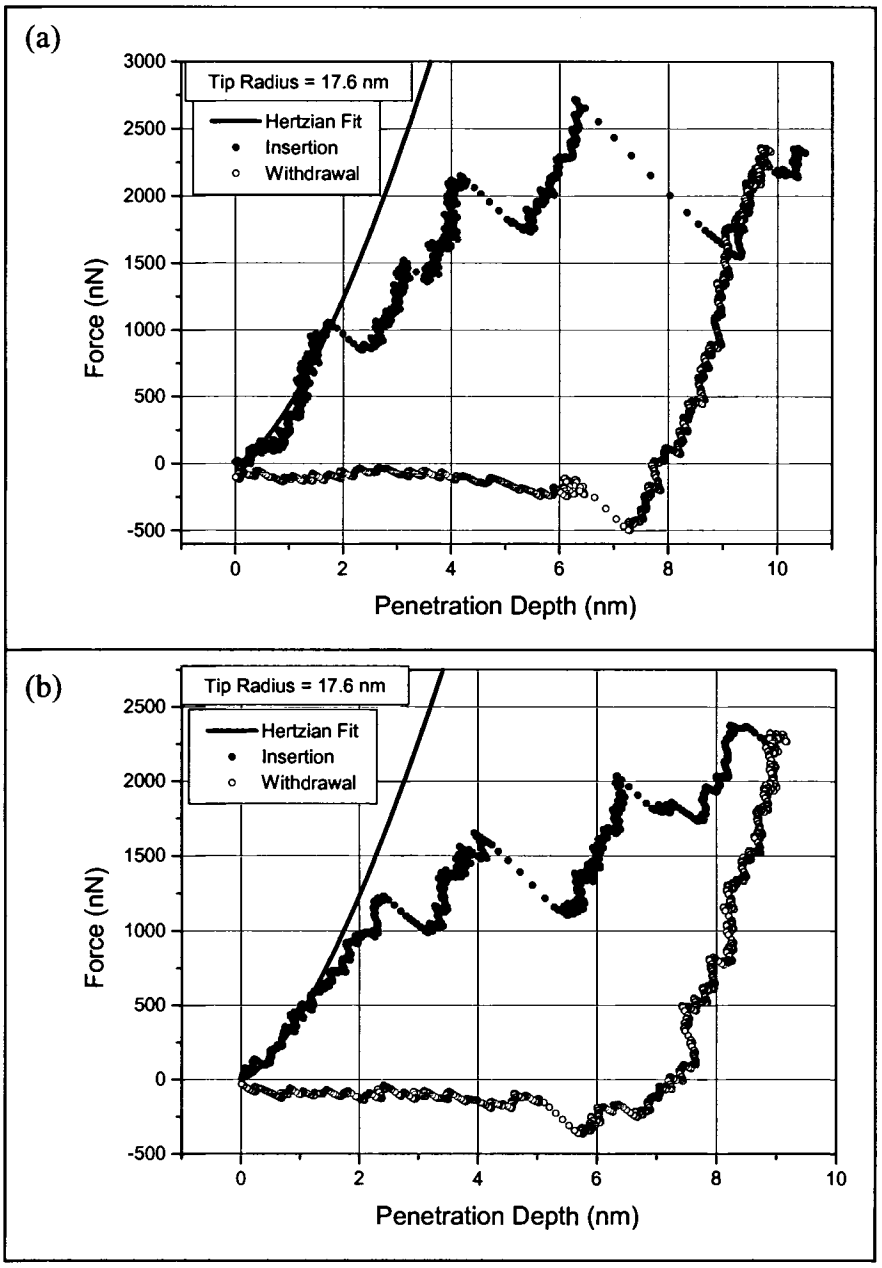

Figure 6.10: Possible evidence of (a) "major" and (b) "minor" yielding.

6.5.1 Pop-out Events

In some of the 19 nm PST displacement indentation curves, material relaxation events that show force signatures above our force noise level were observed. Examples of these features known as "pop-out" events are shown in Figure 6.11. During the withdrawal portion of the curve, there is a discontinuity in the force gradient at these pop-out events. These discontinuities mean that the tip holder essentially stops moving but the sample continues to move at the same rate. This suggests that the indentation depth in the sample becomes shallower via material relaxation that pushes on tip so as to keep the tip holder motion from following the PST motion. Hence material "pops-out" from the sample. Pop-out behavior is often found in indentation experiments on single crystal silicon [30]. One interpretation of these pop-out events is that they result from relaxation of densified material during the withdrawal portion of the indentation [31]. Another explanation is that lateral cracks form in the sample under the indent that push material away from the surface [32]. To our knowledge, our measurements are the first report of pop-out signatures for gold.

6.5.2 Adhesion Model

The Hertzian contact model does not take into account adhesion. Several contact models have been proposed to predict adhesion forces during the withdrawal portion of the force vs. penetration depth curve in order to compare with experimental results. The Derjaguin, Muller and Toporov (DMT) [33] contact model and the Johnson-Kendall-Roberts (JKR) [34] contact model are two of the best-established theories used for elastic adhesive contacts. In these models, the two materials that comprise the contact are assumed to be isotropic, no friction occurs between them, and $a << R$ (see Figure 6.3).

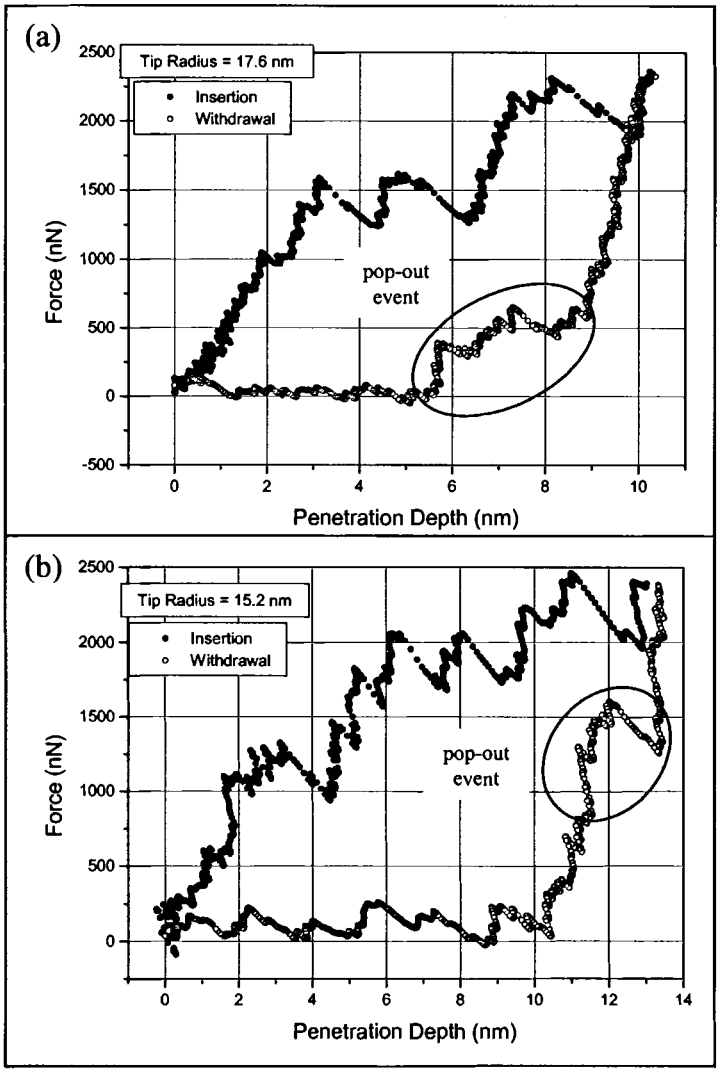

Figure 6.11: Examples of force vs. penetration depth curves which show evidence for pop-out events.

Tabor showed that the DMT and JKR theories are limiting cases of a more general approach [35]. The JKR model only takes into account forces acting within the contact area, while the DMT model also takes into account forces that act outside the contact area. The JKR model is more appropriate for materials with high elasticity, short-range forces and large surface adhesion. The DMT model predicts a larger maximum adhesion force than the JKR. Deciding on which model to use is determined through the elasticity parameter, λ_e [36], given by:

$$\lambda_e = \sigma_o \left(\frac{9R}{2\pi W_{ad} E^{*2}} \right)^{\frac{1}{3}}, \tag{6.8}$$

where σ_o is the stress at the equilibrium position, R is the radius of curvature of the tip, W_{ad} is the adhesion energy and E^* is the composite modulus. Using the Dugdale potential, $\sigma_o = W_{ad} / h_o$ [36]. For our experiments with W/Au contacts, the average tip size R = 17 nm, the adhesion energy is W_{ad} = 0.53 nN/nm [3], E^* = 81.5 GPa (see Section 6.3.2), and a reasonable approximation of h_o = 0.2 nm, which yields a value λ_e = 0.51. When λ_e is small ($\lambda_e < 0.1$) the DMT model is the best model to use, and when λ_e is large ($\lambda_e > 5$) the JKR model is the best model to use. Since our value of λ_e is small, the DMT model is reasonable to describe our results. Figure 6.12a graphically shows the DMT result in comparison to the Hertzian model. It is noted that the theoretical curve of the DMT model is identical to the Hertzian curve except it is shifted along the y-axis by an amount - $F_{pull\text{-}off}$. In this DMT model, the pull-off force, $F_{pull\text{-}off}$, is given by

$$F_{pull-off} = 2\pi R W_{ad} . \tag{6.9}$$

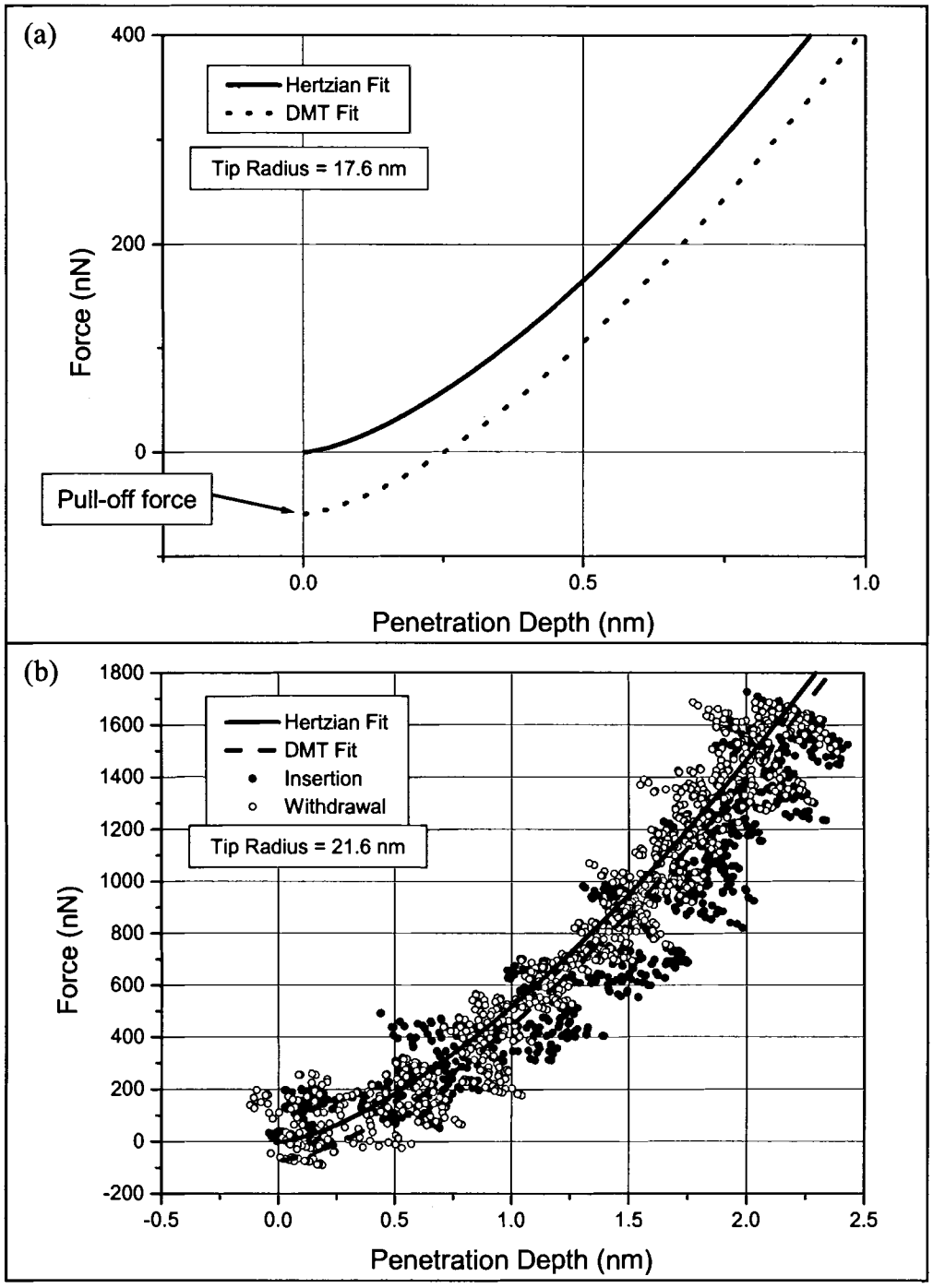

Figure 6.12: Hertzian versus DMT contact model. (a) Comparison between a Hertzian and a DMT curve for the case of an indentation between a tungsten tip, with radius = 17.6 nm, and a gold sample. The pull-off force = 59 nN. (b) Hertzian vs. DMT fit for one of our data sets; the pull-off force = 72 nN.

Referring to the purely elastic data shown in Figure 6.4, the tip radii in our experiments spanned from 13.6 nm to 21.6 nm. The minimum tip radius of R = 13.6 nm yields $F_{pull\text{-}off}$ = 45 nN, whereas for the maximum tip radius of R = 21.6 nm a value of $F_{pull\text{-}off}$ = 72 nN is obtained. In Figure 6.12b, an example of our elastic indentation data is plotted along with the corresponding predictions from the Hertzian model and DMT model. Due to our experimental noise in the force measurements we can not clearly distinguish between a non-adhesion Hertzian fit and an adhesive DMT fit.

Other groups who have done nanoindentation experiments on gold, have observed adhesion and have compared adhesion models with their results. Burnham *et al.* [11,15] observed long range adhesion forces possibly arising from van der Waals forces or patch charge effects (as mentioned in Section 6.3.1) during the precontact portion of the indentation. They modeled their results using van der Waals forces and found the forces to be too short ranged, but when they modeled using patch charge effects their results showed better agreement with the long-range force. During the retraction portion of the indentation, Cross [3] analyzed adhesion in elastic indentations using the Maugis-Dugdale (MD) theory and the Rose-Ferrante-Smith (RFS) potential. In Cross's data set the results matched fairly well except that the model did not predict the long-range force that was noticed as the force approached zero.

For the case of the 19 nm PST displacement indentations the maximum tip radius was 17.6 nm. This corresponds to a maximum $F_{pull\text{-}off}$ = 59 nN from the DMT model. This value is about ten times less than the actual pull-off force we measured experimentally. However, the model assumes elastic behavior and no shear, assumptions that are clearly not met in these multiple yielding event experiments.

In summary, we have found that the DMT model is not suitable to model the pull-off force of our multiple yielding experiments. Also, for our elastic experiments the DMT model predicts results that we can not differentiate from the Hertzian model within the resolution of our interferometer. In fact we could have chosen the DMT model to define our origin, but we chose to define the origin using the simpler Hertzian model.

6.5.3 Neck Formation During Break of Contact

In carefully done experiments on Au/Au contacts, with high resolution current and force measurements, necks have been noticed to form as the contact is pulled apart. The neck decreases in diameter in a series of discrete events as the force approaches zero [8,13,27,37,38]. These experiments were performed by pushing gold tips into gold samples where most likely the tip shape was very much changed after the neck formation. The series of discrete events are thought to represent the atomic rearrangement of atoms within the neck as the atoms disorder to form a new layer within an elongated neck [39]. Evidence for neck formation is found through the combination of discrete current changes that correspond with discrete changes in the force. From the current, the diameter of the connection between the tip and sample can be determined while from the force, the tip to sample distance can be determined. From experiments of this type it is seen that discrete events in the force and current measurements correspond with one another. The measurements show that the connection gets smaller as the tip to sample distance separates meaning that the neck elongates and finally breaks.

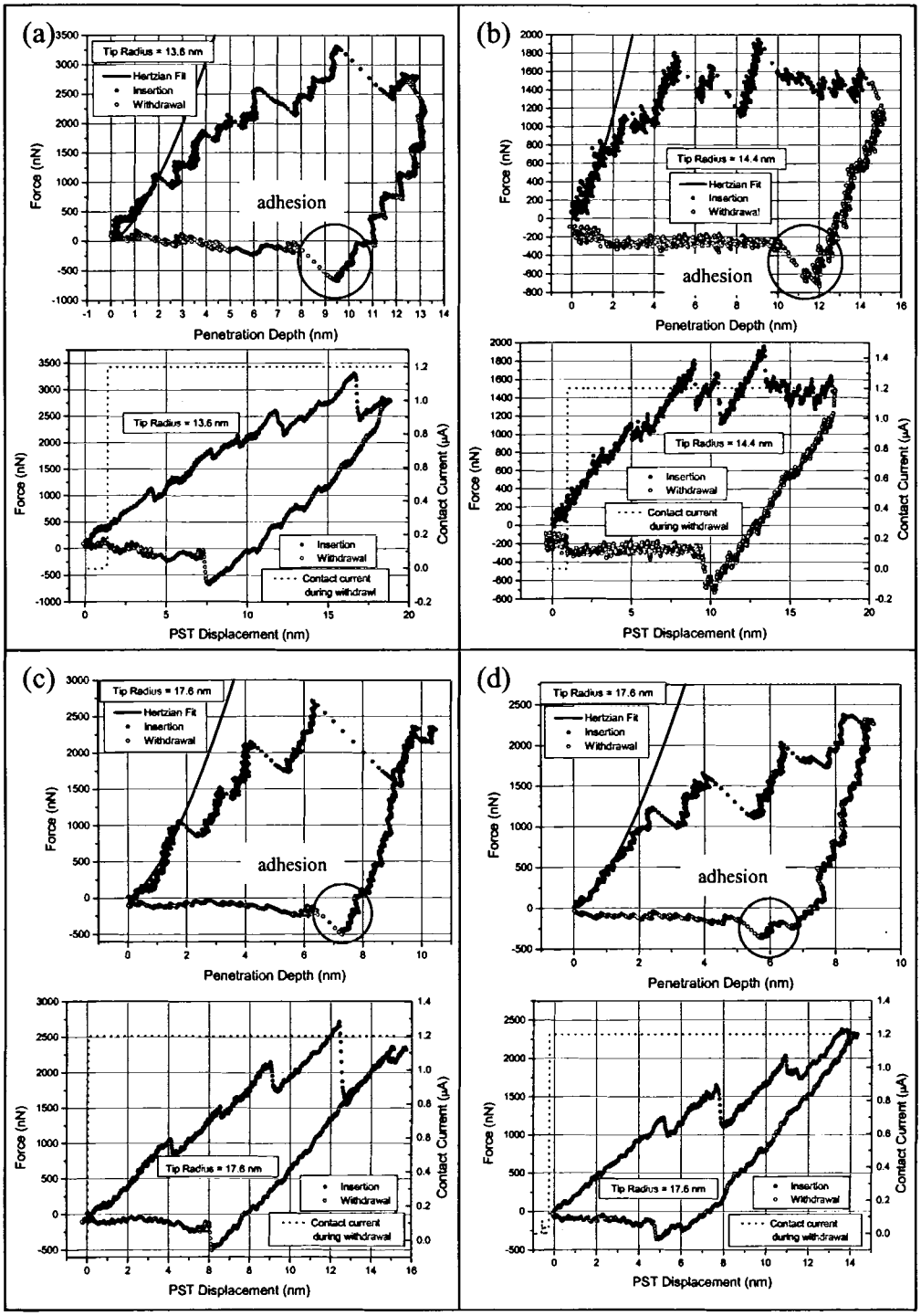

Figure 6.13: Adhesion evidence. Force vs. penetration depth curves are shown with their corresponding force vs. PST displacement curves for 19 nm PST displacement indentations illustrating evidence of adhesion. The circled regions indicate a major excursion in the adhesive force. On the force vs. PST displacement curves, the contact current between the tip and sample measured during break of contact is shown.

Four of the 19 nm PST displacement curves that we measured clearly showed a negative force for a portion of time during the withdrawal portion of the experiment (see Figure 6.13). This negative force is clearly larger than the noise level and appears to be only a single event. In the Au/Au necking experiments mentioned above, the discrete events occur in increments on the order of ~ 10 nN, and the tip was found to move ~ 2.5 Å during each event. In our experiments, the uncertainty in force was ~ ± 75 nN, and thus we were unable to detect any of these discrete steps with our instrument. However, we observe a peak value of negative force followed by a significant change where the force suddenly approaches zero. When this negative force excursion was present, the average tip to sample distance from the point of zero force to the point of maximum negative force was 13 ± 5 Å, and the average maximum negative force found was 550 ± 140 nN. The errors given are estimated systematic errors. This maximum negative force can be equated with the point of maximum tensile force that Stalder and Durig used to calculate the yield strength [8,13] as discussed in Section 6.4.2. Our maximum tensile force of 550 nN falls within the range of maximum tensile force values that Stalder and Durig measured. Furthermore, the maximum tensile force scales with the contact diameter consistent with Stalder and Durig [8,13], and Agrait *et al.* [14,26,27] observations that the yield strength does not depend on the contact diameter. Since a deeper indent implies a larger contact area between tip and sample, then a larger tensile force will be needed before yielding starts.

The tip-sample current was measured throughout our experiments including when there was a break in electrical contact between tip and sample. Because the break to contact occurred so quickly there were very few data points. Also, sometimes the break

to contact was noisy as in Figure 6.1a and 6.1b. Thus we were unable to make accurate current measurements to determine the diameter of contact as other groups have done. However, we were at least able to tell when there was a break of electrical contact to an accuracy of ~ 1 nm. Since our tip radii were on the order of 17 nm, then the contact area must have a radius < 17 nm. An estimate can be used to relate the conductance to contact area. The mean free path length, l, for electrons = $v_m \tau_e$, where v_m is the root mean square velocity and τ_e is the relaxation time. From statistical mechanics, v_m is related to the absolute temperature, T, by the following expression:

$$v_m = \sqrt{\frac{3k_B T}{m_e}}, \tag{6.10}$$

where k_B is Boltzmann's constant and m_e is the mass of an electron. At 273 K, v_m = 1.11×10^5 m/s and $\tau_e = 3.0 \times 10^{-14}$ s for gold [40]. Thus l = 3.3 nm for gold at 273 K. Since the mean free path length of the electrons is on the order of the radius of the contact, $a_{contact}$, we shall use the Sharvin formula [41] to relate the contact radius to the conductance, G:

$$a_{contact} = \sqrt{\frac{4G\rho l}{3\pi}}, \tag{6.11}$$

where ρ is the resistivity of gold, which is 2.04×10^{-8} Ω m at 273 K [40]. The maximum current that we can measure due to limitations in our electronics is 1.2 μA. We used a tip to sample voltage of 156 mV, so for a current of 1.2 μA the conductance is 7.69×10^{-6} A/V which, by using Eq. 6.11, corresponds to a contact radius of 0.15 Å. For a current of 1.2 μA, the contact radius is much less than the mean free path length of the electrons in gold, therefore the electrons are in the ballistic transport regime and the Sharvin formula

is valid [41]. We therefore see that whenever our contact current is less than its maximum value we are dealing with contact diameters less than one atom in size, so there is essentially no contact between tip and sample. In Figure 6.13 we show force vs. penetration depth curves as well as corresponding force vs. PST displacement curves. The contact current during withdrawal is best displayed on a force vs. PST displacement curve. We found that the average tip to sample distance from the point of zero force until there was no measurable electrical contact was 8.7 nm. Therefore, even after the force approaches zero (after the negative excursion event) there is still electrical contact until a much further displacement of the PST.

Several possible scenarios can explain the measured signatures during the negative force portion of the curves. One situation is that a neck could form between the tip and sample. The sharp change in the force after the negative excursion event could be the first atomic rearrangement of the neck. This first event may be a significant event, and subsequent atomic events may be of smaller size that are below the resolution of our instrument. These smaller events could take place until the time when the contact current drops to zero. This scenario would suggest neck lengths on the order of 9 nm before they break. A similar result is seen with a Au/Au contact experiment, where the neck length is also about 9 nm at breakage [8]. A molecular dynamics simulation of a 3 nm nickel tip indentation into Au (100) showed a neck length at breakage of 1.8 nm [39]. Our tip had a much larger radius than this simulation and hence there is a larger contact area between sample and tip. Therefore, it is reasonable that our neck length would be larger. Rather than having a single neck formation there may also be the possibility of having multiple neck formations making up the contact, especially for larger contacts.

Another situation that could explain the negative force signature in our data is that there could be adhesion between the tip and sample without any neck formation. During tip withdrawal and after the tip has entered the negative force regime, this adhesion could occur by the tip sliding along the contour of the indentation hole. A lateral force that causes the tip to follow the hole contour may be caused by vibrations, creep in the PST, or possibly a nonsymmetrical indentation hole shape. Initially the negative excursion event could result when the pulling apart force becomes greater than the adhesion force, and subsequently the tip would quickly slide along the contour of the hole towards its rest position. As the tip slides along the contour, electrical contact would be maintained but the new interactions between the tip and sample along the contour would have a much smaller adhesion force due to a much smaller contact area. The data would show electrical contact after the negative excursion event with very little or no tip motion consistent with our data. If we put this in the context of the DMT model and estimate the surface adhesive force as the retracting tip moves along the contour, we find the pull-off force ~ 59 nN. Again this value is below our interferometer noise level, hence this is consistent with our data not displaying a measurable force after the large excursion event.

Monitoring the contact current with better resolution would clarify whether or not there was neck formation in our experiments. Discrete decreasing changes versus a continual change in contact current should correspond to the neck formation versus the tip sliding along the contour mechanisms. It is not unreasonable to think that the break of contact involves a combination of the above situations or more complex necking mechanisms.

It is interesting to note that only four of the seven 19 nm PST displacement indentation experiments showed any clear evidence of a negative force signature. Thus within the resolution of our measurement, the negative force signature event does not always occur. Two of the experiments which did not show adhesion were experiments that showed pop-out events (see Figure 6.11). The pop-out event may decrease the contact area between the tip and sample hence leading to a smaller adhesion force that is difficult to measure with our interferometer.

6.6 Post Indentation Analysis of Tip and Sample Deformation

6.6.1 FIM Analysis

After an indent was performed the sample was immediately scanned in STM mode using the same tip used for indentation; the tip was then also imaged using FIM. Figure 6.14 shows a typical series of FIM images from one of the experiments. Figure 6.14a shows an FIM image of the tip before the indentation that was acquired at a voltage of 10.69 kV. Figure 6.14b is an FIM image of the tip after the indentation as the voltage was first raised to 10.00 kV. This FIM pattern is considerably different. In a separate set of experiments, we looked at tip contamination effects by performing FIM on tungsten tips before and after the imaging voltage was turned down and then turned back up to the same imaging voltage. The only parameter in these static tip experiments was the time before the imaging voltage was turned back up again. It was found that even after only a few seconds, the tip exhibited contamination features that could be seen in the FIM pattern. This happened even though the base pressure in our chamber was $< 3.0 \times 10^{-10}$ torr. For this reason, it is difficult to determine whether the change in the FIM pattern

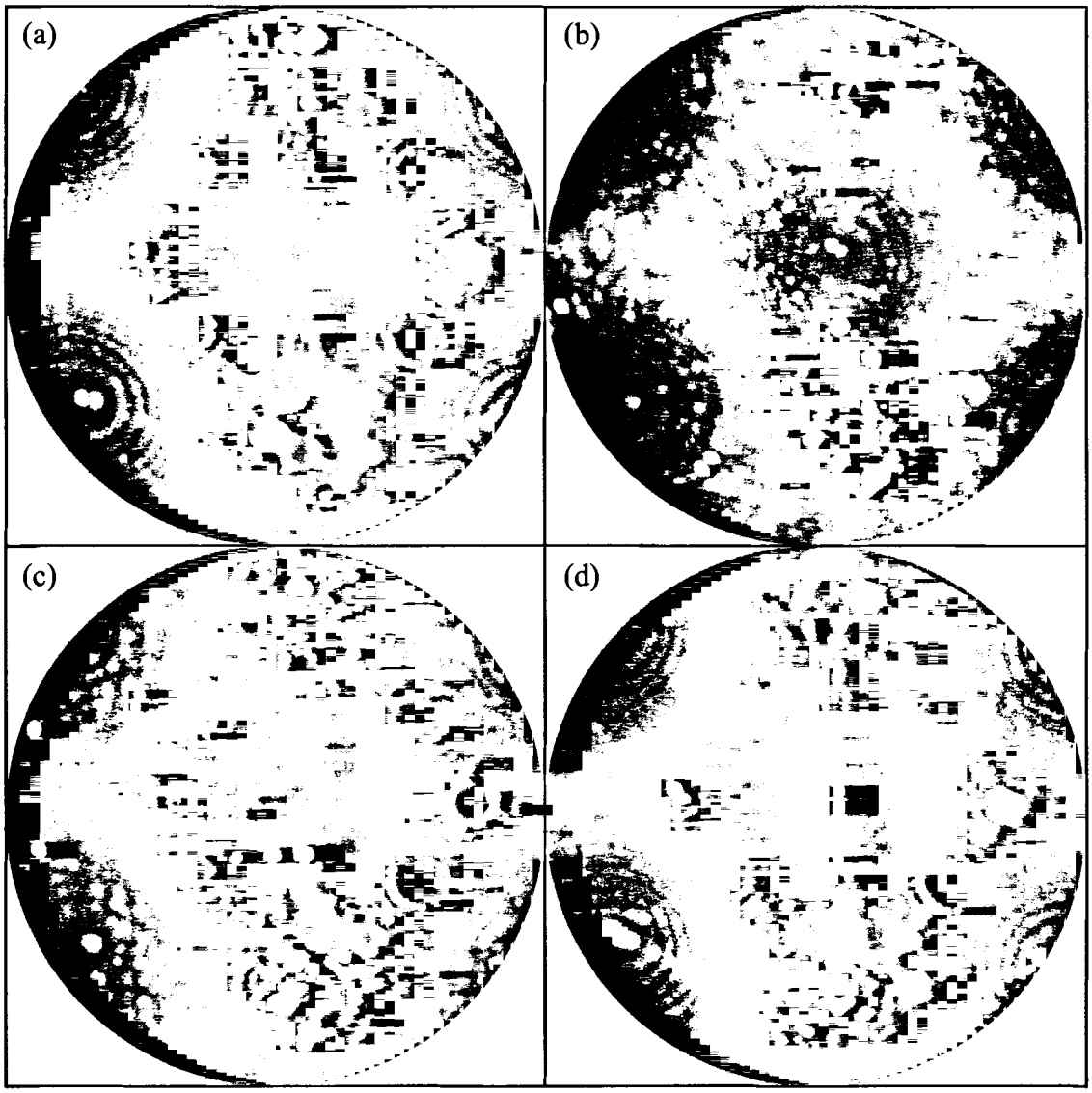

Figure 6.14: A typical series of FIM images before and after an indentation experiment. (a) FIM before indent at 10.69 kV. (b) FIM after indent at 10.00 kV. (c) FIM after indent at 10.69 kV. (d) FIM after indent at 10.69 kV, after it was turned up to 11.42 kV to field evaporate four atomic layers off the (110) pole and then turned back down to 10.69 kV.

from Figure 6.14a to Figure 6.14b is a result of gold transfer to the tungsten tip or due to other contaminants adhered to the tip.

An important issue to consider is whether or not any gold adhered to the tungsten tip field evaporates before the imaging voltage was reached. The evaporation field strength for gold is 35 V/nm and 57 V/nm for tungsten [42]; likewise, the best imaging field (BIF) when using helium gas is 44 V/nm. Thus, from these data it seems that gold should readily evaporate off the tip before an FIM pattern is seen. However, this appears not to be the case since other groups have confirmed that gold can remain stable on a tungsten tip at its imaging voltage [43,44]. Hydrogen is difficult to pump from a vacuum system using turbo/ion pumping. Residual hydrogen has a BIF of 22 V/nm [42] and may possibly be responsible for the gold imaging [44].

In Figure 6.14b some of the poles and their concentric rings associated with the original FIM pattern are still visible suggesting that the original tungsten surface is still intact under the contaminants. The concentric rings around these poles do not collapse upon themselves as atoms are field evaporated at higher voltages. This means that we can say that almost all the atoms that are field evaporating are gold or contaminant atoms, rather than tungsten atoms.

Figure 6.14c shows the FIM image of the tip returned to its original imaging voltage of 10.69 kV. The tip differs from Figure 6.14a indicating that it is still contaminated. The concentric rings around the poles still do not collapse upon themselves. Figure 6.14d shows the FIM image after the imaging voltage was turned up to 11.42 kV to field evaporate four atomic layers off the W (110) plane and then returned

to 10.69 kV for imaging. It is evident that the contaminants have finally been field evaporated along with some of the tungsten atoms.

Our FIM results, unfortunately, do not reveal detailed information about material transfer between the tungsten tip and gold sample. However, FIM images did provide accurate measurements of tip radii. In addition, the FIM results indicate that there is no appreciable plastic deformation or massive material removal from the tip during the indentation even after multiple yielding events have occurred in the gold. Had there been appreciable tip deformation or material removal, the concentric rings around the poles would have exhibited new shapes and/or locations, or defects such as dislocations or grain boundaries would have been evident in the FIM images.

Several other studies have been carried out in which a tungsten tip was indented into gold and then imaged afterwards with FIM [1,2,3,44,45,46,47]. Figure 6.15 shows a series of before and after FIM images of a tungsten tip (radius ~ 35 nm) after it was indented into gold acquired by Brainard and Buckley in 1971 [47]. Their experiment was not done in a very controlled manner and no indentation forces were monitored. However, their results are very similar to our data in that the underlying tungsten pattern is observed and becomes more pronounced as the field evaporation progresses. They also suggest that the diffuse spots seen in Figure 6.15b and 6.15c are clusters of gold atoms on the surface of the tip. Our results in Figure 6.14b and 6.14c also show evidence of clusters.

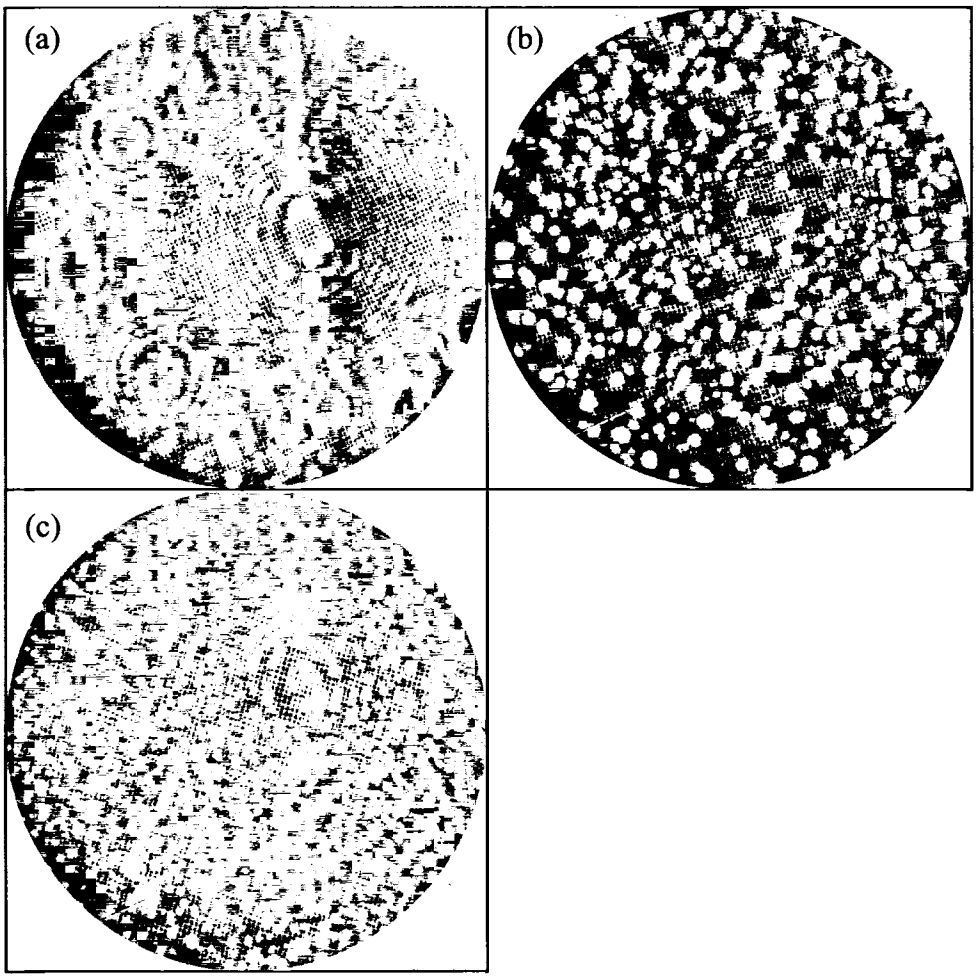

Figure 6.15: FIM before and after a tungsten / gold indentation using a tip radius of ~ 35 nm from Brainard and Buckley [47]. (a) FIM before indent. (b) FIM after indent at a voltage lower than the before indent FIM image. (c) FIM after indent at the same voltage as the before indent FIM image.

Recently Grütter *et al.* has utilized FIM in interpreting well-controlled nanoindentation experiments on gold [1,2,3,4,44]. Despite the fact that their indentation size regime was smaller than ours and that they emphasized the purely elastic regime compared to plastic yielding in our experiments, the FIM results are the same, namely that there is no appreciable tip deformation during the W/Au nanoindentation process.

6.6.2 Indentation Shapes

Since gold is an fcc crystal, slip occurs along the close-packed {111} planes in ⟨110⟩ directions [48]. The plastic deformation volume caused by indentation into a Au (110) surface therefore contains crystallographic features associated with these slip planes as shown in Figure 6.16. The angle between adjacent {111} planes that intersect the surface is either 109.5° or 125.3°. Four of the {111} planes make an angle of 90° with the surface and two of them make an angle of 35.3° with the surface. The (111) and the $(\bar{1}\bar{1}1)$ planes intersect at the bottom of the hole, where the dotted line is located, to form a wedge with an angle of 109.5°. The exact shape of the indent itself can have many different variants due to different combinations of {111} slip events during the indentation process.

Immediately after performing an indentation experiment, the hole was imaged using the same tip in STM mode. Figure 6.17 shows four examples of scans from different indents and also illustrates how different shape variants can form. It is noted that the STM scans were not corrected for hysteresis so the dimensions are not strictly correct. The variants in the indentation shape may be caused by the fact that the tip was

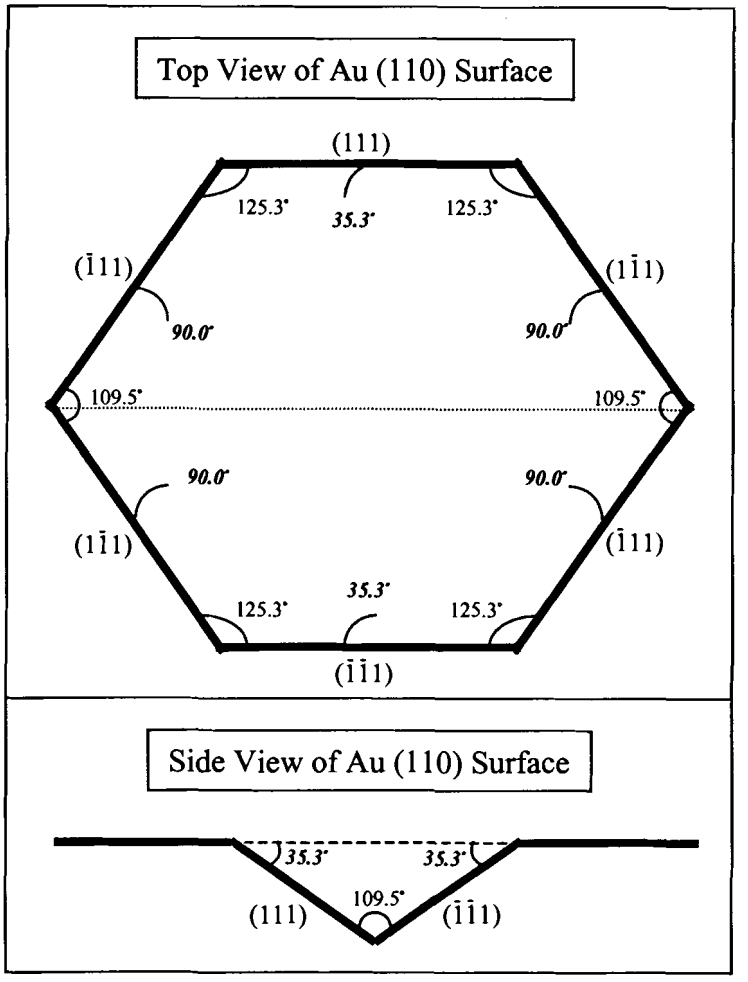

Figure 6.16: Indentation hole. View of an idealized hole formed by a load applied normal to a Au (110) surface. Slippage occurs along {111} planes which are marked in the figure. The angles between adjacent {111} planes that intersect the surface are 109.5° and 125.3°. Four of the {111} planes make an angle of 90° with the surface and two of them make an angle of 35.3° with the surface. The (111) and the $(\bar{1}\bar{1}\bar{1})$ planes intersect at the bottom of the hole, where the dotted line is located, to form a wedge with an angle of 109.5°.

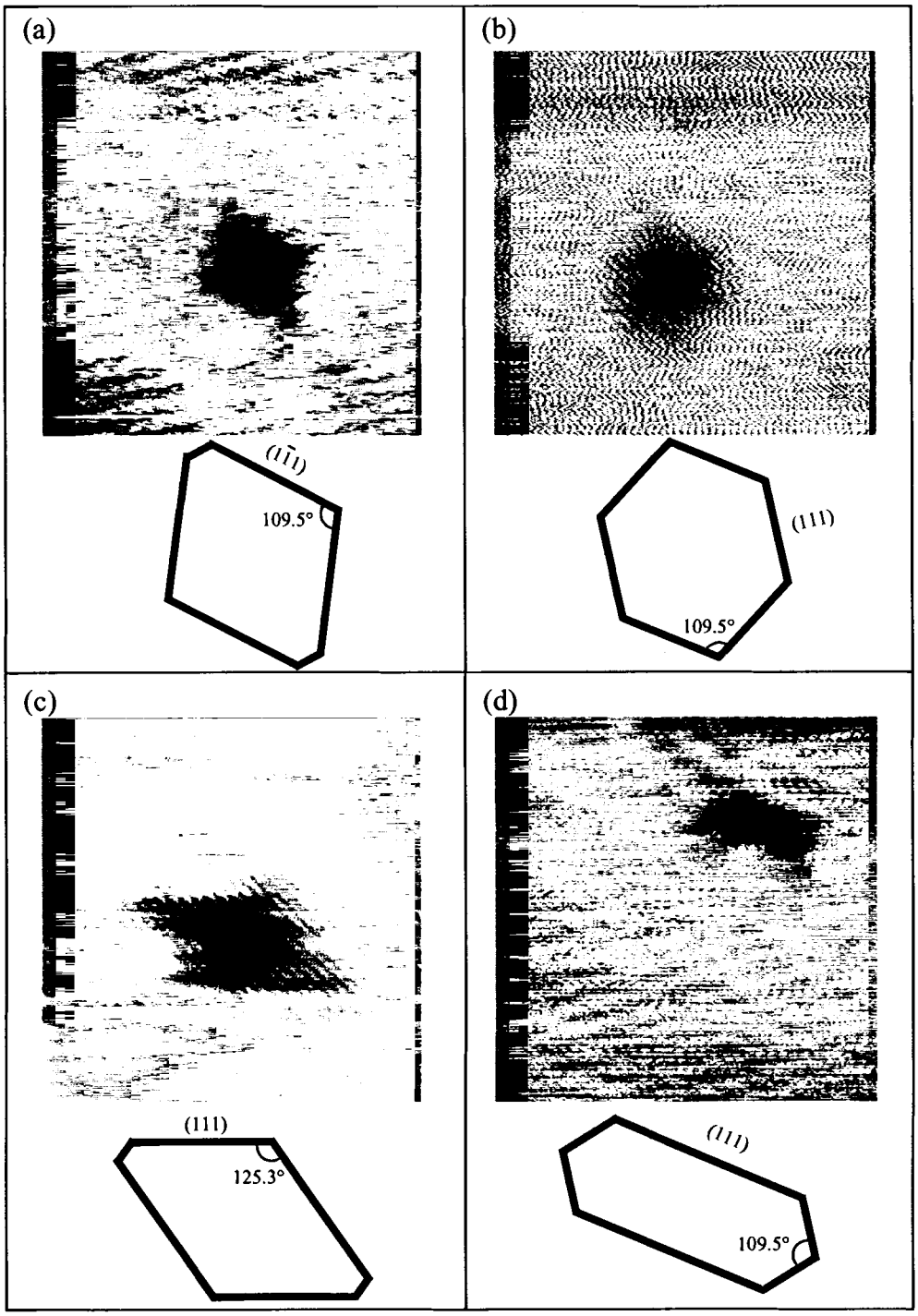

Figure 6.17: 400 x 400 nm STM scans of Au (110) after indentation. Accompanying each scan is a suggested schematic of how the sides of Figure 6.16 may lengthen or shorten to form the indent shape.

probably not perfectly normal to the surface as mounted in the force sensor. This slight misalignment would cause preferential slippage along certain {111} planes.

The indentation holes in Figure 6.17 also show evidence of pile-up around the edges of the hole. This pile-up is asymmetric which may be further evidence that the tip was not oriented exactly perpendicular to the surface. An alternative explanation of the shape variants is that there may have been different defect densities in the gold crystal below the surface from region to region that affected the shape of the indent.

6.6.3 Indentation Sizes

From the STM scans both the depth of the hole, δ_{pl}, and the width of the plastic zone, $2R_{pl}$, were measured (see Figure 6.18). The accuracy in the measurements was found to be $< \pm 0.6$ nm for δ_{pl} and $< \pm 10$ nm for $2R_{pl}$. As shown in Figure 6.19a, the hole depth measured by the STM scan was always smaller than the hole depth measured from the force vs. penetration depth curve. The latter was determined by the value of the penetration depth when the force was zero during the withdrawal. At this point the tip is at its original rest position where no positive force acts on it; i.e. it is just resting inside a plastically deformed hole. As discussed in Sections 6.5.2 and 6.5.3, adhesion is sometimes observed once the sample is pulled further away from this point. Adhesive forces and neck formation could lead to material being pulled up in the bottom of the hole making it appear shallower in an STM scan. Fine structure within the hole is not resolvable since the hole was scanned using the same tip used to create the hole, and thus tip shape convolution effects are large. Due to these STM imaging artifacts, the depth of the hole as determined from the x-intercept of the force vs. penetration depth curve is deemed to be the more accurate measurement of the indent depth.

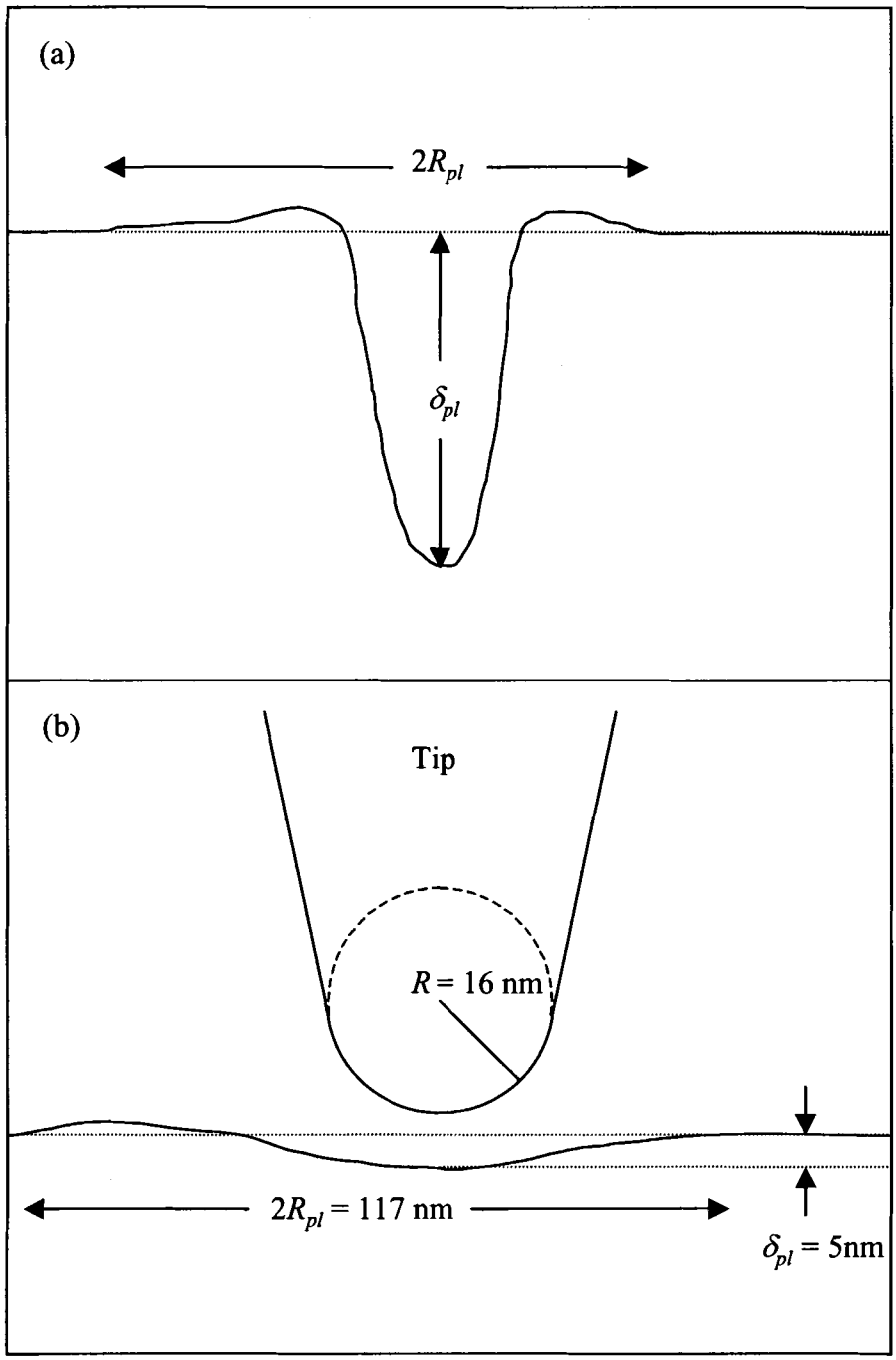

Figure 6.18: Indentation hole parameters. (a) Schematic of an exaggerated STM line scan which shows the parameters measured for each indentation. (b) Schematic of a typical 19 nm PST displacement indentation which shows the tip and indent sizes to scale.

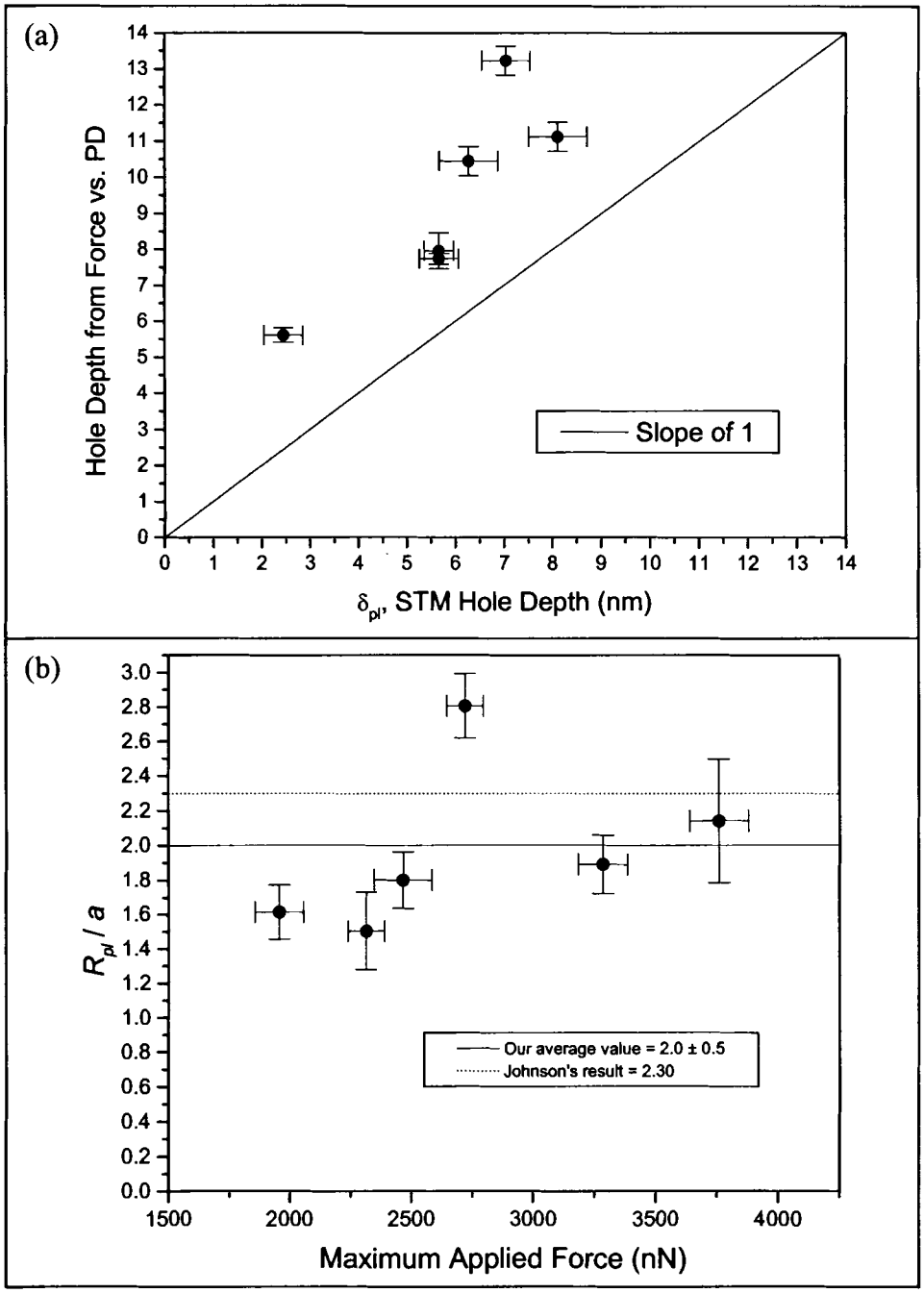

Figure 6.19: Analysis of indentation hole. (a) Depth of indentation hole measured from force vs. penetration depth curves compared to the depth of hole measured from STM scans of indentations. (b) Ratio of plastic zone radius to the contact radius between tip and sample vs. maximum load during the indentation. Our result is compared to a theoretical prediction for the ratio by Johnson [16].

When examining the experimentally determined aspect ratio of the indentation, R_{pl} / δ_{pl}, as a function of the scanned penetration depth, δ_{pl}, we found a trend that is similar to results by Keily *et al.* [21], namely that the penetration depth increases at a faster rate than the plastic zone width.

Several models [16,49] predict that the plastic zone radius and the contact radius between the tip and sample should increase at the same rate. Johnson [16] derives an expression from an elastic-plastic indentation for the ratio of plastic zone radius to the contact radius, R_{pl} / a. The model assumes that the plastic zone has a spherical shape in the sample surface due to the indentation, there is an infinite elastic media which borders the plastic zone, the yield stress remains constant and that the sample is incompressible. The model yields the following expression for the ratio R_{pl} / a:

$$\frac{R_{pl}}{a} = \exp\left[\frac{1}{2}\left(\frac{\bar{\sigma}}{\sigma_y} - \frac{4}{3}\right)\right]. \tag{6.12}$$

$\bar{\sigma}$ is the mean normal stress and σ_y is the yield strength of the surface material. For a fully plastically deformed material $\bar{\sigma} \sim 3\ \sigma_y$. Given this condition, Eq. 6.12 gives the result $R_{pl} / a = 2.30$.

We have compared our results with this model by first estimating a contact radius, a, using Hertzian mechanics [16]:

$$a = \sqrt{R\delta_{pl}}\ , \tag{6.13}$$

where R is the tip radius. For δ_{pl} we used the value of the x-intercept on the force vs. penetration depth curve. Figure 6.19b shows the ratio R_{pl} / a versus the maximum load obtained during the indentation. From our data, we compute a ratio of 2.0 ± 0.5 (error is

calculated from the standard deviation), which appears to be independent of the applied force. Johnson's prediction [16] shown by the dotted line, falls within the uncertainty of our average value even though we estimated the contact area using the Hertzian model that does not take into account plastic deformation. Keily *et al.* [21] found a slightly larger value, $R_{pl} / a = 3$, in their experiments on gold. Once again it is noted that a continuum model appears to be sufficient for analyzing nanoindentations in our contact size regime.

Pile-up behavior can be seen in STM images of the indents (see Figure 6.17). Pile-up height measurements did not provide useful information due to noise levels being between 50% to 100% of the height measurements. The measured pile-up heights ranged between 0.5 nm to 1.4 nm. It is also noted that corrugation heights reported for Au (110) are on the order of 1.4 Å [50]. We were not able to resolve the corrugations, since the noise level for the scanned images was in the range of 3 Å to 6 Å.

6.7 References for Chapter 6

1. Cross, G., Schirmeisen, A., Stalder, A., Grütter, P., Tschudy, M., and Durig, U., Physical Review Letters 80, 4685 (1998).
2. Schirmeisen, A., Cross, G., Stalder, A., Grütter, P., and Durig, U., Applied Surface Science 157, 274 (2000).
3. Cross, G., Mechanics of Nanometer Scale Indentation of a Metal Surface, Ph.D. thesis, McGill University, Montreal, Quebec, Canada, 1999.
4. Schirmeisen, A., Cross, G., Stalder, A., Grütter, P., and Durig, U., New Journal of Physics 2, 29.1 (2000).

5 . Binnig, G., Rohrer, H., Gerber, Ch., and Weibel, E., Surface Science 131, L380 (1983).

6 . Schneir, J., Sonnenfeld, R., Marti, O., Hansma, P.K., Demuth, J.E., and Hamers, R.J., Journal of Applied Physics 63, 718 (1988).

7 . Emch, R., Nogami, J., Dovek, M.M., Lang, C.A., and Quate, C.F., Journal of Applied Physics 65, 80 (1989).

8 . Stalder, A. and Durig, U., Journal of Vacuum Science and Technology B 14, 1259 (1996).

9 . Chen, J.C., Introduction to Scanning Tunneling Microscopy, (Oxford University Press, New York, 1993), p. 38.

10 . Kuk, Y., in Scanning Tunneling Microscopy I, edited by Guntherodt, H.-J. and Wiesendanger, R. (Springer-Verlag, New York, 1992), p. 17.

11 . Burnham, N.A. and Colton, R.J., Journal of Vacuum Science and Technology A 7, 2906 (1989).

12 . Stalder, A. and Durig, U., Probe Microscopy 1, 135 (1998).

13 . Stalder, A. and Durig, U., Applied Physics Letters 68, 637 (1996).

14 . Agrait, N., Rubio, G., and Vieira, S., Physical Review Letters 74, 3995 (1995).

15 . Burnham, N.A., Colton, R.J., and Pollock, H.M., Physical Review Letters 69, 144 (1992).

16 . Johnson, K.L., Contact Mechanics, (Cambridge University Press, New York, 1985).

17 . Kiely, J.D. and Houston, J.E., Physical Review B 57, 12588 (1998).

18. Hertzberg, R.W., Deformation and Fracture Mechanics of Engineering Materials, 2nd ed. (John Wiley and Sons, New York, 1983), p. 8.

19. Timoshenko, S., Theory of Elasticity, (McGraw-Hill Book Company, Inc., New York, 1934).

20. Tangyunyong, P., Thomas, R.C., Houston, J.E., Michalske, T.A., Crooks, R.M., and Howard, A.J., Physical Review Letters 71, 3319 (1993).

21. Kiely, J.D., Jarausch, K.F., Houston, J.E., and Russell, P.E., Journal of Materials Research 14, 2219 (1999).

22. Corcoran, S.G., Colton, R.J., Lilleodden, E.T., and Gerberich, W.W., Physical Review B 55, R16057 (1997).

23. Kelchner, C.L., Plimpton, S.J., and Hamilton, J.C., Physical Review B 58, 11085 (1998).

24. Michalske, T.A. and Houston, J.E., Acta Materialia 46, 391 (1998).

25. Keily, J.D., Hwang, R.Q., and Houston, J.E., Physical Review Letters 81, 4424 (1998).

26. Agrait, N., Rubio, G., and Vieira, S., Langmuir 12, 4505 (1996).

27. Rubio, G., Agrait, N., and Vieira, S., Physical Review Letters 76, 2302 (1996).

28. Bahr, D.F. and Gerberich, W.W., Journal of Materials Research 13, 1065 (1998).

29. Argon, A.S, in Mechanical Behavior of Materials, edited by McClintock, F.A. and Argon, A.S. (Addison-Wesley, Reading, MA 1966), p. 130.

30. McHargue, C.J., in Tribology Issues and Opportunities in MEMS Proceedings of the NSF/AFOSR/ASME Workshop on Tribology Issues and Opportunities, edited by Bhushan, B. (Kluwer Academic Publishers, Boston, MA, 1998), p. 495.

31 . Page, T.F., Oliver, W.C., and McHargue, C.J., Journal of Materials Research 7, 450 (1992).

32 . Pharr, G.M., Oliver, W.C., and Clarke, D.R., Journal of Electronic Materials 19, 881 (1990).

33 . Derjaguin, B.V., Muller, V.M., and Toporov, Y.P., Journal of Colloid Interface Science 53, 314 (1975).

34 . Johnson, K.L., Kendall, K., and Roberts, A.D., Proceedings of the Royal Society of London Series A 324, 301 (1971).

35 Tabor, D., Journal of Colloid Interface Science 58, 1 (1976).

36 . Unertl, W.N., Journal of Vacuum Science and Technology A 17, 1779 (1999).

37 . Yanson, A.I., Bollinger, G. Rubio, van den Brom, H.E., Agrait, N., and van Ruitenbeek, J.M., Nature 395, 783 (1998).

38 . Agrait, N., Rodrigo, J.G., Rubio, G., Sirvent, C., and Vieira, S., Thin Solid Films 253, 199 (1994).

39 . Landman, U., Luedtke, W.D., Burnham, N.A., and Colton, R.J., Science 248, 454 (1990).

40 . Burns, G., Solid State Physics, (Academic Press, Inc., Orlando, Florida, 1985).

41 . Jansen, A.G.M., van Gelder, A.P., and Wyder, P., Journal of Physics C: Solid State Physics 13, 6073 (1980).

42 . Miller, M.K. and Smith, G.D.W., Atom Probe Microanalysis: Principles and Applications to Materials Problems, (Materials Research Society, Pittsburgh, Pennsylvania, 1989).

43 . Montagu-Pollock, H.M., Rhodin, T.N., and Southon, M.J., Surface Science 12, 1 (1968).

44 . Schirmeisen, A., Metallic Adhesion and Tunneling at the Atomic Scale, Ph.D. thesis, McGill University, Montreal, Quebec, Canada, 1999.

45 . Nishikawa, O. and Müller, E.W., IEEE Transactions on Parts, Materials and Packaging, PMP-5, 38 (1969).

46 . Müller, E.W. and Tsong, T.T., Field Ion Microscopy Principles and Applications, (American Elsevier Publishing Co., Inc., New York, 1969), p. 275-276.

47 . Brainard, W.A. and Buckley, D.H., NASA Technical Note, NASA TN D-6492, 1971.

48 . Honeycombe, R.W.K., The Plastic Deformation of Metals, (St. Martin's Press, New York, 1968).

49 . Bahr, D.F. and Gerberich, W.W., Metallurgical and Materials Transactions A 27A, 3793 (1996).

50 . Binnig, G., Rohrer, H., Gerber, Ch., and Weibel, E., Surface Science 131, L379 (1983).

Chapter 7

CONCLUSIONS AND FUTURE WORK

7.1 Conclusions

An instrument was developed to study nanometer scale deformation behavior at well-defined contacts in ultra-high vacuum. The experimental results acquired with this instrument have provided new information about tungsten-gold contacts in a deformation volume size on the order of 100 nm wide by 10 nm deep. In general, we have found that continuum mechanics theories are good in describing certain aspects of the deformation, while some experimental signatures require interpretation at the atomistic scale.

The instrument that we constructed combines atomic force microscopy (AFM), scanning tunneling microscopy (STM), and field ion microscopy (FIM) into a single experimental apparatus. This required the design, fabrication, and calibration of several novel electronic, optical and vacuum components. The advantage of this approach is that a well-defined tip can be shaped and characterized in ultra-high vacuum by FIM and then be immediately used to perform nanometer scale indentation experiments on atomically clean single crystal surfaces. We were able to obtain sufficient atomic resolution of the FIM tip at room temperature to accurately measure the tip radius and carry out high load / small area experiments without the complications of cryogenic cooling.

Our tungsten tip - gold sample deformation experiments were carried out using a cross hair force sensor that limits motion of the tip to the normal direction thereby eliminating lateral force components during the measurement. The motion of the force sensor and tip was measured with a differential interferometer to within 0.17 nm

precision corresponding to a force resolution of 75 nN. Noise levels in the interferometer ultimately limited the accuracy of the force-displacement measurements in our experiments.

Our nanoindentation experiments on gold were carried out in the tip size range 12.8 nm $\leq$ tip radii $\leq$ 21.6 nm. This size regime falls in between that used in other recent tungsten/gold contact experiments which have used either smaller tip radii of $\leq$ 3.0 nm [1] or larger tip radii of $\geq$ 25 nm [2]. We found similar results to these other studies with regard to the mean normal stress at first yield events, hardness values, and ratio of the plastic zone depth to the contact area radius. We also measured response signatures relating to multiple yielding events, tip robustness, indentation shapes, neck formations, and major versus minor yield events.

Continuum mechanics models were found to be useful in understanding several experimental features despite the small contact size regime in our experiments. During the initial elastic deformation, good agreement was found with the Hertzian contact model even though this model assumes no adhesion and we clearly had adhesion. Also, our ratio of the plastic zone depth to the contact area radius was consistent with the predictions of a continuum model involving contact within a conical spherical cavity posed by Johnson [3].

It is important to note that our results agree well with many reported observations by Houston *et al.* [4,5,6,7] during the insertion part of the nanoindentation experiment. They treated their gold surface with a self-assembled monolayer to avoid adhesion effects, while our experiments allowed adhesion. This indicates that adhesion effects do not significantly influence the mean normal stress at the first yield event, the initiation of

major and minor events, or elastic deformation behavior. However, during the withdrawal part of the nanoindentation experiment, adhesion phenomena led to markedly different behavior.

During withdrawal, our results revealed indications of pop-out events occurring in the gold crystal which have not been reported before in gold. Large negative force excursions during withdrawal suggest the possibility of neck formation before the break of contact. Agrait *et al.* [8,9,10] and Durig *et al.* [11,12] have performed extensive necking experiments using tips and samples made from the same material. Our evidence for neck formation at tungsten/gold contacts after multiple yielding events is the first reported for nano-contacts between dissimilar materials. STM imaging following the indentation experiments revealed various indentation shapes that can be explained by the operating $\{111\}\langle 110\rangle$ crystallographic slip system in gold.

Our experimental setup most closely resembles that of Grütter *et al.* [1,13] who also used FIM for tungsten tip formation and characterization prior to indentation experiments on gold in UHV. However, their contact size is about an order of magnitude smaller, and their work has concentrated primarily on elastic indentations. Our FIM results have shown that no significant damage occurs to the tip apex during an indentation, which is consistent with the results found by Grütter *et al.* [1,13].

7.2 Recommended Future Work

Improvements in our instrument involving reduced interferometer noise, better electronics filtration, and faster response will enable higher resolution force versus displacement measurements to be made. The most important task should be to improve the interferometer design by reducing the size and path length of the optical system by

using, for example, fiber optics or solid state lasers. Since the interferometer signal affects both the force measurements as well as the penetration depth measurements, improvements would allow more accurate measurements of yielding events and adhesion phenomena. Developing faster electronics may help to more accurately measure material response time during yielding. Also, faster electronics and careful filtering of the STM current-to-voltage converter would help to better track electronic transitions during yielding and provide information about necking geometries.

Another important improvement to the instrument relates to the incorporation of new cross hair force sensors. The new method that we developed for building force sensors with better defined force constants shows much promise. Repeating the experiments with several of these force sensors would give better statistics, allow for more accurate force measurements, and provide the ability to use force sensors with different force constants.

Experiments should be performed using tip radii over a broader range in order to learn how many of our results depend on the exact tip size and contact area (i.e. mean normal stress at first yield event, hardness, pile up effects, etc.). Additional effort is needed to analyze adhesion during tip withdrawal after plastic events have occurred. Experiments with faster electronics and better characterized force sensor response would help in furthering the understanding of dislocation formation during yielding events particularly as a function of penetration depth and tip size.

In terms of chemical information and material transfer during contact, low temperature FIM would allow comparison of high resolution images before and after contact to accurately determine any movement of surface atoms and dislocation

formation. FIM combined with atom probe time-of-flight would also be extremely valuable for analyzing material adhered to the tip after break of contact. FIM may even be used to determine the exact contact area during the indentation, especially if coordinated with high resolution contact current measurements.

7.3 References for Chapter 7

1. Cross, G., Mechanics of Nanometer Scale Indentation of a Metal Surface, Ph.D. thesis, McGill University, Montreal, Quebec, Canada, 1999.
2. Keily, J.D., Hwang, R.Q., and Houston, J.E., Physical Review Letters 81, 4424 (1998).
3. Johnson, K.L., Contact Mechanics, (Cambridge University Press, New York, 1985).
4. Michalske, T.A. and Houston, J.E., Acta Materialia 46, 391 (1998).
5. Kiely, J.D. and Houston, J.E., Physical Review B 57, 12588 (1998).
6. Keily, J.D., Hwang, R.Q., and Houston, J.E., Physical Review Letters 81, 4424 (1998).
7. Kiely, J.D., Jarausch, K.F., Houston, J.E., and Russell, P.E., Journal of Materials Research 14, 2219 (1999).
8. Agrait, N., Rodrigo, J.G., Rubio, G., Sirvent, C., and Vieira, S., Thin Solid Films 253, 199 (1994).
9. Agrait, N., Rubio, G., and Vieira, S., Langmuir 12, 4505 (1996).
10. Rubio, G., Agrait, N., and Vieira, S., Physical Review Letters 76, 2302 (1996).
11. Stalder, A. and Durig, U., Applied Physics Letters 68, 637 (1996).

12 . Stalder, A. and Durig, U., Journal of Vacuum Science and Technology B 14, 1259 (1996).

13 . Cross, G., Schirmeisen, A., Stalder, A., Grütter, P., Tschudy, M., and Durig, U., Physical Review Letters 80, 4685 (1998).

Bibliography

Agrait, N., Rodrigo, J.G., Rubio, G., Sirvent, C., and Vieira, S., "Plastic deformation in atomic size contacts," Thin Solid Films 253, 199 (1994).

Agrait, N., Rubio, G., and Vieira, S., "Plastic deformation in nanometer scale contacts," Langmuir 12, 4505 (1996).

Agrait, N., Rubio, G., and Vieira, S., "Plastic deformation of nanometer-scale gold connective necks," Physical Review Letters 74, 3995 (1995).

Analog Devices, Inc., One Technology Way, P.O. Box 9106, Norwood, MA 02062.

Apex Microtechnology Corporation, 5980 N. Shannon Road, Tucson, AZ 85741-5230.

Argon, A.S, in Mechanical Behavior of Materials, edited by McClintock, F.A. and Argon, A.S. (Addison-Wesley, Reading, MA 1966), p. 130.

ARIS® is a registered trademark of Burleigh Instruments, Inc., Burleigh Park, Fishers, NY 14453.

Bahr, D.F. and Gerberich, W.W., "Relationships between acoustic emission signals and physical phenomena during indentation," Journal of Materials Research 13, 1065 (1998).

Bahr, D.F. and Gerberich, W.W., "Plastic zone and pileup around large indentations," Metallurgical and Materials Transactions A 27A, 3793 (1996).

Baselt, D., Ph.D. thesis, California Institute of Technology, Pasadena, CA 91125, 1993.

Belak, J.F., "Nanotribology," MRS Bulletin 18 (5), 15 (1993).

Binnig, G., Rohrer, H., Gerber, Ch., and Weibel, E., "(111) facets as the origin of reconstructed Au (110) surfaces," Surface Science 131, L379 (1983).

Brainard, W.A. and Buckley, D.H., "Preliminary studies by field ion microscopy of adhesion of platinum and gold to tungsten and iridium," NASA Technical Note, NASA TN D-6492, 1971.

Brandbyge, M. *et al.*, "Quantized conductance in atom-sized wires between two metals," Physical Review B 52, 8499 (1995).

Burnham, N.A., Colton, R.J., and Pollock, H.M., "Work-function anisotropies as an origin of long-range surface forces," Physical Review Letters 69, 144 (1992).

Burnham, N.A. and Colton, R.J., "Measuring the nanomechanical properties and surface forces of materials using an atomic force microscope," Journal of Vacuum Science and Technology A 7, 2906 (1989).

Burns, G., Solid State Physics, (Academic Press, Inc., Orlando, Florida, 1985).

Burr-Brown Corporation, P.O. Box 11400, Tucson, AZ 85734.

Carpenter HYMU "80"® is a registered trademark of Carpenter Technology Corporation, 101 W. Bern St., Reading, PA 19612-4662.

Chen, J.C., Introduction to Scanning Tunneling Microscopy, (Oxford University Press, New York, 1993), p. 38.

Clark, S.M., Advances in Scanning Force Microscopy, Ph.D. thesis, California Institute of Technology, Pasadena, CA 91125, 1992.

Clavilier, J., Faure, R., Guinet, G., and Durand, R., "Preparation of monocrystalline Pt microelectrodes and electrochemical study of the plane surfaces cut in the direction of the {111} and {110} planes," Journal of Electroanalytical Chemistry 107, 205 (1980).

ConFlat® is a registered trademark of Varian Vacuum Products, 121 Hartwell Ave., Lexington, MA 02173.

Corcoran, S.G., Colton, R.J., Lilleodden, E.T., and Gerberich, W.W., "Anomalous plastic deformation at surfaces: nanoindentaion of gold single crystals," Physical Review B 55, R16057 (1997).

Cross, G., Schirmeisen, A., Stalder, A., Grütter, P., Tschudy, M., and Durig, U., "Adhesion interaction between atomically defined tip and sample," Physical Review Letters 80, 4685 (1998).

Cross, G., Mechanics of Nanometer Scale Indentation of a Metal Surface, Ph.D. thesis, McGill University, Montreal, Quebec, Canada, 1999.

Derjaguin, B.V., Muller, V.M., and Toporov, Y.P., "Effect of contact deformations on the adhesion of particles," Journal of Colloid Interface Science 53, 314 (1975).

Emch, R., Nogami, J., Dovek, M.M., Lang, C.A., and Quate, C.F., "Characterization of gold surfaces for use as substrates in scanning tunneling microscopy studies," Journal of Applied Physics 65, 80 (1989).

Enachescu, M., currently employed at Lawrence Berkeley Laboratory at the University of California, Berkeley, CA 94270.

Epoxy Technology, Inc., 14 Fortune Drive, Billerica, MA 01821.

Ferrante, J. and Smith, J.R., "Theory of the bimetallic interface," Physical Review B 31, 3427 (1985).

Foiles, S.M., Baskes, M.I., and Daw, M.S., "Embedded-atom-method functions for the fcc metals Cu, Ag, Au, Ni, Pd, Pt, and their alloys," Physical Review B 33, 7983 (1986).

From a data sheet HOT Microchannel® Plates from BURLE ELECTRO-OPTICS, INC. Used with permission of BURLE TECHNOLOGIES, INC.

Harrison, J.A., White, C.T., Colton, R.J. and Brenner, D.W., "Atomistic simulations of friction at sliding diamond surfaces," MRS Bulletin 18 (5), 50 (1993).

Hertzberg, R.W., Deformation and Fracture Mechanics of Engineering Materials, 2nd ed. (John Wiley and Sons, New York, 1983), p. 8.

Hirth, J.P. and Lothe, J., Theory of Dislocations, (Krieger, Malabar, FL, 1982).

Honeycombe, R.W.K., The Plastic Deformation of Metals, (St. Martin's Press, New York, 1968).

Houston, J.E. and Michalske, T.A., "The interfacial-force microscope," Nature 356, 266 (1992).

HyMu "80"® is a registered trademark of Carpenter Technology Corporation.

Inchworm® is a registered trademark of Burleigh Instruments, Inc., Burleigh Park, Fishers, NY 14453.

Jansen, A.G.M., van Gelder, A.P., and Wyder, P., "Point-contact spectroscopy in metals," Journal of Physics C: Solid State Physics 13, 6073 (1980).

Johnson, K.L., Contact Mechanics, (Cambridge University Press, New York, 1985).

Johnson, K.L., Kendall, K., and Roberts, A.D., "Surface energy and the contact of elastic solids," Proceedings of the Royal Society of London Series A 324, 301 (1971).

Joyce, S.A. and Houston, J.E., "A new force sensor incorporating force-feedback control for the interfacial force microscopy," Review of Scientific Instruments 62, 710 (1991).

Joyce, S.A., Thomas, R.C., Houston, J.E., Michalske, T.A., and Crooks, R.M., "Mechanical relaxation of organic monolayer films measured by force microscopy," Physical Review Letters 68, 2790 (1992).

Kaneko, R., "Microtribology related to MEMS," Proceedings IEEE Micro Electro Mechanical Systems, 1 (1991).

Kelchner, C.L., Plimpton, S.J., and Hamilton, J.C., "Dislocation nucleation and defect structure during surface indentation," Physical Review B 58, 11085 (1998).

Kiely, J.D. and Houston, J.E., "Nanomechanical properties of Au (111), (011), and (110) surfaces," Physical Review B 57, 12588 (1998).

Keily, J.D., Hwang, R.Q., and Houston, J.E., "Effect of surface steps on the plastic threshold in nanoindentation," Physical Review Letters 81, 4424 (1998).

Kiely, J.D., Jarausch, K.F., Houston, J.E., and Russell, P.E., "Initial stages of yield in nanoindentation," Journal of Materials Research 14, 2219 (1999).

Kuk, Y., in Scanning Tunneling Microscopy I, edited by Guntherodt, H.-J. and Wiesendanger, R. (Springer-Verlag, New York, 1992).

Landman, U., Luedtke, W.D., Burnham, N.A., and Colton, R.J., "Atomistic mechanisms and dynamics of adhesion, nanoindentation, and fracture," Science 248, 454 (1990).

Long-Life™ Microchannel Plate is a trademark of Burle Industries, Inc.

Macor® is a registered trademark of Corning Inc., One Riverfront Plaza, Corning, NY 14831.

McHargue, C.J., in Tribology Issues and Opportunities in MEMS Proceedings of the NSF/AFOSR/ASME Workshop on Tribology Issues and Opportunities, edited by Bhushan, Bharat (Kluwer Academic Publishers, Boston, MA, 1998).

Melmed, A.J., "The art and science and other aspects of making sharp tips," Journal of Vacuum Science Technology B 9, 601 (1991).

Michalske, T.A. and Houston, J.E., "Dislocation nucleation at nano-scale mechanical contacts," Acta Materialia 46, 391 (1998).

Miller, M.K. and Smith, G.D.W., Atom Probe Microanalysis: Principles and Applications to Materials Problems, (Materials Research Society, Pittsburgh, Pennsylvania, 1989).

Montagu-Pollock, H.M., Rhodin, T.N., and Southon, M.J., "Some properties of thin metal films observed by field-ion and field emission microscopy," Surface Science 12, 1 (1968).

Müller, E.W., Advances in Electronics and Electron Physics Vol. XIII, (Academic Press, New York, 1960).

Müller, E.W. and Tsong, T.T., Field Ion Microscopy Principles and Applications, (American Elsevier Publishing Co., Inc., New York, 1969).

National Science and Technology Council, Committee on Technology, Subcommittee on Nanoscale Science, Engineering and Technology, National Nanotechnology Initiative: The Initiative and its Implementation Plan, July 2000. Can be located at <http://nano.gov/nni2.htm#DocumentBody>.

Nishikawa, O. and Müller, E.W., "Field ion microscopy of contacts," IEEE Transactions on Parts, Materials and Packaging, PMP-5, 38 (1969).

Page, T.F., Oliver, W.C., and McHargue, C.J., "The deformation behavior of ceramic crystals subjected to very low load (nano)indentations," Journal of Materials Research 7, 450 (1992).

Part # TO-1095 from Century Spring Corporation, P.O. Box 15287, 222 East 16th St., Los Angeles, CA 90015.

Pethica, J.B. and Oliver, W.C., "Tip surface interactions in STM and AFM," Physica Scripta T19, 61 (1987).

Pharr, G.M., Oliver, W.C., and Clarke, D.R., "The mechanical behavior of silicon during small-scale indentation," Journal of Electronic Materials 19, 881 (1990).

Pharr, G.M and Oliver, W.C., "Nanoindentation of silver-relations between hardness and dislocation structure," Journal of Materials Research 4, 94 (1989).

Richardson, C., senior project report with advisor Unertl, W., Department of Physics and Astronomy, The University of Maine, Orono, ME 04469.

Rose, J.H., Smith, J.R., and Ferrante, J., "Universal binding energy curves for metals and bimetallic interfaces," Physical Review Letters 47,675 (1981).

Rubio, G., Agrait, N., and Vieira, S., "Atomic-sized contacts: mechanical properties and electronic transport," Physical Review Letters 76, 2302 (1996).

Sanchez-Portal, D., Untiedt, C., Solar, J.M., Saenz, J.J., and Agrait, N., "Nanocontacts: probing electronic structure under extreme uniaxial strains," Physical Review Letters 79, 4198 (1997).

Scheer, E., Agrait, N., Cuevas, J.C., Yeyati, A.L., Ludolph, B., Martin-Rodero, A., Bollinger, G.R., van Ruitebeek, J.M., and Urbina, C., "The signature of chemical valence in the electrical conductance through a single-atom contact," Nature 394, 154 (1998).

Schirmeisen, A., Cross, G., Stalder, A., Grütter, P., and Durig, U., "Metallic adhesion forces and tunneling between atomically defined tip and sample," Applied Surface Science 157, 274 (2000).

Schirmeisen, A., Cross, G., Stalder, A., Grütter, P., and Durig, U., "Metallic adhesion and tunneling at the atomic scale," New Journal of Physics 2, 29.1 (2000).

Schirmeisen, A., Metallic Adhesion and Tunneling at the Atomic Scale, Ph.D. thesis, McGill University, Montreal, Quebec, Canada, 1999.

Schneir, J., Sonnenfeld, R., Marti, O., Hansma, P.K., Demuth, J.E., and Hamers, R.J., "Tunneling microscopy, lithography, and surface diffusion on an easily prepared, atomically flat gold surface," Journal of Applied Physics 63, 718 (1988).

Schonenberger, C. and Alvarado, S.F., "A differential interferometer for force microscopy," Review of Scientific Instruments 60, 3131 (1989).

Sirvent, C., Rodrigo, J.G., Agrait, N., and Viera, S., "STM study of the atomic contact between metallic electrodes," Physica B 218, 238 (1996).

Spectrum Signal Processing Inc., One Spectrum Court, #200, 2700 Production Way Burnaby, BC, Canada V5A 4X1.

Stalder, A. and Durig, U., "Study of yielding mechanics in nanometer-sized Au contacts," Applied Physics Letters 68, 637 (1996).

Stalder, A. and Durig, U., "Study of plastic flow in ultrasmall Au contacts," Journal of Vacuum Science and Technology B 14, 1259 (1996).

Stalder, A. and Durig, U., "Mechanics on the nanometer scale: experimental study of Au nanowires," Probe Microscopy 1, 135 (1998).

Staveley Sensors Inc., 91 Prestige Park Circle, East Hartford, CT 06108.

Tabor, D., "Surface forces and surface interactions," Journal of Colloid Interface Science 58, 1 (1976).

Tangyunyong, P., Thomas, R.C., Houston, J.E., Michalske, T.A., Crooks, R.M., and Howard, A.J., "Substrate effects on the nanometer-scale mechanics of gold films," Journal of Adhesion Science and Technology 8, 897 (1994).

Tangyunyong, P., Thomas, R.C., Houston, J.E., Michalske, T.A., Crooks, R.M., and Howard, A.J., "Nanometer-scale mechanics of gold films," Physical Review Letters 71, 3319 (1993).

Thomas, R.C., Houston, J.E., Michalske, T.A., and Crooks, R.M., "The mechanical response of gold substrates passivated by self-assembling monolayer films," Science 259, 1883 (1993).

Timoshenko, S., Theory of Elasticity, (McGraw-Hill Book Company, Inc., New York, 1934).

Unertl, W.N., "Implications of contact mechanics models for mechanical properties measurements using scanning force microscopy," Journal of Vacuum Science and Technology A 17, 1779 (1999).

Vitrodyne® is a registered trademark of John Chatillon & Sons, Inc., Greensboro, N.C. 27409-9301.

Yanson, A.I., Bollinger, G. Rubio, van den Brom, H.E., Agrait, N., and van Ruitenbeek, J.M., "Formation and manipulation of a metallic wire of single gold atoms," Nature 395, 783 (1998).

Appendix A

NEW UHV TRANSFER DESIGN

A.1 Motivation

We have recently come up with a new design to perform transfers in ultra-high vacuum (UHV). This came out of a need to minimize lateral forces during the transfer.

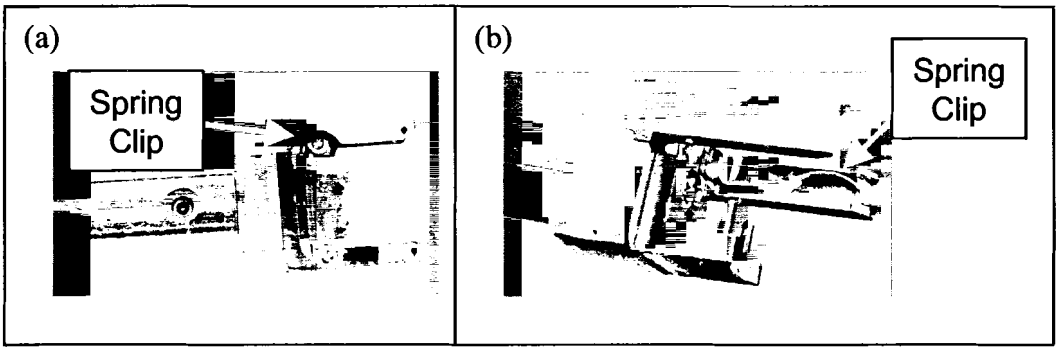

Figure A.1: Transfer arm fork. (a) Fork on the end of the transfer arm. (b) Spring clip on fork.

For our experiments, we use an Inchworm® [1] and piezoelectric scanner tube (PST) design to perform scanning tunneling microscopy (STM) and atomic force microscopy (AFM) experiments. In our original design we used a transfer arm that had a U-shaped holder on the end of it with spring clips in its arms to hold a sample holder (Figure A.1). The sample holder is placed in the spring clips in a loading chamber, then transferred to the PST in the experimental chamber (Figure A.2). On the bottom end of the PST is a sample holder mount (SHM) containing a SmCo magnet. The SHM has a conical counterbore that matches the conical shape on the back of the sample holder. The sample holder was machined out of the magnetic material HyMu "80"® [2]. With the transfer arm the sample holder is positioned directly below the SHM and then raised until

they mate. To remove the sample holder, the process is reversed. The maximum normal load rating on the Inchworm® is 0.5 kg, but the maximum lateral load is only 0.1 kg. We had a problem staying within this rated force during the sample mount docking process. As a result the Inchworm® became damaged which was generally noticed as slippage of the alumina shaft inside the Inchworm®. To solve this problem we developed a new type of transfer technique that applied only a normal load to the Inchworm®.

A.2 New Method

In the new transfer design, the spring clips are still used on the end of the transfer arm. However, instead of docking the sample holder directly into the SHM, it is loaded onto a mechanism that we affectionately refer to as "Jake" (Figure A.3). This approach permits mounting onto the SHM by applying only a normal force to the Inchworm®.

Jake is mounted in a vertical direction with the jaws pointing up and is capable of handling large lateral forces. Our sample holders have two rectangular slots milled into them. The transfer arm is used to position the sample holder directly above Jake so that the slots in the sample holder line up with the jaws on Jake. The sample holder is then lowered, using the transfer arm, so that the grooves in the jaws of Jake are located inside the milled slots of the sample holder.

Clockwise rotation of a rotary motion feedthrough (RMF) causes the jaws to simultaneously expand and be lowered in the vertical direction. When the jaws are fully expanded the sample mount is fully captured by Jake. The transfer arm is slightly lowered to compensate for the lowering of the jaws, and then pulled back. As this is done the sample mount slides through the spring clips and is left held by Jake.

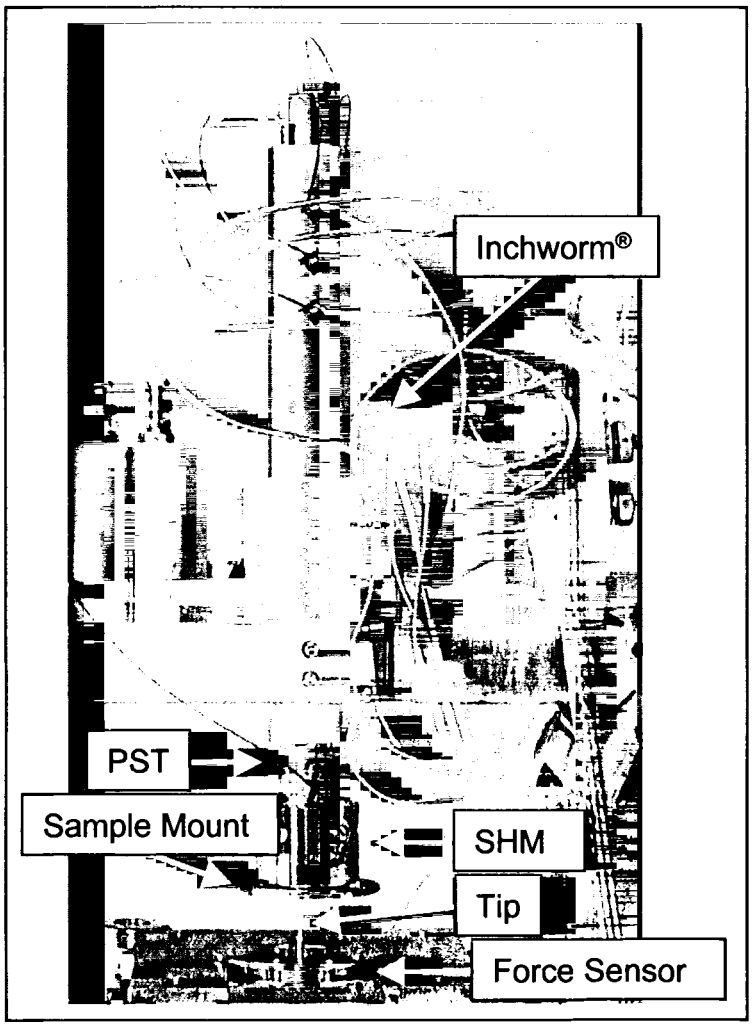

Figure A.2: Inchworm® and PST assembly.

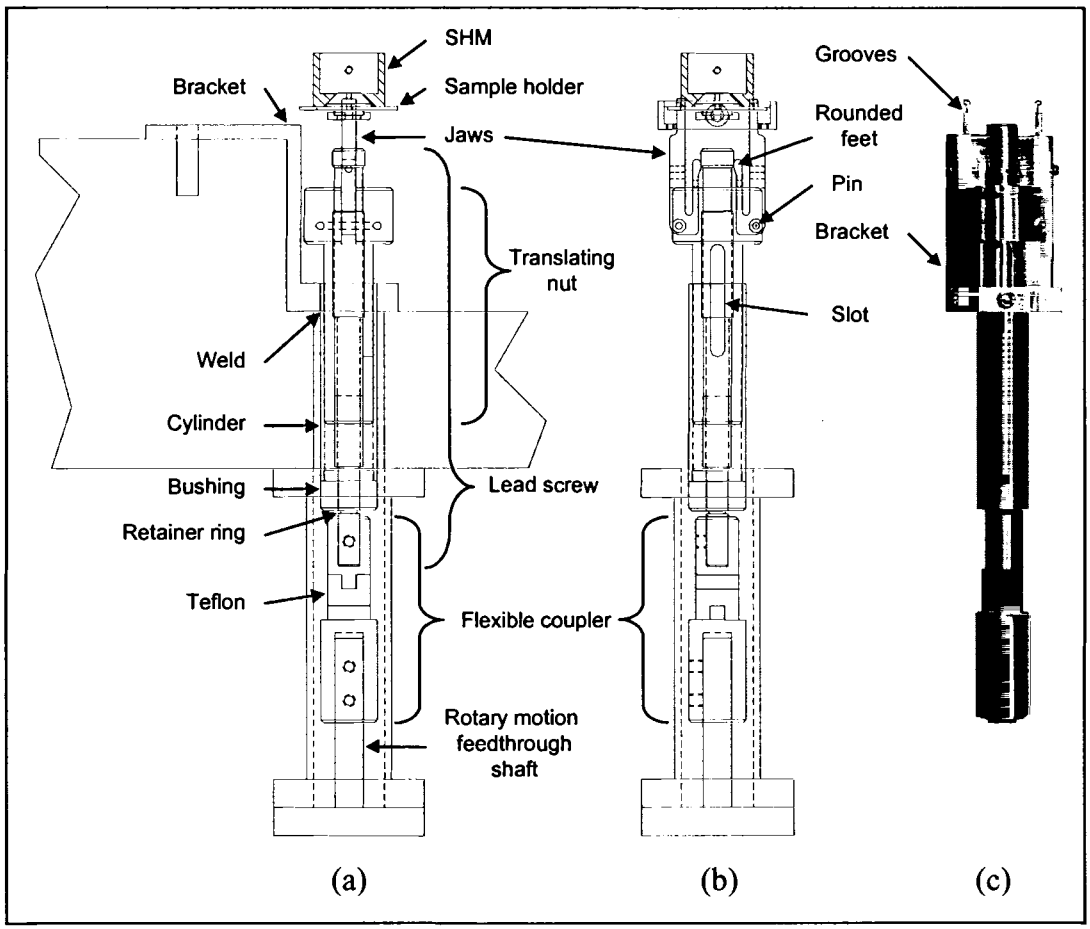

Figure A.3: "Jake". (a) Side view schematic mounted in flange. (b) Front view schematic. (c) Front view photograph.

The Inchworm® and the PST are firmly attached to a stage that is allowed to slide in the horizontal direction. The stage is slid so that the SHM is directly over the sample holder (Figure A.4a), which is being held by Jake. The Inchworm® lowers the SHM into contact with the sample holder. The conical shapes of the two parts allow the sample holder to be easily located in the SHM. Counterclockwise rotation of the feedthrough raises the jaws in the vertical direction and causes them to contract (Figure A.4b). At the same time the RMF is rotated CCW, the Inchworm® is used to raise the SHM to compensate for the rising of the jaws. When the jaws are fully contracted, the Inchworm® continues to raise the SHM and sample holder away from the jaws. The sample holder is now firmly held in place by the SmCo magnet and released from Jake (Figure A.4c). To take the sample holder from the SHM and out of the chamber, the procedures are simply reversed.

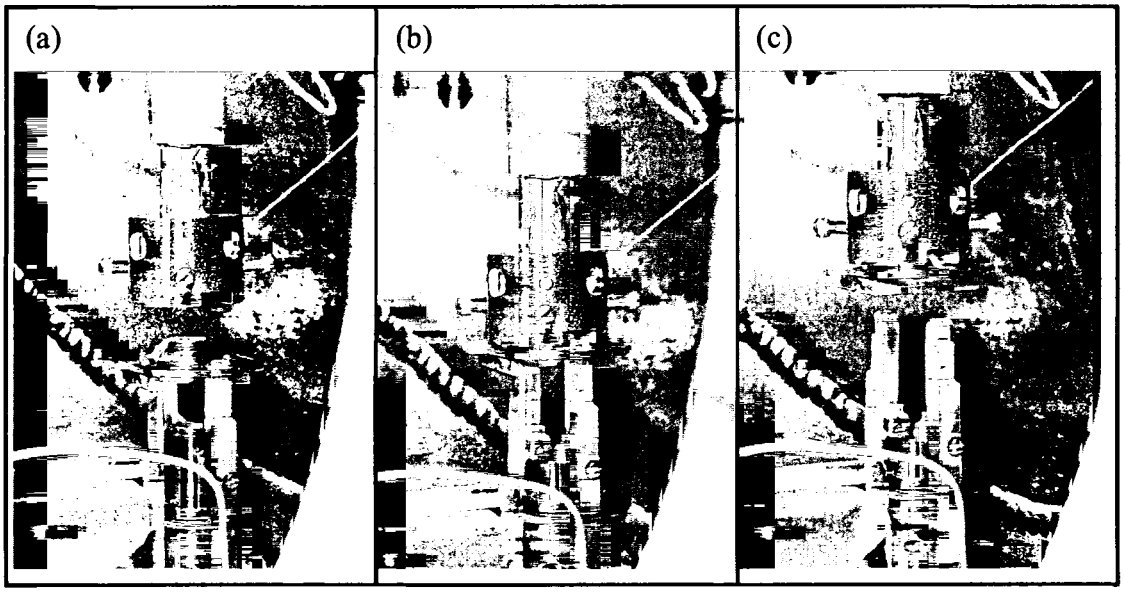

Figure A.4: PST picking up a sample holder from Jake. (a) SHM directly over sample holder, jaws expanded to hold sample holder. (b) SHM lowered into contact with sample holder, jaws contracted to release sample holder. (c) SHM holds sample holder by means of a SmCo magnet, jaws still contracted.

A.3 Design

On our design, a flexible coupler is attached to the shaft of a rotary motion feedthrough with a couple of setscrews to allow for the fact that the SHM may not be located exactly above the RMF. The top end of the flexible coupler is connected with a setscrew to a partially threaded lead screw. Screwed onto this lead screw is a translating nut that is partially threaded. The translating nut has a slot milled into its side. A screw through the bracket loosely fits into this slot. This prevents the translating nut from rotating since the bracket is rigidly attached at the top side of the flange. The end of the screw through the bracket is wrapped with a small piece of shrink teflon tubing to lower the friction against the lead screw as it rotates. As the RMF is rotated, the flexible coupling and the lead screw rotate together, but since the translating nut cannot rotate it translates vertically upward when the RMF is rotated CCW and rotates vertically downward when the RMF is rotated CW.

The middle piece of the flexible coupler is made out of teflon to allow smoother motion of the coupler. The teflon piece is not firmly attached to anything. On the lead screw there is a retainer ring below a bushing that has a reamed hole in it. The bushing fixes the location of the lead screw in the horizontal direction. The bottom of a cylinder is attached to this bushing with a setscrew. The top of the cylinder is welded to the bracket. The cylinder and bushing keep the flexible coupler from separating in the vertical direction.

The two jaws are held in place by two pins at the top of the translating nut. The pins allow the jaws to rotate. The jaws are held in place by a wire wrapped around both of them and the top of the translating nut. This wire also acts a spring to push the jaws

back together when they are being forced apart from one another. At the top of the jaws are grooves that fit into slots of the sample holder and keep it from moving in the vertical direction. The insides of the jaws have little rounded feet that rest against the shaft of the lead screw. The top of the lead screw has a section where it gets larger in diameter. There is a bit of a slope that connects the two differing diameters. As the translating nut moves vertically, the feet of the jaws ride up the shaft of the lead screw along the slopes and cause the jaws to expand or contract. The little feet of the jaws are shrink wrapped with teflon to decrease the friction on the shaft of the lead screw. A screw is present on each jaw to allow slight adjustment of the overall span of the jaws. The BeCu lead screw was sprayed with molybdinum disulfide to help lubricate moving parts; all other parts are made from 316 stainless steel.

A.4 Conclusion

A new transfer technique was developed to avoid detrimental lateral forces during sample dockings on a PST/ Inchworm® assembly. Simple rotary motion is used for both a vertical motion and an expansion and contraction of two jaws. This new type of transfer requires only a 1.33" ConFlat® [3] flange and can be easily adapted for many other types of transfer situations.

A.5 References for Appendix A

---

1. Inchworm® is a registered trademark of Burleigh Instruments, Inc., Burleigh Park, Fishers, NY 14453.
2. HyMu "80"® is a registered trademark of Carpenter Technology Corporation.
3. ConFlat® is a registered trademark of Varian Vacuum Products, 121 Hartwell Ave., Lexington, MA 02173.

Appendix B

NEW INTERCHANGEABLE PIEZO DESIGN FOR INCHWORM® MOTORS

B.1 Introduction

In scanning tunneling microscopy (STM) and atomic force microscopy (AFM), it is common practice to use an Inchworm® [1] motor coupled with a piezoelectric scanner tube (PST) in order to control movement of a tip or sample. Burleigh Instruments, Inc. sells SPM Approach Modules that perform this operation. The SPM Approach Module is constructed of a PST that is attached by means of epoxy to the inside of an alumina shaft. The alumina shaft moves up and down inside the Inchworm® motor. We have found that if the PST gets damaged (e.g. cracking), then it is very difficult, if not impossible, to replace the PST without damaging the alumina shaft or Inchworm® motor. If the alumina shaft gets damaged, then the Inchworm® motor cannot be easily repaired due to the very tight manufacturing tolerance of the alumina shaft inside the Inchworm® motor. The motor is easily damaged due to the small lateral load tolerance and is totally destroyed.

To greatly reduce the possibility of having to replace the whole SPM Approach Module after a PST breakage, we developed an interchangeable PST assembly to be used with Inchworm® motors. Instead of attaching the PST to the inside of the alumina shaft of the Inchworm® motor using epoxy, we have built an interchangeable spring loaded, friction fit PST assembly that fits inside the alumina shaft of the Inchworm® motor (Figure B.1a). This process requires purchasing an Inchworm® motor, a piezoceramic tube, a few pieces of machinable Macor® ceramic[2] and aluminum, ultra-high vaccum (UHV) compatible non-conductive epoxy, UHV compatible silver epoxy, UHV

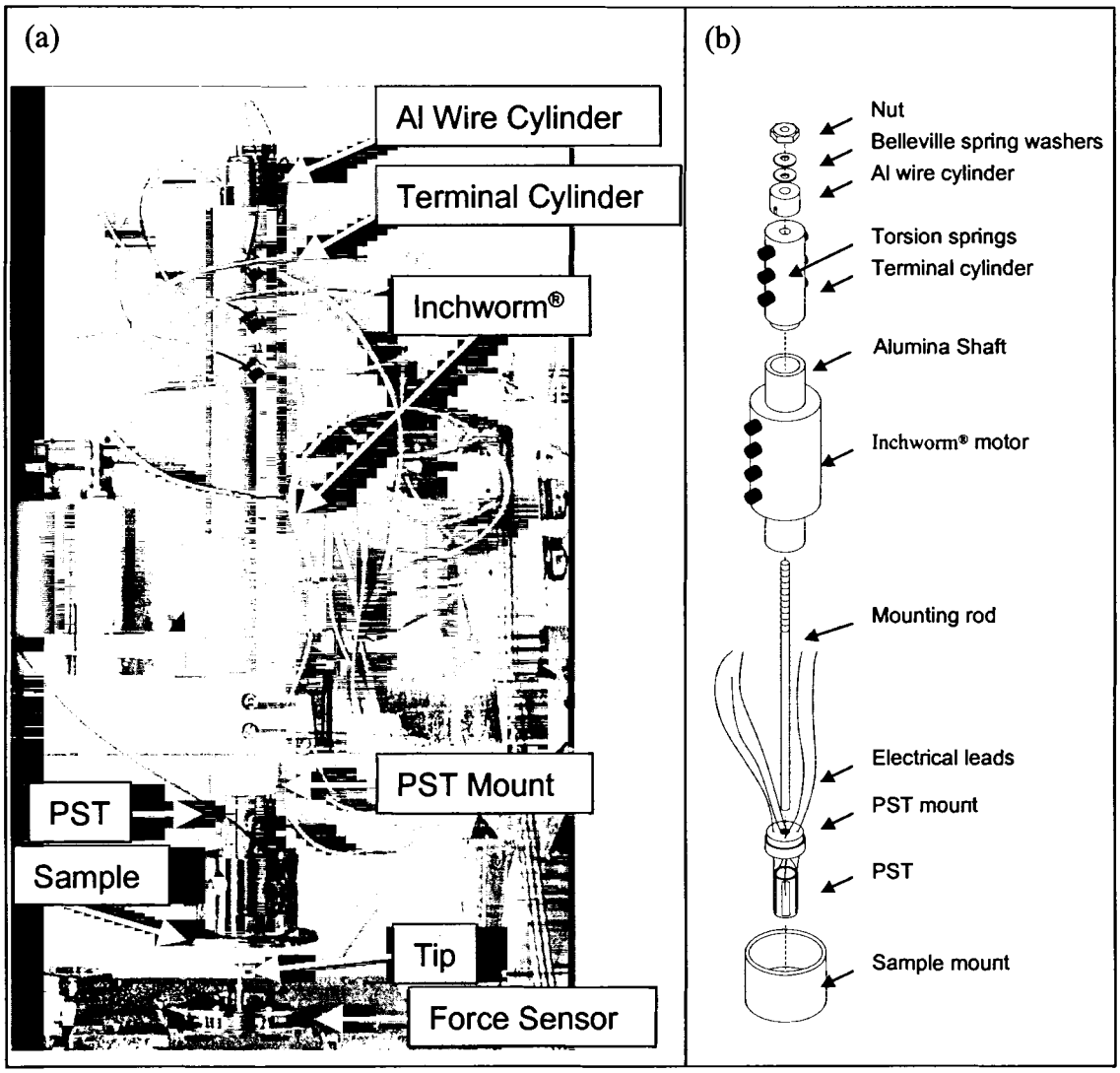

Figure B.1: Inchworm® and PST interchangeable assembly. (a) Photograph. (b) Exploded view of PST assembly.

compatible wires with insulation, and some torsion springs. In our design when the PST breaks, one only needs to cut a new tube, epoxy some wires and machine a few simple parts.

B.2 Design

Insulated electrical leads (Fig. B.1b) were first attached using HD21 silver epoxy from Epoxy Technology, Inc. [3] to the five electrodes of a piezoceramic tube. We purchased a piezoceramic tube from Staveley Sensors Inc. [4] that is 0.250" dia. x 0.020" thick x 2.0" long. The piezoceramic tube can be cut to any length desired, by means of a diamond saw, depending on the sensitivity of the scanner tube that you desire. We chose to cut our tube to a length of 0.5". This left us with three other potential backup PST's.

Next the PST mount was machined out of Macor®. Four electrical leads were fed through four holes drilled into the PST mount. The central electrical lead of the PST was fed through a hole in the center of the PST mount. The PST was attached into a counterbored hole on the bottom side of the PST mount using H74F nonconducting, UHV compatible epoxy from Epoxy Technology, Inc. A mounting rod made out of aluminum is threaded on one end, and the other end has a groove cut into it to allow the central electrical lead of the PST to feed into the interior of the alumina shaft of the Inchworm®. The mounting rod is attached, using the H74F epoxy, into a counterbored hole on the topside of the PST mount.

The mounting rod, along with the electrical leads, is fed through the inside of the alumina shaft of the Inchworm®. We used an UHVL-015 Inchworm® motor from Burleigh Instruments, Inc. On the other end of the alumina shaft, the mounting rod goes through a terminal cylinder that was machined out of Macor®. Little torsion springs [5]

that are used as the wire junctions were attached, using H74F epoxy, into drilled holes in the terminal cylinder. There is a shoulder on the bottom side of the terminal cylinder and a shoulder on the top end of the PST mount to allow these two pieces to be comfortably located inside the alumina shaft of the Inchworm®.

After the mounting rod goes through the terminal block, it goes through an aluminum wire cylinder which allows a place for the wires to come out. Lastly, the end of the mounting rod is topped off with two opposing Belleville spring washers and a nut. The washers allow for some expansion and contraction as the assembly goes through bakeout. The nut is tightened down enough to hold the assembly in place without it moving side to side.

For our purpose we attached, using H74F epoxy, a sample holder mount (SHM), machined out of Macor®, to the bottom of the PST. At the bottom of this SHM was a recessed hole containing a SmCo magnet. The magnet is sandwiched between the SHM and a machined nickel sample holder. The sample holder grips to the SHM by three setscrews.

We have found this interchangeable assembly design to be much cheaper than repurchasing new SPM Approach Modules when the PST gets damaged. We observed no noticeable detrimental effects caused by bakeout or repeated use in UHV.

B.3 References for Appendix B

---

1. Inchworm® is a registered trademark of Burleigh Instruments, Inc., Burleigh Park, Fishers, NY 14453.

2. Macor® is a registered trademark of Corning Inc., One Riverfront Plaza, Corning, NY 14831.

3 . Epoxy Technology, Inc., 14 Fortune Drive, Billerica, MA 01821.

4 . Staveley Sensors Inc., 91 Prestige Park Circle, East Hartford, CT 06108.

5 . Part # TO-1095 from Century Spring Corporation, P.O. Box 15287, 222 East 16th St., Los Angeles, CA 90015.

Biography of the Author

Steven A. Smallwood was born on January 23, 1968 in Lansdale, Pennsylvania, to the parents of Robert G. and Catherine A. Smallwood. He graduated from North Penn High School, Lansdale, Pennsylvania in June 1986. In May of 1992 he received his Bachelor of Science degree in Physics from the University of North Carolina at Charlotte, Charlotte, North Carolina. In September of 1993 Steven began his graduate studies in Physics at The University of Maine, Orono, Maine.

During the fall of 1990 Steven was selected to do research for a semester at Brookhaven National Laboratory (BNL) under the DOE Science and Engineering Research Semester. While there he correlated neck and cervical spine injuries reported from motor vehicle crash reports with magnetic resonance imaging (MRI) scans of victims. In the summer of 1991 Steven returned to BNL to do research on the coronary angiography project at the National Synchrotron Light Source. During Steven's last two years at University of North Carolina at Charlotte and during his first two years at University of Maine he was a teaching assistant. As a graduate student Steven spent one month doing field ion microscopy research at Johns Hopkins University under the DOE/EPSCoR research traineeship program. His remaining time in graduate school was spent as a research assistant.

Steven is a member of the American Physical Society. Steven is a candidate for the Doctor of Philosophy degree in Physics from The University of Maine in May, 2001.